



Contents

6.1	Introduction	204
6.2	Two-Dimensional NMR	205
6.3	Two-Dimensional Fourier Transformation in NMR	207
6.4	Peak Shapes in Two-Dimensional Spectra	209
6.5	Quadrature Detection in Two-Dimensional NMR	211
6.6	Types of Two-Dimensional NMR Spectra	212
6.6.1	Two-Dimensional Resolution/Separation Experiments	213
6.6.2	Two-Dimensional Correlation Experiments	219
6.6.3	Two-Dimensional Heteronuclear Correlation Experiments	238
6.6.4	Combination of Mixing Sequences	248
6.7	Three-Dimensional NMR	249
6.7.1	The CT-HNCA Experiment	252
6.7.2	The HNN Experiment	257
6.7.3	The Constant Time HN(CO)CA Experiment	263
6.7.4	The HN(C)N Experiment	266
6.8	Summary	270
6.9	Further Reading	270
6.10	Exercises	271
	Reference	276

The original version of the chapter has been revised. A Correction to this chapter can be found at https://doi.org/10.1007/978-3-030-88769-8_8

Learning Objectives

- Introducing new dimensions in NMR
- Different types of two- and three-dimensional NMR spectra
- Benefits of multidimensional NMR spectra in terms of resolution enhancement and extractable information

6.1 Introduction

The most significant development in NMR after the discovery of FTNMR is undoubtedly multidimensional NMR spectroscopy, although one can say in the retrospective that FTNMR had already paved the way for its development. The essence of this statement in more explicit words is that multidimensional NMR exploits the fact that in FTNMR, the excitation of the spins and detection of their response are separated in time. The first ideas of extending the dimensionality of NMR to two from the conventional one-dimensional NMR was put forward by Jean Jeener in 1971. The technique has grown since then, in an explosive manner, and continues to develop unabatedly. The tremendous success of these experiments is due to the fact that they permit the display of pairwise interactions between spins in a given molecule in the form of cross-peaks in a plane. Quantitative interpretations of these correlations have revealed structural and dynamical information on such large molecules as proteins and nucleic acids—a hitherto unthinkable fact. With this, NMR entered the realm of biology, a subject with an ocean of unsolved problems both at macroscopic and microscopic levels.

This chapter begins by introducing the concepts in a pedagogic manner; progresses gradually in complexity and rigor, illustrating the explicit calculations in few cases; and quickly jumps into more complex experiments. In these complex experiments, used in biomolecular NMR or structural biology, explicit step-by-step calculations are not shown, but the final results which help to understand the performance of the experiments are presented. Certainly, the discussion is not exhaustive, but indicative. It will expose the students to the barrage of developments, so that those who would continue research in such advanced topics can pursue with the details at a later stage.

A generalized scheme of multidimensional NMR experiment is based on the idea of “segmentation of time axis,” as shown in Fig. 6.1.

The experimental scheme begins with a “preparation period” during which the spin system is prepared in a suitable state. It can consist of a simple delay or a combination of pulses and delays or other kinds of perturbations as desired. For example, in a simple FTNMR experiment, the single-pulse excitation constitutes the preparation period during which x - y magnetization is created. A pair of 90° pulses separated by a constant evolution time constitutes the preparation period for multiple quantum spectroscopy, etc.



Fig. 6.1 Segmentation of the time axis

The “evolution periods” t_1, t_2, \dots, t_n are variables and generate $(n+1)$ dimensional time domain data, which after $(n+1)$ dimensional Fourier transformation yields the $(n+1)$ dimensional spectrum. The evolution periods help to frequency label the individual spins or group of spins with their characteristic single-quantum or multiple-quantum frequencies. Various types of manipulations with the frequencies are possible during these periods.

Mns constitute the so-called mixing periods, the most important part of the experimental scheme. It is the “mixing” which establishes correlations between frequencies in adjacent evolution periods. Different kinds of correlations can be established by exploiting different types of interactions between the spins. The most common types of interactions exploited are J-coupling interactions and through-space dipolar interactions. Hundreds of pulse sequences have been published till date. In the following sections, we shall discuss at length the principle and developments in two-dimensional (2D) NMR, which laid the foundation for higher-dimensional experiments for specific purposes.

6.2 Two-Dimensional NMR

The details of performing a two-dimensional NMR experiment are shown schematically in Fig. 6.2.

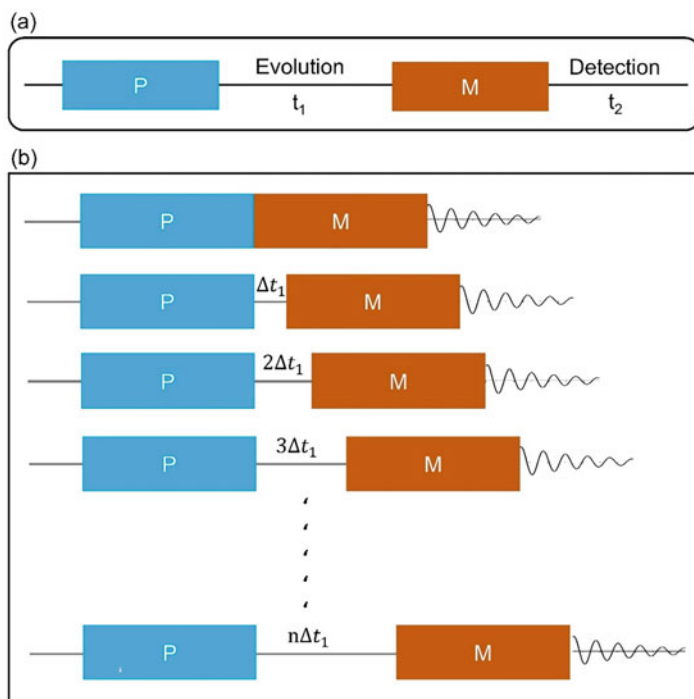


Fig. 6.2 (a) The segmentation of the time axis for the two-dimensional experiment. (b) Details of the experiment showing systematic incrementation of the evolution period, t_1

P and M are the preparation and mixing periods, respectively, and t_1 and t_2 are the evolution and detection periods, respectively. The experiment involves a collection of a number of free induction decays for systematically incremented values of t_1 . The final data set will thus be a matrix, $S(t_1, t_2)$. Fourier transformation, with respect to t_2 , results in a series of one-dimensional spectra in which the amplitudes and phases of the signals depend upon the value of t_1 . Variations of these entities as a function of time carry the frequency information present during the t_1 period (Fig. 6.3), and thus Fourier transformation of these data along t_1 results in a two-dimensional frequency domain spectrum, $S(F_1, F_2)$.

$$S(t_1, t_2) \xrightarrow{\text{FT}} S(F_1, F_2) \quad (6.1)$$

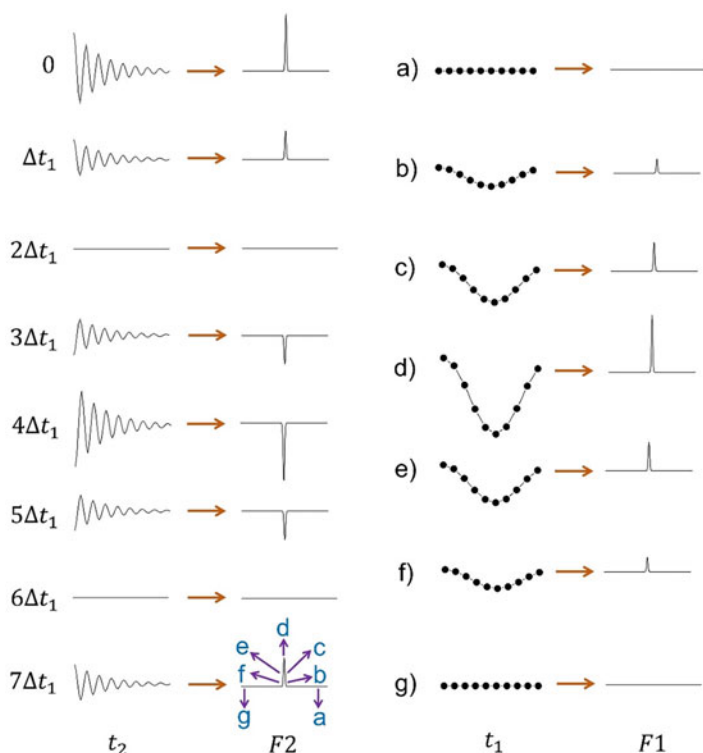
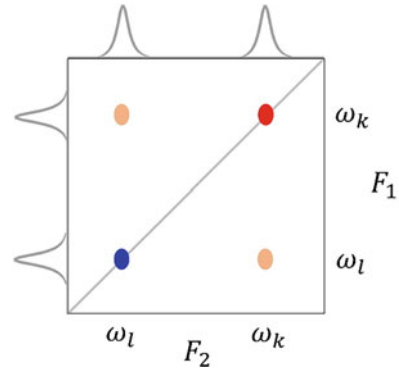


Fig. 6.3 A schematic of the processing of the two-dimensional data, $S(t_1, t_2)$. Individual FIDs (first column) collected for different t_1 time points are Fourier transformed (second column, F_2 spectra). By taking the intensities at each point on the discrete F_2 spectra, we arrive at the t_1 -dependent profiles (column 3). These FIDs are then Fourier transformed to generate the spectra along the F_1 axis. For illustration, only one line is considered. In both F_2 and F_1 spectra, one sees intensity modulations as we move through the frequency axes

Fig. 6.4 A schematic of a two-dimensional spectrum considering two spins k and l . ω_k and ω_l represent the resonance frequencies of the two spins



Consider a spin k whose x - y magnetization has been created by the preparation period, and this magnetization precesses with a frequency ω_k during the evolution period. At the end of the period t_1 the magnetization has components $M_k(0) \cos \omega_k t_1$ and $M_k(0) \sin \omega_k t_1$ along, say the y - and x -axes, respectively; $M_k(0)$ is the magnetization at the beginning of the evolution period. Let us now assume that the mixing period converts one of the above components (say $M_k(0) \sin \omega_k t_1$) into unobservable magnetization such as z -magnetization or multiple quantum coherence. From the remaining, part of the magnetization is transferred to say spin l , which has a characteristic frequency ω_l . The detected signal, as a function of t_2 , will then have two contributions.

$$A = a M_k(0) \cos \omega_k t_1 \cdot \cos \omega_k t_2 \quad (6.2)$$

$$B = b M_k(0) \cos \omega_k t_1 \cdot \cos \omega_l t_2 \quad (6.3)$$

Here it is assumed that only the y -component of the magnetization is detected during t_2 period; a and b are some coefficients representing the relative contributions. These equations represent, of course, oversimplification made to convey the concepts clearly, and we will return to rigorous calculations later on. The component A , after two-dimensional Fourier transformation, results in a peak which has the same frequency ω_k along both $F1$ and $F2$ axis. The component B , results in a peak which has frequency ω_k along $F1$ and frequency ω_l along $F2$. The former is called the “diagonal peak” and the latter the “cross-peak” in the two-dimensional spectrum. A similar description applies to the magnetization originating from the l spin. A schematic of the resultant two-dimensional spectrum is shown in Fig. 6.4.

6.3 Two-Dimensional Fourier Transformation in NMR

A two-dimensional frequency spectrum, $S(F1, F2)$, will be generated from a two-dimensional time domain data set, $S(t_1, t_2)$, by the two-dimensional Fourier transformation. This is mathematically represented as

$$S(F_1, F_2) = \mathcal{F}^{(1)} \mathcal{F}^{(2)} S(t_1, t_2) \quad (6.4)$$

where $\mathcal{F}^{(1)}$ and $\mathcal{F}^{(2)}$ represent Fourier transformation operators along the t_1 and t_2 dimensions, respectively. These have to be carried out independently. Clearly, two-dimensional FT is a succession of one-dimensional FT.

\mathcal{F} in general can be written as

$$\mathcal{F} = \mathcal{F}_c - i\mathcal{F}_s \quad (6.5)$$

where \mathcal{F}_c and \mathcal{F}_s represent cosine and sine transforms, respectively, as discussed in Chap. 3.

$S(t_1, t_2)$ is in general a complex function represented as

$$S(t_1, t_2) = \text{Re} \{S(t_1, t_2) + i \text{Im} S(t_1, t_2)\} \quad (6.6)$$

$$= S_r(t_1, t_2) + i S_i(t_1, t_2) \quad (6.7)$$

Similarly,

$$S(F_1, F_2) = S_r(F_1, F_2) + i S_i(F_1, F_2) \quad (6.8)$$

Further,

$$S(F_1, F_2) = (\mathcal{F}_c^1 - i\mathcal{F}_s^1)(\mathcal{F}_c^2 - i\mathcal{F}_s^2)\{S_r(t_1, t_2) + i S_i(t_1, t_2)\} \quad (6.9)$$

From this, it follows

$$S_r(F_1, F_2) = \mathcal{F}^{cc}\{S_r(t_1, t_2)\} - \mathcal{F}^{ss}\{S_r(t_1, t_2)\} + \mathcal{F}^{cs}\{S_i(t_1, t_2)\} + \mathcal{F}^{sc}\{S_i(t_1, t_2)\} \quad (6.10)$$

$$S_i(F_1, F_2) = \mathcal{F}^{cc}\{S_i(t_1, t_2)\} - \mathcal{F}^{ss}\{S_i(t_1, t_2)\} - \mathcal{F}^{cs}\{S_r(t_1, t_2)\} - \mathcal{F}^{sc}\{S_r(t_1, t_2)\} \quad (6.11)$$

where

$$\mathcal{F}^{cc}\{S_r(t_1, t_2)\} = \int_{-\infty}^{+\infty} dt_1 \cos \omega_1 t_1 \int_{-\infty}^{+\infty} dt_2 \cos \omega_2 t_2 S_r(t_1, t_2) \quad (6.12)$$

$$\mathcal{F}^{ss}\{S_r(t_1, t_2)\} = \int_{-\infty}^{+\infty} dt_1 \sin \omega_1 t_1 \int_{-\infty}^{+\infty} dt_2 \sin \omega_2 t_2 S_r(t_1, t_2) \quad (6.13)$$

$$\mathcal{F}^{cs}\{S_r(t_1, t_2)\} = \int_{-\infty}^{+\infty} dt_1 \cos \omega_1 t_1 \int_{-\infty}^{+\infty} dt_2 \sin \omega_2 t_2 S_r(t_1, t_2) \quad (6.14)$$

$$\mathcal{F}^{sc}\{S_r(t_1, t_2)\} = \int_{-\infty}^{+\infty} dt_1 \sin \omega_1 t_1 \int_{-\infty}^{+\infty} dt_2 \cos \omega_2 t_2 S_r(t_1, t_2) \quad (6.15)$$

Similar equations hold good for $S_i(t_1, t_2)$ as well.

Since for t_1 and $t_2 < 0$, there is no signal, the transformations will have to be considered only for the range $0 < t < \infty$.

The general principles of Fourier transformation discussed in Chap. 3 are applicable here as well, along both axes, $F1$ and $F2$ of the two-dimensional spectrum. Sensitivity and resolutions along the two axes are governed by the same considerations of sampling rate, acquisition time, data size, zero filling, window multiplications, etc. The acquisition times along the t_1 and t_2 directions are generally represented as t_1^{\max} and t_2^{\max} , respectively. While increasing t_2^{\max} can be simply accomplished by increasing the size of the FID data, increasing t_1^{\max} amounts to collecting more number of t_1 increments, and this contributes dearly to the total experimental time. Thus, for two-dimensional experiments, it is very essential to optimize the number of t_1 increments and the data need be collected only until that value of t_1 where the signal is present appreciably. The data is not actually collected during t_1 , and this decision will have to be taken by calculation, by comparing t_1^{\max} value with the T_2 of the spin system, roughly observable from one-dimensional FIDs. Typically, t_1^{\max} is limited to 50–150 ms range depending upon the type of the experiment.

6.4 Peak Shapes in Two-Dimensional Spectra

The time domain signal ($S(t_1, t_2)$) is a superposition of many coherences. Considering a particular combination of coherences between levels $t \rightarrow u$ in t_1 domain and $r \rightarrow s$ in t_2 domain, the time domain signal for this pair will be

$$S_{tu,rs}(t_1, t_2) = S_{tu,rs}(0, 0) e^{\{(-i\omega_{tu} - \lambda_{tu})t_1\}} e^{\{(-i\omega_{rs} - \lambda_{rs})t_2\}} \quad (6.16)$$

where the λ_s represent the T_2 relaxation rates for the respective coherences.

Define

$$Z_{tu,rs} = S_{tu,rs}(0, 0) \quad (6.17)$$

Then,

$$S_{tu,rs}(\omega_1, \omega_2) = Z_{tu,rs} \left\{ \frac{1}{i\Delta\omega_{tu} + \lambda_{tu}} \right\} \left\{ \frac{1}{i\Delta\omega_{rs} + \lambda_{rs}} \right\} \quad (6.18)$$

where

$$\Delta\omega_{tu} = \omega_1 + \omega_{tu}, \Delta\omega_{rs} = \omega_2 + \omega_{rs}. \quad (6.19)$$

Equation 6.18 can be rewritten as

$$S_{tu,rs}(\omega_1, \omega_2) = Z_{tu,rs} \left\{ \frac{\lambda_{tu}}{(\Delta\omega_{tu})^2 + (\lambda_{tu})^2} - \frac{i\Delta\omega_{tu}}{(\Delta\omega_{tu})^2 + (\lambda_{tu})^2} \right\} \\ \times \left\{ \frac{\lambda_{rs}}{(\Delta\omega_{rs})^2 + (\lambda_{rs})^2} - \frac{i\Delta\omega_{rs}}{(\Delta\omega_{rs})^2 + (\lambda_{rs})^2} \right\} \quad (6.20)$$

In each of the angular brackets, the first term which is real represents an absorptive line shape (A), and the second term which is imaginary represents a dispersive line shape (D).

Thus,

$$S_{tu,rs}(F1, F2) = Z_{tu,rs} \{A_{tu}(F1) - iD_{tu}(F1)\} \{A_{rs}(F2) - iD_{rs}(F2)\} \quad (6.21)$$

$$= Z_{tu,rs} \{A_{rs}A_{tu} - D_{rs}D_{tu}\} - i\{D_{tu}A_{rs} + A_{tu}D_{rs}\} \quad (6.22)$$

This indicates that both the real and imaginary parts of the spectrum have mixed phases, along both the frequency axes. Figure 6.5 shows the appearances of the peaks for different peak shapes along the $F1$ and $F2$ axes. Absorptive peak shapes produce the highest resolution in the spectra and thus are preferred.

The time domain signal can be classified into two categories:

- (1) The evolution in t_1 modulates the phase of the detected signal (e.g., $e^{i\omega_{tu}t_1} \cdot f(t_2)$). This is called phase modulation.
- (2) The evolution in t_1 modulates the amplitude of the detected signal (e.g., $\cos\omega_{tu}t_1 \cdot f(t_2)$). This is called amplitude modulation.

Several methods have been designed to obtain pure absorptive spectra, and the most common is to perform real Fourier transformation with respect to t_1 . We show how absorptive lines can be obtained when the detected signal is amplitude modulated by evolution during t_1 .

Consider

$$S_{tu,rs}(t_1, t_2) = \cos\omega_{tu}t_1 \cdot e^{-i\omega_{rs}t_2} \cdot e^{-\lambda_{tu}t_1 - \lambda_{rs}t_2} \quad (6.23)$$

Real cosine Fourier transformation of this data is given by

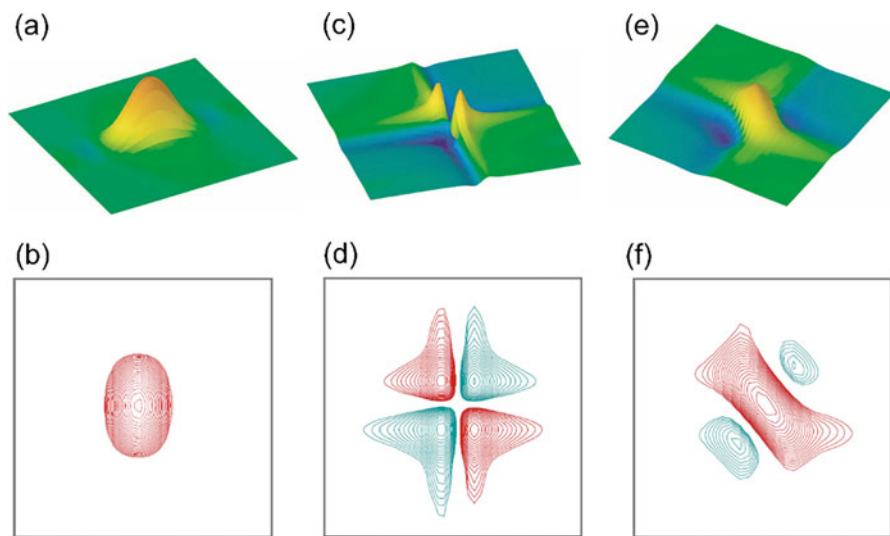


Fig. 6.5 Peak shapes in the two-dimensional spectra. Top row shows stacked plot representations, while the bottom row represents the corresponding contour representations of the same peak shapes. The left peak represents absorptive shape along both the frequency axes. The central picture represents dispersive line shapes along both the frequency axes, and the right picture represents absorptive along $F2$ and dispersive along $F1$ axes; the reverse is also possible. Such mixed line shapes are referred to as “mixed phases”

$$S_{tu,rs}(\omega_1, \omega_2) = \int_0^\infty \int_0^\infty S_{tu,rs}(t_1, t_2) \cos \omega_1 t_1 \cdot e^{-i\omega_2 t_2} dt_1 dt_2 \quad (6.24)$$

This leads to

$$S_{tu,rs}(\omega_1, \omega_2) = \frac{1}{2} \{A_{tu}(\omega_1) + A_{tu}(-\omega_1)\} \{A_{rs}(\omega_2) - iD_{rs}(\omega_2)\} \quad (6.25)$$

If the real part of the spectrum along ω_2 is selected, one can obtain pure absorptive peak along both frequency axes.

This, however, results in the duplication of peaks at $\pm\omega_{tu}$, which is artificial. So, this can be avoided by doing quadrature detection along the t_1 axis, as discussed in the next section.

6.5 Quadrature Detection in Two-Dimensional NMR

Here we need to consider how positive and negative frequencies can be discriminated in both $F1$ and $F2$ dimensions of the two-dimensional experiment. As far as $F2$ dimension is concerned, it comes from the detected signal during the t_2 time period, and the procedures described in Chap. 3 are applicable here as well. However, along the $F1$ dimension, there is a difficulty because the data is not

Table 6.1 Protocols for data collection in the three methods of quadrature detection along the F1 axis

<i>(a) TPPI (time proportional phase incrementation)</i>			
Experiment no.	Increment	Pulse phase	Receiver phase
$(4k + 1)$	$t_1(0) + (4k)\Delta$	x	x
$(4k + 2)$	$t_1(0) + (4k + 1)\Delta$	y	x
$(4k + 3)$	$t_1(0) + (4k + 2)\Delta$	$-x$	x
$(4k + 4)$	$t_1(0) + (4k + 3)\Delta$	$-y$	x

The index $k = 0, 1, 2, \dots, (N/4) - 1$; N is the total number of experiments along the t_1 dimension; $\Delta = 1/(2SW_1)$; $t_1(0) =$ ideally zero, but practically a few microseconds.

<i>(b) States</i>			
Experiment no.	Increment	Pulse phase	Receiver phase
$(4k + 1)$	$t_1(0) + (4k)2\Delta$	x	x
$(4k + 2)$	$t_1(0) + (4k)2\Delta$	y	x
$(4k + 3)$	$t_1(0) + (4k + 1)2\Delta$	x	x
$(4k + 4)$	$t_1(0) + (4k + 1)2\Delta$	y	x

The index $k = 0, 1, 2, \dots, (N/4) - 1$; N is the total number of experiments along the t_1 dimension; $\Delta = 1/(2SW_1)$; $t_1(0) =$ ideally zero, but practically a few microseconds.

<i>(c) States-TPPI</i>			
Experiment no.	Increment	Pulse phase	Receiver phase
$(4k + 1)$	$t_1(0) + (4k)2\Delta$	x	x
$(4k + 2)$	$t_1(0) + (4k)2\Delta$	y	x
$(4k + 3)$	$t_1(0) + (4k + 1)2\Delta$	$-x$	$-x$
$(4k + 4)$	$t_1(0) + (4k + 1)2\Delta$	$-y$	$-x$

The index $k = 0, 1, 2, \dots, (N/4) - 1$; N is the total number of experiments along the t_1 dimension; $\Delta = 1/(2SW_1)$; $t_1(0) =$ ideally zero, but practically a few microseconds.

actually collected during the “ t_1 ” period. Different strategies are adopted for this purpose, by manipulating the way the increments in t_1 are adjusted along with the receiver phases. There are three methods which are known to achieve this, and these are described in Table 6.1 (Cavanagh page 323, in this table, the pulse phase refers to the phase of the pulse immediately prior to the t_1 evolution period). For the TPPI method, the increment Δt_1 is half of that in STATES and TPPI-STATES methods.

6.6 Types of Two-Dimensional NMR Spectra

The known two-dimensional NMR experiments can be broadly classified into three categories:

- (i) Resolution/separation experiments
- (ii) Correlation experiments
- (iii) Multiple-quantum experiments

Hybrid experiments have also been devised which use some of the ideas in two different classes of experiments.

6.6.1 Two-Dimensional Resolution/Separation Experiments

The primary aim in these experiments is to separate the different interactions in the Hamiltonian. In high-resolution NMR, this amounts to the separation of the Zeeman (\mathcal{H}_z) and the coupling Hamiltonians (\mathcal{H}_J).

$$\mathcal{H} = \mathcal{H}_z + \mathcal{H}_J \quad (6.26)$$

Different strategies can be defined depending upon the nature of the information required in the final spectrum.

6.6.1.1 Two-Dimensional Heteronuclear Separation Experiments

Figure 6.6 illustrates such a concept (pulse sequences a and b). In (a), the $F2$ axis of the final spectrum contains both ^{13}C chemical shift and ^{13}C - ^1H coupling information, whereas the $F1$ axis contains only the ^{13}C chemical shift information. In (b), the reverse occurs, i.e., the $F1$ axis has both ^{13}C chemical shift and ^{13}C - ^1H coupling constants, while the $F2$ axis has only ^{13}C chemical shift information. This was the first two-dimensional experiment ever recorded. Figure 6.7 shows an experimental spectrum corresponding to Fig. 6.6b.

Figure 6.8 illustrates another situation where the $F1$ axis has only scalar coupling constants and the $F2$ axis has the chemical shift information. This represents a complete separation of the coupling and chemical shift Hamiltonians along the two axes.

The product operator description of the experiment is explicitly given in the following paragraphs.

The density operator (ρ) terms at the time points 1 to 3 indicated in Fig. 6.8 are

$$\rho_1 = C_z \quad (6.27)$$

$$\rho_2 = -C_y \quad (6.28)$$

$$\rho_3 = -[C_y \cos \pi J_{HC} t_1 - 2C_x H_z \sin \pi J_{HC} t_1] \quad (6.29)$$

The terms C_x , C_y , and C_z refer to the x -, y -, and z -components of the ^{13}C magnetization. And $2C_x H_z$ represents x -magnetization of carbon antiphase with respect to proton. In Eq. 6.29, the second term does not lead to observable magnetization in t_2 because of proton decoupling. The first term evolves under chemical shift only during t_2 .

Therefore,

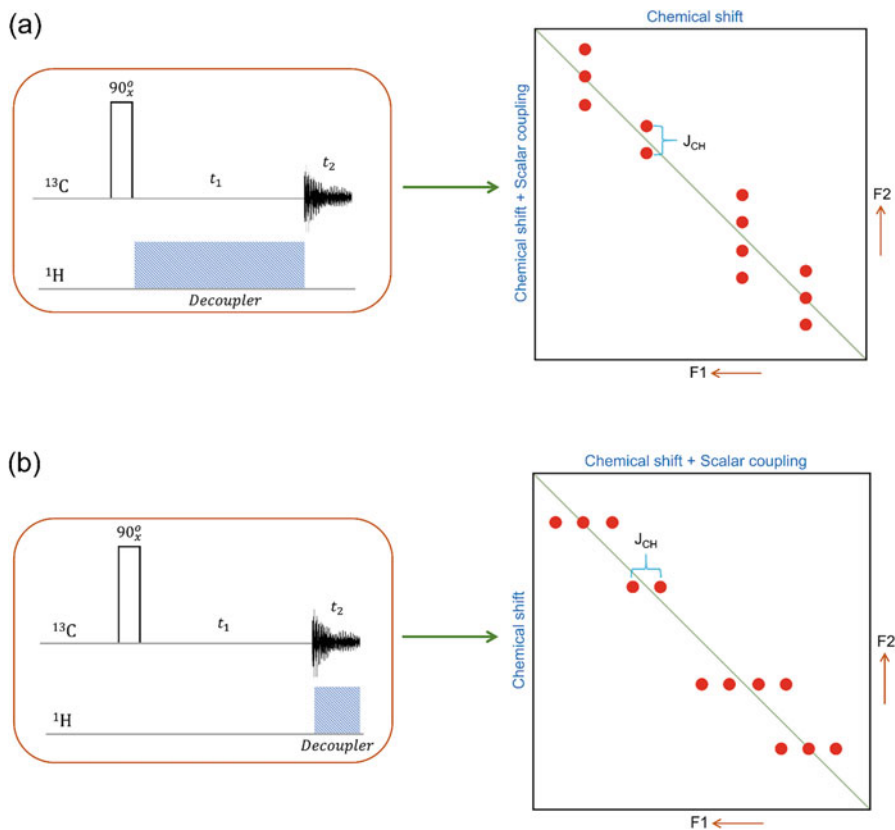


Fig. 6.6 Two-dimensional experiments, where the ^{13}C chemical shift and ^{13}C - ^1H coupling constants are separated on the F_1 and F_2 dimensions. In (a) the F_2 axis has both chemical shifts and coupling constants, while the F_1 axis has only chemical shifts. The reverse is true in (b)

$$C_y \xrightarrow{\mathcal{H}_Z} [C_y \cos\omega_C t_2 - C_x \sin\omega_C t_2] \quad (6.30)$$

Then, assuming y-detection, the density operator at time point 4 in Fig. 6.8 is

$$\rho_4 = C_y \cos\omega_C t_2 \cos\pi J_{\text{HC}} t_1 \quad (6.31)$$

This leads to exclusively coupling information along t_1 and chemical shift information along t_2 .

The experimental spectrum corresponding to this pulse scheme is shown in Fig. 6.9.

6.6.1.2 Two-Dimensional Homonuclear Separation Experiments

Figure 6.10 shows a pulse scheme for obtaining the separation of interactions in homonuclear systems. This is often referred to as two-dimensional J-resolved

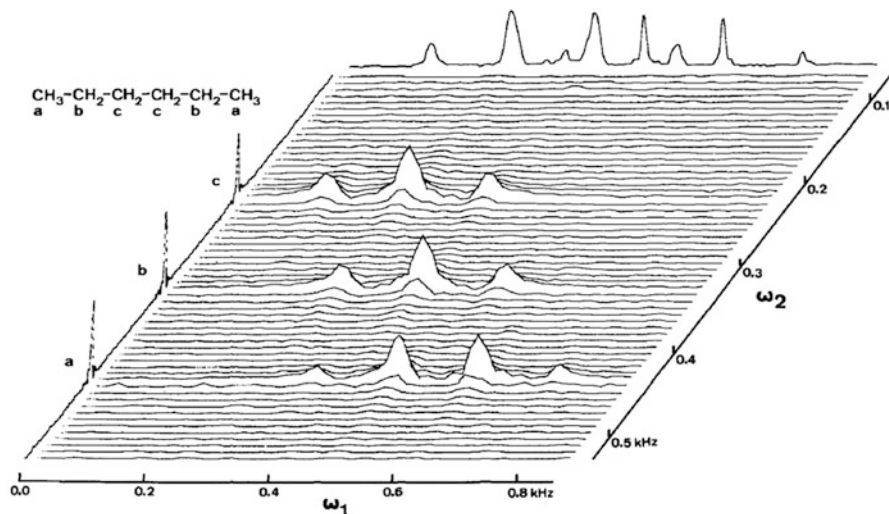


Fig. 6.7 Experimental spectrum demonstrating the scheme in Fig. 6.6b. (Reproduced from J. Chem. Phys. 63, 5490 (1975), with the permission of AIP Publishing)

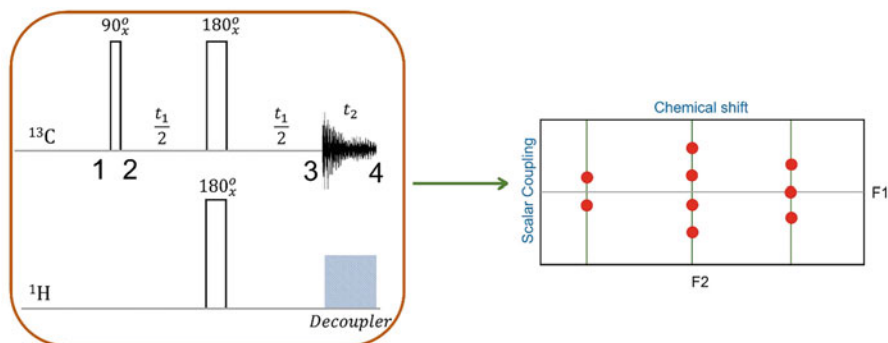


Fig. 6.8 Schematic of ^{13}C chemical shift and ^{13}C - ^1H scalar coupling separation in the two-dimensional spectrum. The $F2$ axis displays ^{13}C chemical shifts, while the $F1$ axis displays the multiplicity at each carbon site. See text for more details

(JRES) experiment. The pulse sequence can be analyzed using the product operator formalism.

For a weakly coupled two-spin system (k and l , $I = 1/2$), the density operator terms at different time points along the pulse sequence are

$$\rho_1 = I_{kz} + I_{lz} \quad (6.32)$$

Fig. 6.9 Experimental two-dimensional J-resolved NMR spectrum of cholesterol displaying the separation of ^{13}C chemical shift and ^{13}C - ^1H scalar coupling, along the F_2 and F_1 dimensions, respectively. (Reproduced from *J. Magn. Reson.* 29, 587 (1978), with the permission from Elsevier Publishing)

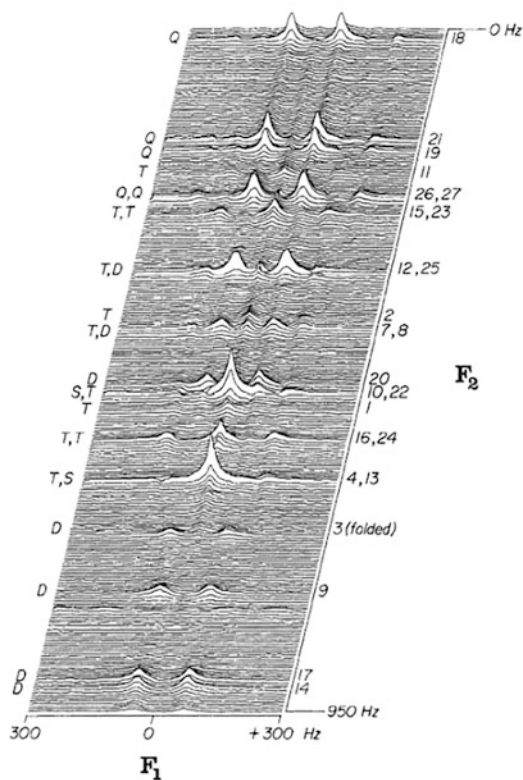
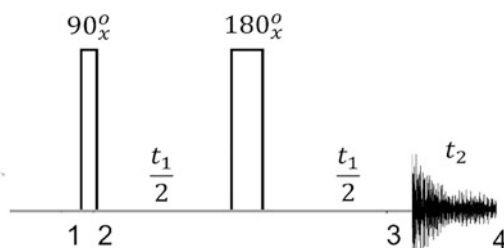


Fig. 6.10 Schematic of the two-dimensional J-resolved pulse sequence. Numbers 1–4 indicate the time points at which the density operators are calculated (see text)



$$\rho_2 = -(I_{ky} + I_{ly}) \quad (6.33)$$

During the next spin echo period chemical shifts are refocused, and thus spins evolve under the scalar coupling Hamiltonian (H_J) only. Explicitly the evolutions of product operators are shown for spin k only. Similar calculations apply for the spin l as well. Now, ρ_2 evolves under scalar coupling during the spin echo (t_1) and during the detection period t_2 , thus for the total time period t_1+t_2 .

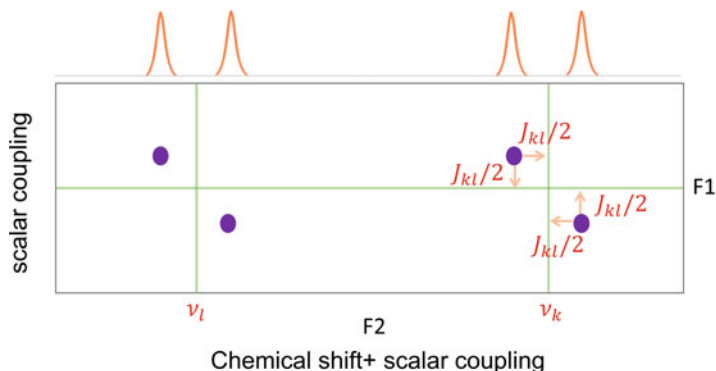


Fig. 6.11 Schematic two-dimensional JRES for a two-spin system. Projection shown on the top represents the one-dimensional spectrum

$$-I_{ky} \xrightarrow{\mathcal{H}_J} -I_{ky} \cos \pi J_{kl}(t_1 + t_2) + 2I_{kx}I_{lz} \sin \pi J_{kl}(t_1 + t_2) \quad (6.34)$$

In this equation the second term which represents antiphase magnetization is not observable during t_2 period. So, considering the chemical shift evolution of the first term during t_2 , one gets

$$-\cos \pi J_{kl}(t_1 + t_2)I_{ky} \xrightarrow{\mathcal{H}_z} -\cos \pi J_{kl}(t_1 + t_2) \{I_{ky} \cos \omega_k t_2 - I_{kx} \sin \omega_k t_2\} \quad (6.35)$$

Assuming y-detection, the signal is proportional to

$$-\cos \pi J_{kl}(t_1 + t_2) \cos \omega_k t_2 \quad (6.36)$$

$$= -\{ \cos \pi J_{kl} t_1 \cos \pi J_{kl} t_2 - \sin \pi J_{kl} t_1 \sin \pi J_{kl} t_2 \} \cos \omega_k t_2 \quad (6.37)$$

We see that along the t_2 axis, there are both chemical shifts and coupling constants, whereas along the t_1 axis, there is only scalar coupling information. This results in a spectrum of the type shown in Fig. 6.11. The peaks align themselves at an angle of 45° with respect to the $F2$ axis. The detected signal has both cosine and sine modulations along both t_1 and t_2 axes. The cosine modulation results in an absorptive shape, while the sine modulation results in dispersive line shape, after Fourier transformation. Thus, the peaks will have mixed phases. This requires a magnitude mode calculation of the spectra. Such calculation can be extended to multi-spin systems as well. An experimental spectrum demonstrating these features is shown in Fig. 6.12.

In Figs. 6.11 and 6.12, we notice that the coupling information is present along both axes, and it would be desirable to have a complete separation of the chemical shift and coupling information. This can be achieved by performing a shearing transformation on the peaks as indicated schematically in Fig. 6.13.

Fig. 6.12 A section of the experimental two-dimensional JRES spectrum for a multi-spin system, artemisinin

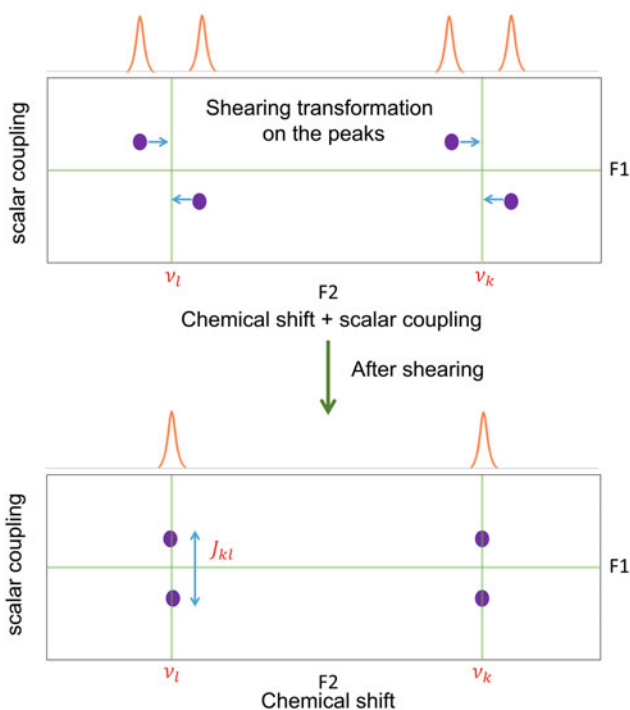
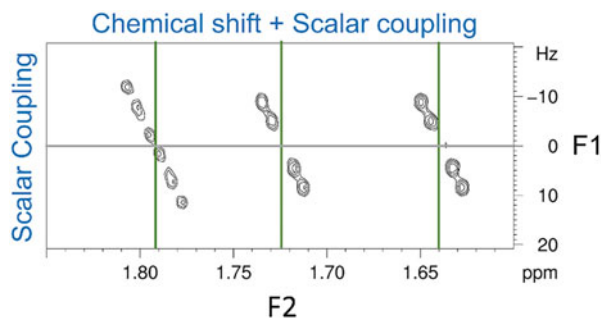
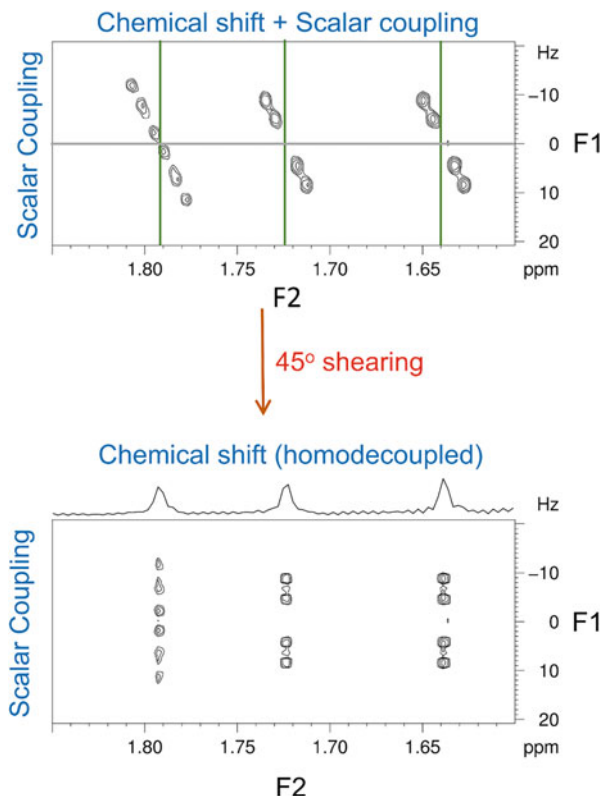


Fig. 6.13 Shearing transformation on the peaks in the two-dimensional J-resolved spectrum. The shearing transformation eliminates the coupling information along the $F2$ (horizontal axis, bottom picture)

Figure 6.14 shows the result of a shearing transformation in an experimental spectrum of a multi-spin system demonstrating the complete separation of the chemical shift and scalar coupling information along the $F2$ and $F1$ axes, respectively.

Fig. 6.14 A section of the experimental spectrum of artemisinin demonstrating the effect of shearing transformation



Interestingly, the projection of the spectrum on the $F2$ axis shows a completely homodecoupled spectrum of the spin system. This is an interesting way of achieving broadband homonuclear decoupling in complex spin systems. Along the $F1$ axis, the resolution is sufficiently high because of the small spectral width; therefore, the coupling constants can be measured very precisely. Further, because of the spin echo in the t_1 period, the external magnetic field inhomogeneity effects of line broadening are eliminated, which enhances the resolution along the $F1$ dimension. This technique has been extremely useful in separating out the multiplets in complex spin systems and measure accurately the various coupling constants.

6.6.2 Two-Dimensional Correlation Experiments

These experiments are designed to correlate two frequencies in a given one-dimensional spectrum with regard to various interactions between the spin systems in a molecule under consideration. The very first experiment in this context was proposed by Jean Jeener. This experiment has been popularly known as correlated spectroscopy or COSY.

6.6.2.1 The COSY Experiment

The pulse sequence for the COSY experiment is shown in Fig. 6.15.

Here the first pulse acts as the preparation period which is followed by the evolution period t_1 . The second pulse acts as the mixing period of the generalized scheme given in Fig. 6.1. The detailed mathematical analysis of the working of this pulse sequence is described in the following paragraphs.

COSY of Two Spins

Consider a system of two weakly coupled spins, k and l (with $I = 1/2$). They are J -coupled with a coupling constant of J_{kl} . The density operator of the spin system at the beginning of the experiment, ρ_1 , is

$$\rho_1 = I_{kz} + I_{lz} \quad (6.38)$$

For illustration, we calculate the evolution of I_{kz} through the pulse sequence explicitly, and the same can be extrapolated to I_{lz} , as well.

Following the convention of rotations described in Chap. 5, the density operator ρ_2 at time point 2 in the pulse sequence, for the spin k , is

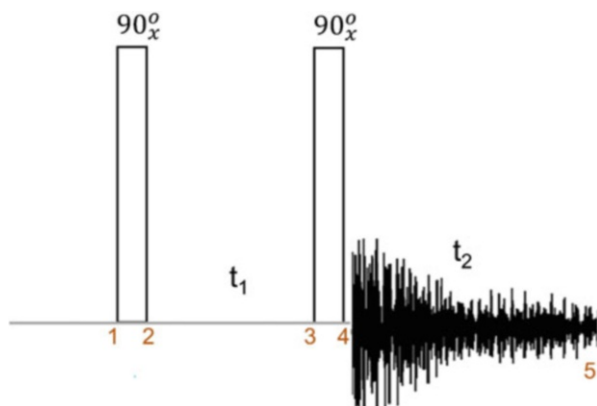
$$\rho_2 = -I_{ky} \quad (6.39)$$

This evolves under the Zeeman Hamiltonian ($\omega_k I_{kz}$), for a period t_1 yielding the density operator ρ_3 , at time point 3 in the pulse sequence.

$$\rho_3 = -(I_{ky} \cos \omega_k t_1 - I_{kx} \sin \omega_k t_1) \quad (6.40)$$

Next, considering evolution under the J -coupling Hamiltonian ($2\pi J_{kl} I_{kz} I_{lz}$), the density operator will be ρ_3' :

Fig. 6.15 Schematic pulse sequence of the COSY experiment. Numbers 1–5 indicate the time points at which the density operator calculations are reported (see text)



$$\begin{aligned} \rho_3' = & - \left\{ \left[\mathbf{I}_{ky} \cos \pi J_{kl} t_1 - 2 \mathbf{I}_{kx} \mathbf{I}_{lz} \sin \pi J_{kl} t_1 \right] \cos \omega_k t_1 \right. \\ & \left. - \left[\mathbf{I}_{kx} \cos \pi J_{kl} t_1 + 2 \mathbf{I}_{ky} \mathbf{I}_{lz} \sin \pi J_{kl} t_1 \right] \sin \omega_k t_1 \right\} \end{aligned} \quad (6.41)$$

The last pulse transforms these operators to yield a density operator ρ_4 , at time point 4 of the pulse sequence.

$$\begin{aligned} \rho_4 = & - \left\{ \left[\mathbf{I}_{kz} \cos \pi J_{kl} t_1 + 2 \mathbf{I}_{kx} \mathbf{I}_{ly} \sin \pi J_{kl} t_1 \right] \cos \omega_k t_1 \right. \\ & \left. - \left[\mathbf{I}_{kx} \cos \pi J_{kl} t_1 - 2 \mathbf{I}_{kz} \mathbf{I}_{ly} \sin \pi J_{kl} t_1 \right] \sin \omega_k t_1 \right\} \end{aligned} \quad (6.42)$$

Since the data is collected soon after, one needs to look at only those terms in the density operator which are observable as per definitions given in Chap. 5 ($Tr[\mathbf{I}_x \mathbf{B}(-s)] \neq 0$). Thus, the observable part of ρ_4 is ρ_4^{obs} :

$$\rho_4^{\text{obs}} = \left[\mathbf{I}_{kx} \cos \pi J_{kl} t_1 - 2 \mathbf{I}_{kz} \mathbf{I}_{ly} \sin \pi J_{kl} t_1 \right] \sin \omega_k t_1 \quad (6.43)$$

The first term in Eq. 6.43 which represents x -magnetization of the k spin evolves during the t_2 period with frequencies characteristic of k spin. Therefore, this will produce a diagonal peak ($F1 = F2 = \omega_k$) in the final two-dimensional spectrum. The second term which represents y -magnetization of l spin evolves during the t_2 period with frequencies characteristic of l spin. Therefore, this term will produce a “cross-peak” ($F1 = \omega_k$; $F2 = \omega_l$). Both these peaks will have fine structures, which contain the coupling information.

We now calculate the evolution of the terms in Eq. 6.43 during the t_2 time period. Here again both chemical shift and coupling evolutions have to be considered explicitly.

The first (diagonal peak) term in Eq. 6.43:

Chemical shift evolution leads to the density operator ρ_{5d} given by

$$\rho_{5d} = \left[\mathbf{I}_{kx} \cos \omega_k t_2 + \mathbf{I}_{ky} \sin \omega_k t_2 \right] f_d(t_1) \quad (6.44)$$

where $f_d(t_1) = \cos \pi J_{kl} t_1 \sin \omega_k t_1$.

Evolution under coupling generates the density operator ρ_{5d}' given by

$$\begin{aligned} \rho_{5d}' = & \left\{ \left[\mathbf{I}_{kx} \cos \pi J_{kl} t_2 + 2 \mathbf{I}_{ky} \mathbf{I}_{lz} \sin \pi J_{kl} t_2 \right] \cos \omega_k t_2 \right. \\ & \left. + \left[\mathbf{I}_{ky} \cos \pi J_{kl} t_2 - 2 \mathbf{I}_{kx} \mathbf{I}_{lz} \sin \pi J_{kl} t_2 \right] \sin \omega_k t_2 \right\} f_d(t_1) \end{aligned} \quad (6.45)$$

Assuming that we measure the y -magnetization, the observable signal is given by $Tr[\rho_{5d}' \mathbf{I}_{ky}]$.

$$Tr[\rho_{5d}' \mathbf{I}_{ky}] = \cos \pi J_{kl} t_2 \sin \omega_k t_2 f_d(t_1)$$

$$= \cos \pi J_{kl} t_2 \sin \omega_k t_2 \cos \pi J_{kl} t_1 \sin \omega_k t_1 \quad (6.46)$$

Explicitly this will lead to the following terms:

$$\begin{aligned} Tr[\rho_{5d}' I_{ky}] &= \frac{1}{4} \{ \sin(\omega_k + \pi J_{kl}) t_2 + \sin(\omega_k - \pi J_{kl}) t_2 \} \{ \sin(\omega_k + \pi J_{kl}) t_1 \\ &\quad + \sin(\omega_k - \pi J_{kl}) t_1 \} \end{aligned} \quad (6.47)$$

This contributes to the detected FID.

The two-dimensional real Fourier transformation along the t_1 and t_2 dimensions leads to four peaks with a dispersive line shapes at the following frequencies (Hz).

$$\begin{aligned} (F1, F2) &= \left[\left(\nu_k + \frac{J_{kl}}{2} \right), \left(\nu_k + \frac{J_{kl}}{2} \right) \right]; \text{positive, dispersive} \\ &\left[\left(\nu_k + \frac{J_{kl}}{2} \right), \left(\nu_k - \frac{J_{kl}}{2} \right) \right]; \text{positive, dispersive} \\ &\left[\left(\nu_k - \frac{J_{kl}}{2} \right), \left(\nu_k + \frac{J_{kl}}{2} \right) \right]; \text{positive, dispersive} \\ &\left[\left(\nu_k - \frac{J_{kl}}{2} \right), \left(\nu_k - \frac{J_{kl}}{2} \right) \right]; \text{positive, dispersive} \end{aligned} \quad (6.48)$$

This results in a fine structure for the diagonal peak as indicated in Fig. 6.16. *The second (cross-peak) term in Eq. 6.43:*

Here, let us consider the J-evolution first. This leads to the density operator ρ_{5c} :

$$\rho_{5c} = [2\mathbf{I}_{kz} \mathbf{I}_{ly} \cos \pi J_{kl} t_2 - \mathbf{I}_{lx} \sin \pi J_{kl} t_2] f_c(t_1) \quad (6.49)$$

$$f_c(t_1) = \sin \pi J_{kl} t_1 \sin \omega_k t_1 \quad (6.50)$$

Next, considering the shift evolution, we get ρ_{5c}' as

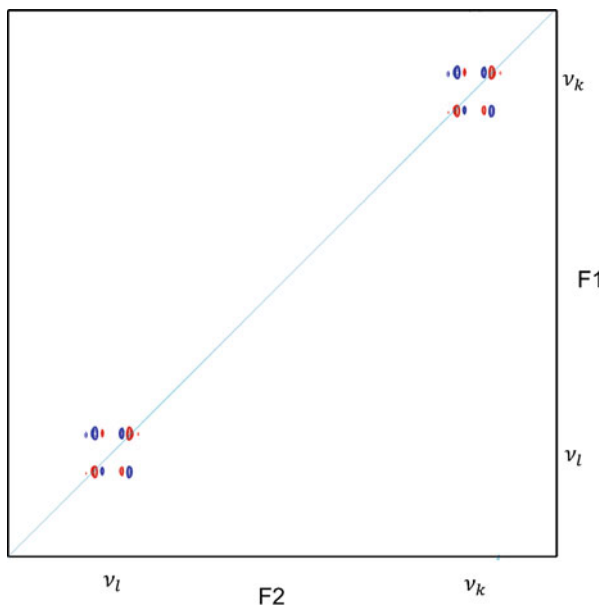
$$\begin{aligned} \rho_{5c}' &= \{ 2\mathbf{I}_{kz} [\mathbf{I}_{ly} \cos \omega_l t_2 - \mathbf{I}_{lx} \sin \omega_l t_2] \cos \pi J_{kl} t_2 \\ &\quad - [\mathbf{I}_{lx} \cos \omega_l t_2 + \mathbf{I}_{ly} \sin \omega_l t_2] \sin \pi J_{kl} t_2 \} f_c(t_1) \end{aligned} \quad (6.51)$$

Again, assuming that we measure the y-magnetization, the observable signal is given by $Tr[\rho_{5c}' I_{ly}]$:

$$Tr[\rho_{5c}' I_{ly}] = \sin \omega_l t_2 \sin \pi J_{kl} t_2 \sin \omega_k t_1 \sin \pi J_{kl} t_1 \quad (6.52)$$

This leads to four absorptive peaks at the following coordinates.

Fig. 6.16 Typical fine structure of the diagonal peaks in the COSY spectrum. They have in-phase dispersive line shapes along both frequency axes



$$\begin{aligned}
 (F1, F2) &= \left[\left(\nu_k + \frac{J_{kl}}{2} \right), \left(\nu_l + \frac{J_{kl}}{2} \right) \right]; \text{ positive, absorptive} \\
 &\left[\left(\nu_k + \frac{J_{kl}}{2} \right), \left(\nu_l - \frac{J_{kl}}{2} \right) \right]; \text{ negative, absorptive} \\
 &\left[\left(\nu_k - \frac{J_{kl}}{2} \right), \left(\nu_l - \frac{J_{kl}}{2} \right) \right]; \text{ positive, absorptive} \\
 &\left[\left(\nu_k - \frac{J_{kl}}{2} \right), \left(\nu_l + \frac{J_{kl}}{2} \right) \right]; \text{ negative, absorptive} \quad (6.53)
 \end{aligned}$$

Similar expressions can be derived to obtain the peak list starting from the l spin magnetization. Thus, the overall two-dimensional spectrum for the $k-l$ spin system will look as shown in Fig. 6.17.

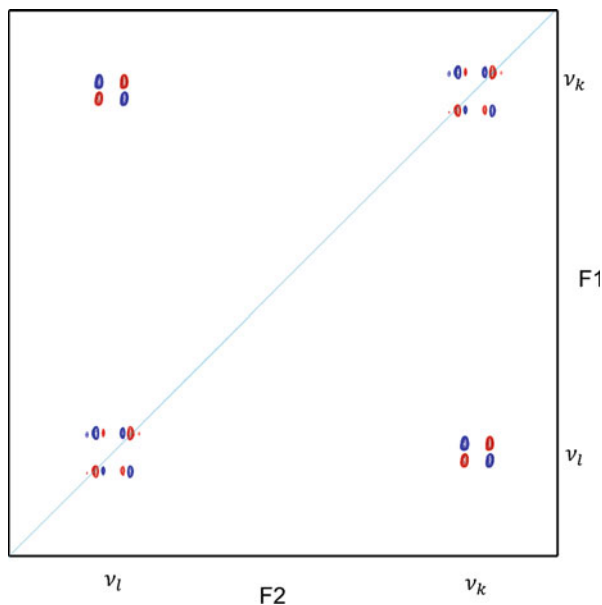
Figure 6.18 shows the phase-sensitive experimental spectrum of an AX sub-spin system of curcumin dissolved in CDCl_3 .

COSY of Three Spins

The detailed calculation shown for the two-spin system can be extrapolated to three-spin systems as well. The following considerations will help in arriving at the appropriate fine structures of the peaks.

- (i) The spectrum will have cross-peaks displaying the nature of the coupling network. For example, for a linear AMX system, there will be cross-peaks from A to M and M to X on one-side of the diagonal and M to A and X to M

Fig. 6.17 Schematic COSY NMR spectrum of a weakly coupled two-spin system. The cross-peaks have antiphase (+ and -) character and absorptive line shapes along both F2 and F1 axes. The diagonal peaks have in-phase dispersive line shapes along both axes



on the other side of the diagonal. All the three diagonal peaks will be present. However, there will be no A to X and X to A cross-peaks, as there is no coupling between A and X spins. Likewise, for a triangular coupling network, where all the three coupling constants are nonzero, there will be A to M, A to X, M to X, M to A, X to A, and X to M cross-peaks. Figure 6.19 shows the expected COSY spectra for linear and triangular coupling networks.

- (ii) Each cross-peak in the COSY spectrum arises as a result of the evolution under one particular coupling constant. For example, in an AMX spin system, the A to M (or M to A) cross-peak will result from the coupling J_{AM} . This coupling constant leads to a splitting where lines will have positive and negative signs, and this is called *active coupling*. The other coupling, for example, A to X, if it is nonzero, leads to in-phase splitting and is called the *passive coupling*. Accordingly, the fine structures in the cross-peaks will depend upon the relative magnitudes of the *active* and *passive* couplings. Figure 6.19 shows the fine structures for the A(F2) to M(F1) cross-peak for two different cases of J_{AM} and J_{AX} coupling constants in the linear AMX spin system (Fig. 6.20). Continuing along the same lines, the fine structure in the A(F1) to M(F2) cross-peak can be calculated, and this is shown in Fig. 6.21.

For the triangular coupling network of the three spins A, M, and X, the fine structures can be calculated for the individual cross-peaks following the same procedure described. This is explicitly shown for the A to M cross-peak in Fig. 6.22 for a particular choice of magnitudes of coupling constants. Notice once again that in this cross-peak, J_{AM} is the active coupling, while J_{MX} and J_{AX} are passive couplings.

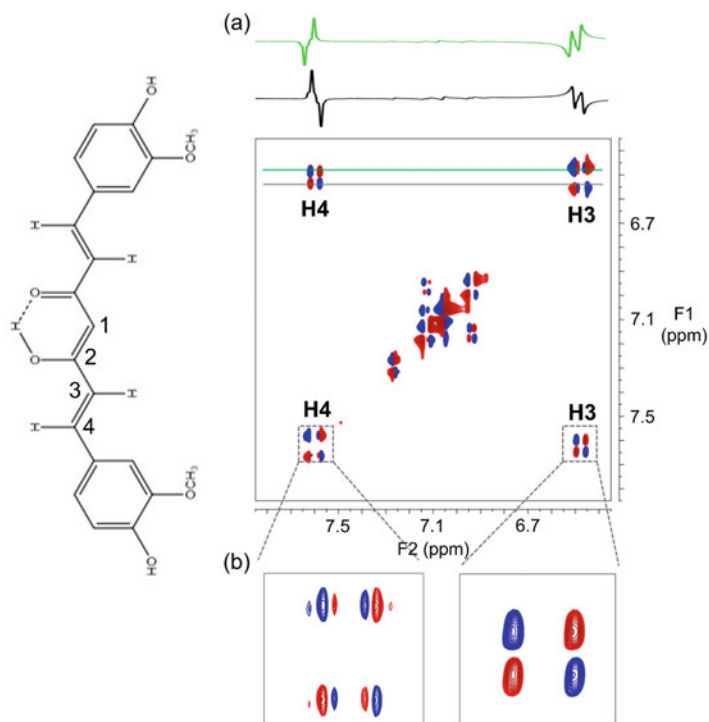


Fig. 6.18 (a) Phase-sensitive COSY spectrum of curcumin (AX sub-spin system) and (b) blowups of the cross- (right) and diagonal peaks (left). Horizontal cross-sections through the peaks at the gray- and green-colored lines are shown on the top

Disadvantages of COSY

The COSY experiment has the following disadvantages.

- (i) The dispersive line shapes in the diagonal peaks produce long tails which hamper the resolution in the spectra. The cross-peaks which lie close to the diagonal would get masked out.
- (ii) The diagonal peak has in-phase components, while the cross-peak has antiphase components. The resolution in the F1 dimension is determined by the number of increments one can acquire along the t_1 dimension, and this will be limited by the machine time. In that scenario, because of poor resolution along the F1 dimension, the peak intensities cancel because of the positive/negative character of the components in the cross-peak. On the other hand, the components in the diagonal peaks coadd because of the in-phase character. This results in huge diagonal peaks and tiny cross-peaks in the event of insufficient resolution in the spectrum.

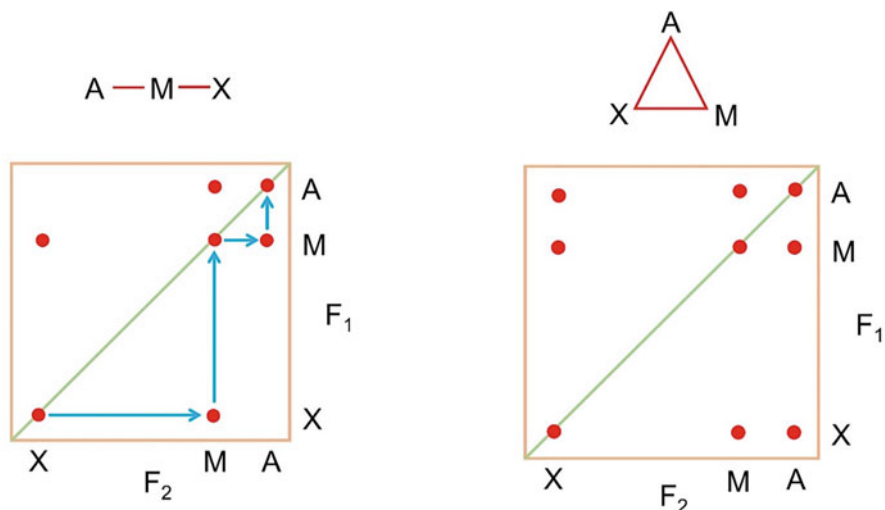


Fig. 6.19 Schematic appearance of the COSY spectrum for a system of three spins, AMX. The coupling patterns are shown on the top

6.6.2.2 Double-Quantum-Filtered COSY (DQF-COSY)

This experiment was designed to circumvent the limitations of the COSY experiment. The pulse sequence for the DQF-COSY is shown in Fig. 6.23.

The pulse sequence is similar to that of COSY up to the second pulse but for the fact that the phases (ϕ) of these two pulses need to be cycled and the data coadded or subtracted as discussed in the following. The scheme involves acquiring four transients with the pulse phase (ϕ) and the receiver phase (θ) incremented with every transient. This is indicated in Table 6.2.

The experiment can be analyzed in the same manner as was done for COSY. Considering a system of two weakly coupled spins (k , l), the density operator calculation follows the same steps as for COSY, and we rewrite the density operator at time point 4 of the pulse sequence:

$$\rho_4(\phi = x) = \left[-I_{kz} \cos \pi J_{kl} t_1 - 2I_{kx} I_{ly} \sin \pi J_{kl} t_1 \right] \cos \omega_k t_1 + \left[I_{kx} \cos \pi J_{kl} t_1 - 2I_{kz} I_{ly} \sin \pi J_{kl} t_1 \right] \sin \omega_k t_1 \quad (6.54)$$

Here the first two pulses are considered to be applied along the x axis ($\phi = x$). Repeating such an exercise with $\phi = y$ leads to the following density operator $\rho_4(y)$:

$$\rho_4(\phi = y) = \left[-I_{kz} \cos \pi J_{kl} t_1 + 2I_{ky} I_{lx} \sin \pi J_{kl} t_1 \right] \cos \omega_k t_1 + \left[I_{ky} \cos \pi J_{kl} t_1 + 2I_{kz} I_{lx} \sin \pi J_{kl} t_1 \right] \sin \omega_k t_1 \quad (6.55)$$

Similar calculations with $\phi = -x$ and $\phi = -y$ lead to the following density operators.

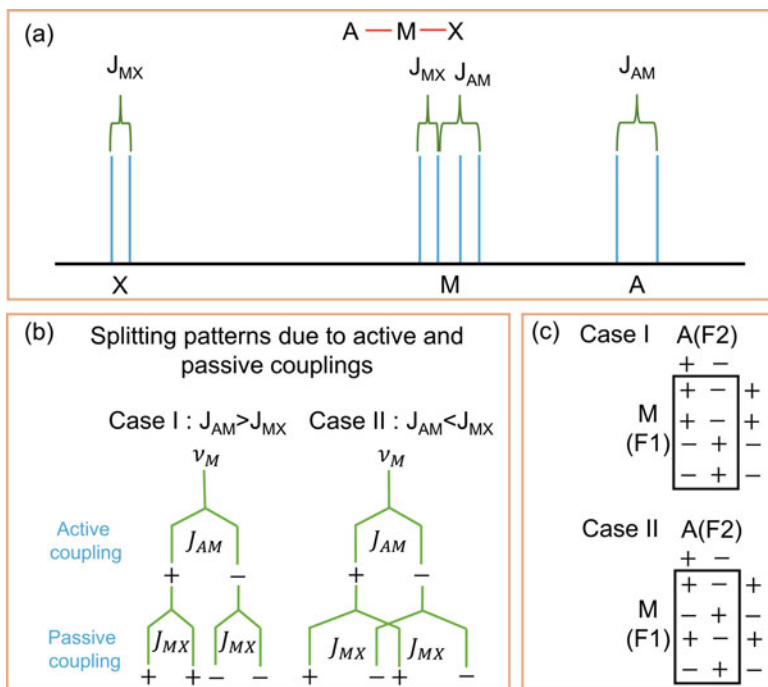


Fig. 6.20 (a) Fine structure in the one-dimensional spectrum for a linear AMX system. (b) Splitting patterns in the A-M cross-peak due to active and passive couplings for the M spin for two different cases of relative magnitudes of active and passive couplings. (c) The final fine structure in the cross-peak A(F2) to M(F1) in the COSY spectrum for the two cases considered in (b). Note that this peak lies in the lower triangle in the two-dimensional spectrum (Fig. 6.19)

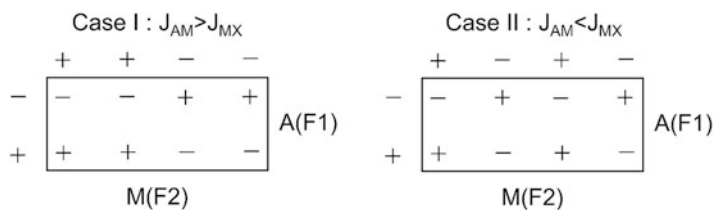


Fig. 6.21 Schematic fine structure in the A(F1) to M(F2) cross-peak. Note that this peak lies in the upper triangle in the two-dimensional spectrum (Fig. 6.19)

$$\rho_4(\phi = -x) = [-I_{kz} \cos \pi J_{kl} t_1 - 2I_{kx} I_{ly} \sin \pi J_{kl} t_1] \cos \omega_k t_1 + [-I_{kx} \cos \pi J_{kl} t_1 + 2I_{kz} I_{ly} \sin \pi J_{kl} t_1] \sin \omega_k t_1 \quad (6.56)$$

$$\rho_4(\phi = -y) = [-I_{kz} \cos \pi J_{kl} t_1 + 2I_{ky} I_{lx} \sin \pi J_{kl} t_1] \cos \omega_k t_1 + [-I_{ky} \cos \pi J_{kl} t_1 - 2I_{kz} I_{lx} \sin \pi J_{kl} t_1] \sin \omega_k t_1 \quad (6.57)$$

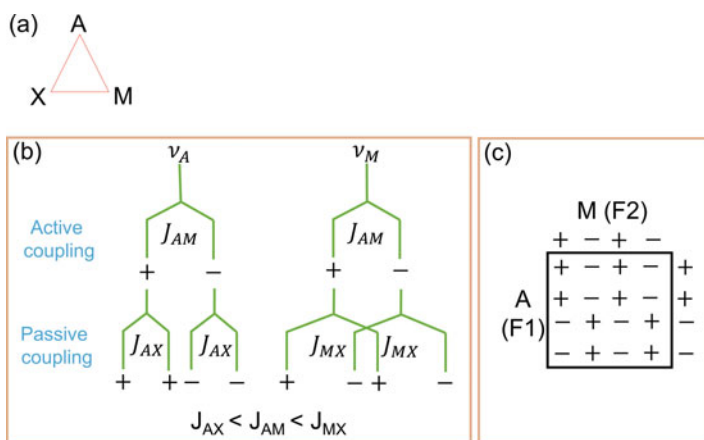


Fig. 6.22 (a) Schematic of triangular J-coupling network in the weakly coupled AMX system. (b) The splitting pattern of A and M spins due to active and passive coupling constants for a particular choice of their relative magnitudes. (c) Fine structure in the A to M cross-peak in the lower triangle of the COSY spectrum for the choice of coupling constants as in (b)

Fig. 6.23 Schematic of the DQF-COSY pulse sequence. Here, ϕ and θ refer to the phases of the pulses and the receiver, respectively. See text for more details. Numbers 1–5 indicate the time points at which the density operators are reported in the text

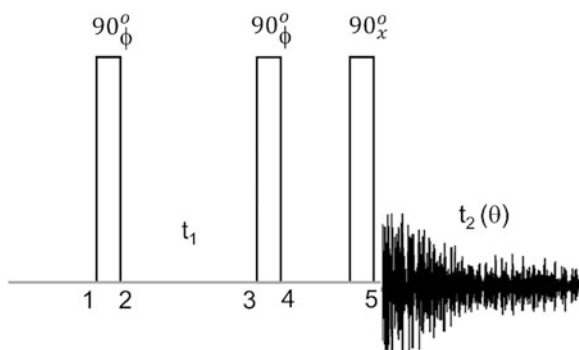


Table 6.2 Phase cycling for DQF-COSY pulse sequence

Scan no.	Pulse phase (ϕ)	Receiver phase (θ)
1	x	+
2	y	-
3	-x	+
4	-y	-

As per the receiver phase cycling the data is added or subtracted and then, the resultant density operator will be

$$\rho_4 = \rho_4(\phi = x) - \rho_4(\phi = y) + \rho_4(\phi = -x) - \rho_4(\phi = -y) \quad (6.58)$$

$$= -4(I_{ky}I_{lx} + I_{kx}I_{ly}) \sin \pi J_{kl}t_1 \cos \omega_k t_1 \quad (6.59)$$

The operators in Eq. 6.59 represent pure double-quantum coherences.

The third 90° pulse in the pulse sequence converts these terms into observable single-quantum coherences. The corresponding density operator ρ_5 will be

$$\rho_5 = -4 (I_{kz}I_{lx} + I_{kx}I_{lz}) \sin \pi J_{kl}t_1 \cos \omega_k t_1 \quad (6.60)$$

This now consists of antiphase magnetizations of both k and l spins with the same phase. They will evolve during the t_2 period into in-phase magnetizations of k and l spins, whereby it becomes observable. Rewriting Eq. 6.60,

$$\rho_5 = -4 (I_{kz}I_{lx} + I_{kx}I_{lz}) f(t_1) \quad (6.61)$$

$$f(t_1) = \sin \pi J_{kl}t_1 \cos \omega_k t_1 \quad (6.62)$$

Now evolve ρ_5 under \mathcal{H}_J and \mathcal{H}_z sequentially during t_2 ,

$$\begin{aligned} \rho_5 \xrightarrow{\mathcal{H}_J} & -2 \{ [2I_{kz}I_{lx} \cos(\pi J_{kl}t_2) + I_{ly} \sin(\pi J_{kl}t_2)] \\ & + [2I_{kx}I_{lz} \cos(\pi J_{kl}t_2) + I_{ky} \sin(\pi J_{kl}t_2)] \} f(t_1) \end{aligned} \quad (6.63)$$

The antiphase terms $2I_{kz}I_{lx}$ and $2I_{kx}I_{lz}$ are not observable and hence will not be considered further. The other terms will be evolved under the \mathcal{H}_z .

$$\begin{aligned} \xrightarrow{\mathcal{H}_z} & -2 \{ [I_{ly} \cos \omega_l t_2 - I_{lx} \sin \omega_l t_2] \sin(\pi J_{kl}t_2) \\ & + [I_{ky} \cos \omega_k t_2 - I_{kx} \sin \omega_k t_2] \sin(\pi J_{kl}t_2) \} f(t_1) \end{aligned} \quad (6.64)$$

Assuming y-detection, we have the following signal:

$$\text{Signal (S)} = -2 [\cos \omega_l t_2 \sin(\pi J_{kl}t_2) + \cos \omega_k t_2 \sin(\pi J_{kl}t_2)] \sin \pi J_{kl}t_1 \cos \omega_k t_1 \quad (6.65)$$

In this expression, the first term leads to the cross-peak, while the second term leads to the diagonal peak in the spectrum.

(a) Cross-peak

$$\begin{aligned} & \cos \omega_l t_2 \sin(\pi J_{kl}t_2) \sin \pi J_{kl}t_1 \cos \omega_k t_1 \\ &= \frac{1}{4} [\sin(\omega_k + \pi J_{kl})t_1 - \sin(\omega_k - \pi J_{kl})t_1] \\ & \quad [\sin(\omega_l + \pi J_{kl})t_2 - \sin(\omega_l - \pi J_{kl})t_2] \\ &= + \sin(\omega_k + \pi J_{kl})t_1 \sin(\omega_l + \pi J_{kl})t_2 \\ & \quad - \sin(\omega_k - \pi J_{kl})t_1 \sin(\omega_l - \pi J_{kl})t_2 \end{aligned} \quad (6.66)$$

$$\begin{aligned}
& - \sin(\omega_k - \pi J_{kl})t_1 \sin(\omega_l + \pi J_{kl})t_2 \\
& + \sin(\omega_k - \pi J_{kl})t_1 \sin(\omega_l - \pi J_{kl})t_2
\end{aligned} \tag{6.67}$$

This leads to the following peaks.

$$\begin{aligned}
(F1, F2) &= \left[\left(\nu_k + \frac{J_{kl}}{2} \right), \left(\nu_l + \frac{J_{kl}}{2} \right) \right]; \text{positive, dispersive} \\
& \left[\left(\nu_k + \frac{J_{kl}}{2} \right), \left(\nu_l - \frac{J_{kl}}{2} \right) \right]; \text{negative, dispersive} \\
& \left[\left(\nu_k - \frac{J_{kl}}{2} \right), \left(\nu_l + \frac{J_{kl}}{2} \right) \right]; \text{negative, dispersive} \\
& \left[\left(\nu_k - \frac{J_{kl}}{2} \right), \left(\nu_l - \frac{J_{kl}}{2} \right) \right]; \text{positive, dispersive}
\end{aligned} \tag{6.68}$$

A 90° phase shift will produce absorptive line shape for all the four peaks.

(b) Diagonal peak

$$\begin{aligned}
& \cos \omega_k t_2 \sin(\pi J_{kl} t_2) \sin \pi J_{kl} t_1 \cos \omega_k t_1 \\
&= \frac{1}{4} [\sin(\omega_k + \pi J_{kl})t_1 - \sin(\omega_k - \pi J_{kl})t_1] \cdot \\
& \quad [\sin(\omega_k + \pi J_{kl})t_2 - \sin(\omega_k - \pi J_{kl})t_2]
\end{aligned} \tag{6.69}$$

$$\begin{aligned}
&= + \sin(\omega_k + \pi J_{kl})t_1 \sin(\omega_k + \pi J_{kl})t_2 \\
& \quad - \sin(\omega_k + \pi J_{kl})t_1 \sin(\omega_k - \pi J_{kl})t_2 \\
& \quad - \sin(\omega_k - \pi J_{kl})t_1 \sin(\omega_k + \pi J_{kl})t_2 \\
& \quad + \sin(\omega_k - \pi J_{kl})t_1 \sin(\omega_k - \pi J_{kl})t_2
\end{aligned} \tag{6.70}$$

This leads to the following peaks:

$$\begin{aligned}
(F1, F2) &= \left[\left(\nu_k + \frac{J_{kl}}{2} \right), \left(\nu_k + \frac{J_{kl}}{2} \right) \right]; \text{positive, dispersive} \\
& \left[\left(\nu_k + \frac{J_{kl}}{2} \right), \left(\nu_k - \frac{J_{kl}}{2} \right) \right]; \text{negative, dispersive} \\
& \left[\left(\nu_k - \frac{J_{kl}}{2} \right), \left(\nu_k + \frac{J_{kl}}{2} \right) \right]; \text{negative, dispersive} \\
& \left[\left(\nu_k - \frac{J_{kl}}{2} \right), \left(\nu_k - \frac{J_{kl}}{2} \right) \right]; \text{positive, dispersive}
\end{aligned} \tag{6.71}$$

A 90° phase shift will produce absorptive line shape for all the four peaks.

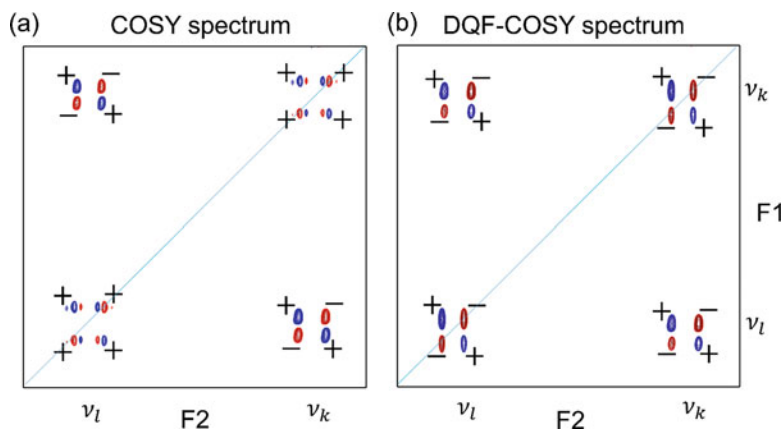


Fig. 6.24 Comparison of COSY and DQF-COSY spectra for a two-spin system. + and – indicate positive and negative signs of the peak components, respectively

Thus, the final spectrum for the two-spin system will appear as shown in Fig. 6.24. Clearly, the DQF-COSY spectrum shows better resolution than the COSY spectrum and is pretty clean in both the diagonal and cross-peaks.

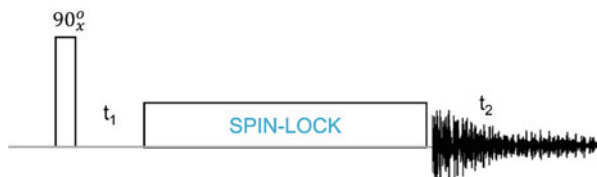
6.6.2.3 Total Correlation Spectroscopy (TOCSY)

The COSY and the DQF-COSY resulted in fine structures in diagonal as well as cross-peaks. The DQF-COSY circumvented the shortcomings of COSY with respect to the diagonal. However, the fine structures still retain the antiphase nature of the components in the cross-peaks. In essence, this amounts to a differential transfer of magnetization between the spins. The antiphase character results in the cancellation of component intensities in the cross-peaks in the absence of sufficient resolution. This problem is circumvented by total correlation spectroscopy (TOCSY) which results in in-phase components and thus achieves net transfer of magnetization between the spins. The pulse sequence for the TOCSY experiment is shown in Fig. 6.25.

The pulse sequence starts with a 90° pulse, which creates transverse magnetization which then evolves during the period t_1 with characteristic frequencies. The so-called mixing here consists of a strong RF field or a train of pulses (often referred to as composite pulses) during which time the spins are locked in the rotating frame in the transverse plane along the x or the y -axis. During the spin lock transfer of coherence occurs among the J-coupled spins. For a two-spin system, k and l (spin $1/2$), the effective Hamiltonian during the mixing period consists only of the J-coupling Hamiltonian, and the Zeeman interactions are eliminated. This Hamiltonian is given by

$$\mathcal{H}_e = 2\pi J I_k \cdot I_l \quad (6.72)$$

Fig. 6.25 Pulse sequence for the TOCSY experiment



$$= 2\pi J(I_{kz}I_{lz} + I_{kx}I_{lx} + I_{ky}I_{ly}) \quad (6.73)$$

The evolution of the magnetization components under the influence of this Hamiltonian is given by the following equation:

$$I_{kx} \xrightarrow{\mathcal{H}_{et}} I_{kx} \left(\frac{1 + \cos 2\pi Jt}{2} \right) + I_{lx} \left(\frac{1 - \cos 2\pi Jt}{2} \right) + (I_{ky}I_{lz} - I_{ly}I_{kz}) \sin 2\pi Jt \quad (6.74)$$

Complete transfer of magnetization will occur for time $t = 1/2J$. This is in contrast to INEPT transfer of coherence where a complete transfer requires a time $t = 1/J$; in the INEPT, the transfer occurs in two steps: the first step involving a spin-echo of period $1/2J$ causes antiphase transfer, and in the second step, a second spin echo of period $1/2J$ causes refocusing to generate in-phase magnetization ($I_{kx} \rightarrow 2I_{ly}I_{kz} \rightarrow I_{lx}$).

A similar equation can be written for the evolution of I_{lx} :

$$I_{lx} \xrightarrow{\mathcal{H}_{et}} I_{lx} \left(\frac{1 + \cos 2\pi Jt}{2} \right) + I_{kx} \left(\frac{1 - \cos 2\pi Jt}{2} \right) + (I_{ly}I_{kz} - I_{ky}I_{lz}) \sin 2\pi Jt \quad (6.75)$$

The addition of Eqs. 6.74 and 6.75 leads to the following:

$$(I_{kx} + I_{lx}) \xrightarrow{\mathcal{H}_{et}} (I_{kx} + I_{lx}) \quad (6.76)$$

This implies that the total x -magnetization is conserved through the mixing sequence, and there is in-phase transfer ($I_{kx} \rightarrow I_{lx}$ and vice versa), retaining the phase of the magnetization, i.e., $I_{kx} \rightarrow I_{lx}$, $I_{ky} \rightarrow I_{ly}$, and $I_{kz} \rightarrow I_{lz}$. Therefore, this mixing is termed as isotropic mixing, and the Hamiltonian is termed as isotropic Hamiltonian. After the mixing the magnetization components are detected in the t_2 time period. Two-dimensional Fourier transformation of the collected signal results in a two-dimensional spectrum.

Detailed calculations for multi-spin systems show that the general conclusions derived for the two-spin systems are valid for multi-spin systems as well. However, an interesting feature of this experiment is the following. Considering a linear three-spin system (AMX), where there is no coupling between the spins A and X, it turns out that there will be a cross-peak between the spins A and X, provided both AM

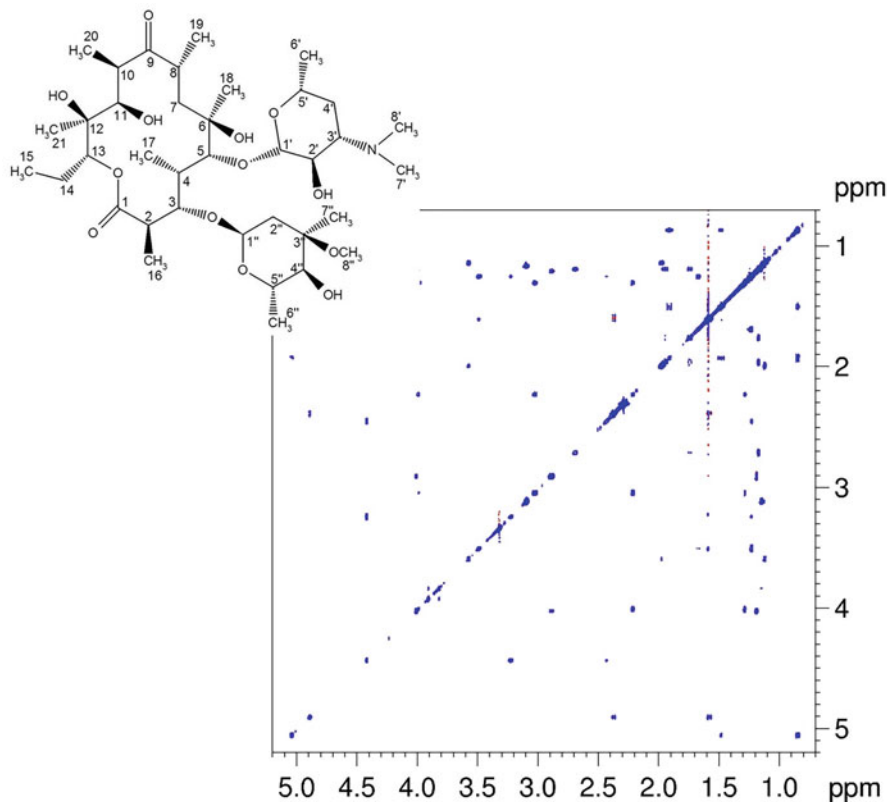


Fig. 6.26 Experimental TOCSY spectrum of erythromycin-A

coupling and MX coupling are nonzero. Thus, the TOCSY experiments relays magnetization through the network of coupled spins, providing valuable information about the coupling network in a given molecule. An experimental TOCSY spectrum is shown in Fig. 6.26.

Such a spectrum will enable to distinguish between a linear three-spin system, AMX, and a mixture of two two-spin systems AM and M'X with accidental degeneracy of the M and M' chemical shifts. In the latter case, there will be no cross-peak between A and X spins in the TOCSY spectrum, whereas the COSY or DQF-COSY will not be able to distinguish between these two situations.

6.6.2.4 Two-Dimensional Nuclear Overhauser Effect Spectroscopy (2D-NOESY)

This experiment represents an extension of the one-dimensional transient NOE to two dimensions. The pulse sequence for this is given in Fig. 6.27a. τ_m here is called the mixing time during which transfer of magnetization happens through dipolar interactions or the NOE effect. For uncoupled spin systems, the spin dynamics

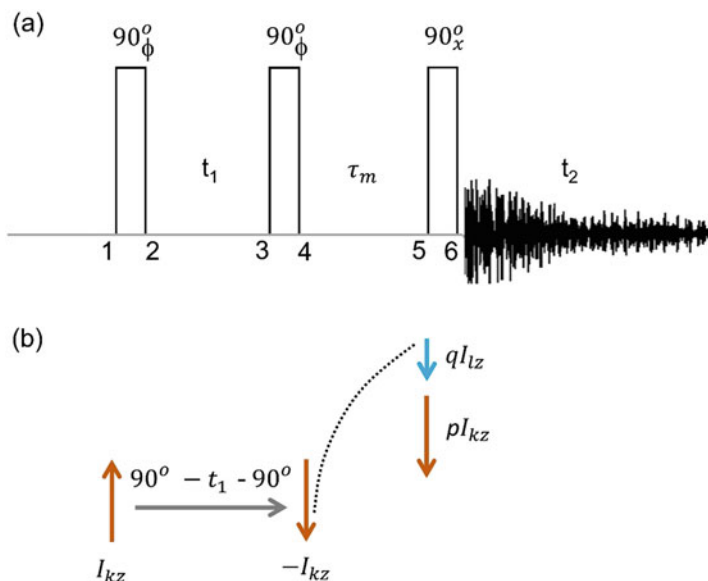


Fig. 6.27 (a) Pulse sequence of NOESY experiment. (b) Schematic of magnetization transfer between two spins (k and l). Numbers 1–6 are time points along the pulse sequence to facilitate discussion in the text

through the pulse sequence leading to transfer of magnetization is schematically shown in Fig. 6.27b.

For coupled spin systems, the pulse sequence can be analyzed by following the product operator formalism, as in the case of COSY. For a two-spin system, k and l (spin = 1/2), the density operator at time point 4 in the pulse sequence is given by

$$\rho_4 = \left[-I_{kz} \cos \pi J_{kl} t_1 - 2I_{kx} I_{ly} \sin \pi J_{kl} t_1 \right] \cos \omega_k t_1 + \left[I_{kx} \cos \pi J_{kl} t_1 - 2I_{kz} I_{ly} \sin \pi J_{kl} t_1 \right] \sin \omega_k t_1 \quad (6.77)$$

As demonstrated in the case of DQF-COSY, a phase cycling scheme is utilized to retain only the first term in Eq. 6.33. This is indicated in Table 6.3.

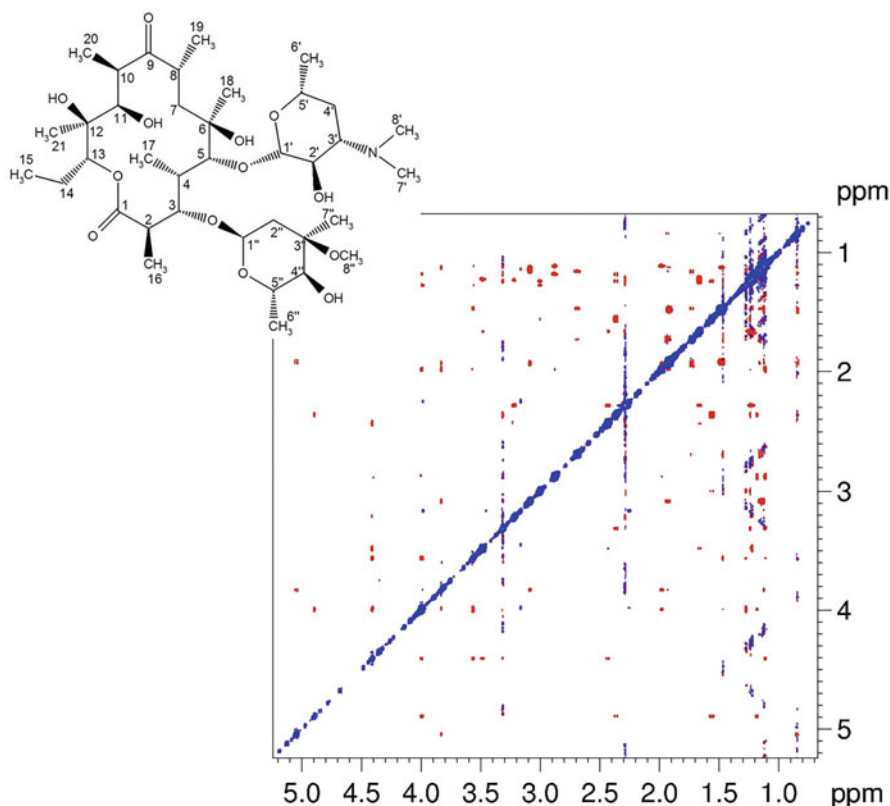
During the following period τ_m , transfer of z -magnetization occurs from spin k to spin l , as per the dipolar coupling-mediated relaxation of the spins (refer to Chap. 4). The final 90° pulse converts the z -magnetization into transverse magnetization for detection.

Since the transfer of magnetization during the mixing time is never complete, there will be magnetization components of both k and l spins (coupled or uncoupled) evolving during the detection period. These result in the diagonal and cross-peaks, respectively. Both diagonal and cross-peaks will have fine structure if the spins are J-coupled and the components will have in-phase character.

In multi-spin systems, transfer of magnetization will be governed by the relaxation matrix, as discussed in Chap. 4. There will be cross-peaks between every two

Table 6.3 Phase cycling for NOESY pulse sequence given in Fig. 6.27a

Scan	ϕ	Receiver
1	x	+
2	y	+
3	$-x$	+
4	$-y$	+

**Fig. 6.28** Experimental NOESY spectrum of erythromycin-A

spins which have dipolar coupling contributing to their relaxation. Thus, the NOESY spectrum represents the network of dipolar-coupled spins in a given molecule. The cross-peak intensities will depend upon respective cross-relaxation rates for short mixing times compared to the spin-lattice relaxation time (T_1). These, in turn, are proportional to the inverse sixth power of the internuclear distances; in a sense the cross-peak intensities reflect the NOEs observed in a transient NOE experiment (see Chap. 4). Thus, the NOESY spectrum reflects the distance matrix representing the three-dimensional structure of a given molecule. An illustrative experimental spectrum is shown in Fig. 6.28.

The NOESY pulse sequence also reflects transfer of magnetization through chemical exchange mechanism. During the mixing time, transfer of z -magnetization can also happen via chemical exchange process, wherever it is present. Thus, in such situations, the cross-peak and diagonal peak intensities can also be monitored as a function of the mixing time to derive the exchange rates. For a symmetrical two-site exchange $A \leftrightarrow B$, with equal populations at the two sites, equal spin-lattice relaxation rates, and equal transverse relaxation rates, the intensities of the diagonal (a_{AA} , a_{BB}) and cross-peaks (a_{AB} , a_{BA}) are given by the following equations:

$$a_{AA}(\tau_m) = a_{BB}(\tau_m) = \frac{1}{2} [1 + e^{-2k\tau_m}] e^{-\tau_m/T_1} \quad (6.78)$$

$$a_{AB}(\tau_m) = a_{BA}(\tau_m) = \frac{1}{2} [1 - e^{-2k\tau_m}] e^{-\tau_m/T_1} \quad (6.79)$$

where k is the exchange rate and T_1 is the spin-lattice relaxation time. Equilibrium magnetization at the two sites is assumed to be the same. Figure 6.29 shows the dependence of the diagonal and cross-peak intensities on the mixing time.

The ratio of diagonal-to-cross-peak intensities will be

$$\frac{a_{AA}}{a_{AB}} = \frac{1 + e^{-2k\tau_m}}{1 - e^{-2k\tau_m}} \quad (6.80)$$

For short mixing times ($k\tau_m \ll 1$), Eq. 6.80 reduces to

$$\frac{a_{AA}}{a_{AB}} = \frac{1 - k\tau_m}{k\tau_m} \quad (6.81)$$

Thus, by monitoring the intensity ratios as a function of τ_m , the exchange rates can be calculated.

6.6.2.5 Two-Dimensional ROESY

ROESY represents the Overhauser experiment in the rotating frame (ROE). The pulse sequence for this experiment is given in Fig. 6.30.

Here, the mixing process and the consequent magnetization transfer is brought about by low-power spin lock on the transverse magnetization. The magnetization transfer ($I_{kx} \rightarrow I_{lx}$) occurs via transverse cross-relaxation, and the evolution of the magnetization components during the mixing time (τ_m) can be shown to be as follows.

$$I_{kx}(\tau_m) = \left(1 - \frac{\tau_m}{T_2}\right) \sin(\omega_k t_1) I_{kz}^0 - \sigma \tau_m \sin(\omega_l t_1) I_{lz}^0 \quad (6.82)$$

$$I_{lx}(\tau_m) = \left(1 - \frac{\tau_m}{T_2}\right) \sin(\omega_l t_1) I_{lz}^0 - \sigma \tau_m \sin(\omega_k t_1) I_{kz}^0 \quad (6.83)$$

Fig. 6.29 Diagonal (brown line) and cross-peak (green line) intensities in the presence of chemical exchange as a function of mixing time

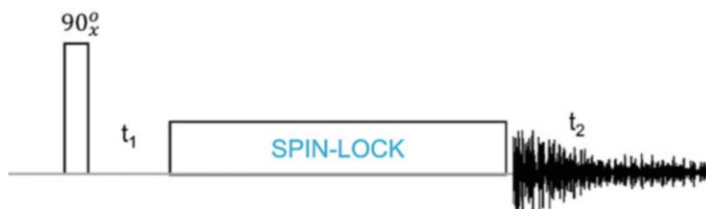
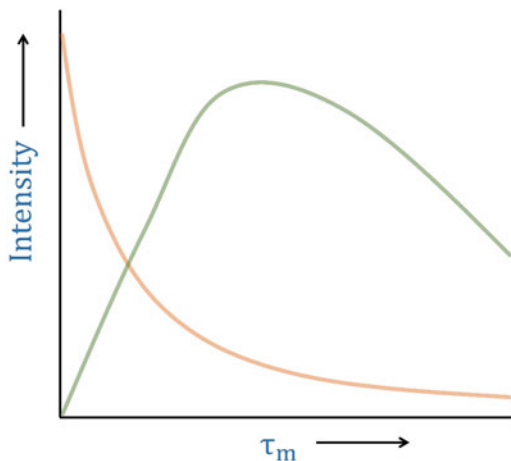


Fig. 6.30 Pulse sequence for two-dimensional ROESY experiment

In both these equations, the first term produces the diagonal peak in the end, and the second term produces the cross-peak. In the initial rate limit, i.e., $\frac{\tau_m}{T_2} \ll 1$, the diagonal peaks are positive, and the cross-peaks will be negative.

Table 6.4 shows the results of detailed calculations of the intensities as a function of spectrometer frequency (ω_0), correlation times (τ_c) of molecular tumbling, and chemical exchange rates (k) for ROESY and NOESY spectra. It is seen that the ROESY spectrum allows the discrimination of ROE and chemical exchange peaks, whereas NOESY will have ambiguities.

The ROESY experiment has some additional advantages in comparison to the NOESY, especially for molecules with $\omega_0\tau_c \sim 1$. In such situations, the NOESY spectrum does not show magnetization transfer.

6.6.2.6 Application of Two-Dimensional Homonuclear Experiments in Structural Analysis of Small Organic Molecules: A Case Study of Artemisinin

The combined utilization of two-dimensional homonuclear NMR spectra, viz., DQF-COSY, TOCSY, and NOESY, helps in solving structures of molecules. Figure 6.31 represents the homonuclear two-dimensional NMR spectra recorded on artemisinin molecule (Fig. 6.31d). The chemical shift correlations obtained from

Table 6.4 Comparison of cross-peak and diagonal peak signs in NOESY and ROESY spectra for different molecular tumbling rates and chemical exchange

Condition	NOESY		ROESY	
	Diagonal peak	Cross-peak	Diagonal peak	Cross-peak
$\omega_0\tau_c \ll 1$	+	–	+	–
$\omega_0\tau_c \sim 1$	+	0	+	–
$\omega_0\tau_c \gg 1$	+	+	+	–
Chemical exchange (k)	+	+	+	+

the DQF-COSY (Fig. 6.31a) are useful for identifying the scalarly coupled spin pairs of artemisinin; for example, correlations with the spin 9 allow to get the chemical shift assignments of 8 and for one of the methyl groups. In contrast, the correlations from spin 9 in the TOCSY (Fig. 6.31b) spectrum facilitate monitoring the relayed spin network up to 4–5 bonds. In the present case, from spin 9 to spin 7, TOCSY correlations are observed. Besides, spatial information obtained from the NOESY spectrum (Fig. 6.31c) enables to obtain the three-dimensional structure of artemisinin molecule. The observed NOE correlations between the spin pairs, 12-5'', 12-6, 12-8', and 8a-5a, confirm the given structure for artemisinin molecule (Fig. 6.31d).

6.6.3 Two-Dimensional Heteronuclear Correlation Experiments

Coherence transfer can also be effected between two different types of nuclear species, say I and S . Such experiments are referred to as heteronuclear correlation experiments. A variety of heteronuclear experiments can be designed, since the RF pulses can be applied selectively to either of the species and heteronuclear broadband decoupling can be incorporated without any constraints. Heteronuclear experiments have particular advantages:

- (i) Increased sensitivity of indirect detection as evidenced in the INEPT pulse sequence.
- (ii) The possibility of unraveling overlapping I resonances by exploiting the chemical shifts of the S spins and vice versa.
- (iii) The correlation of chemical shifts of different nuclear species would facilitate assignments in complex systems.

In most cases, one of the two nuclear species is a rare nucleus (S) such as ^{13}C , ^{15}N , etc., while the other nucleus is usually a more sensitive species (I) such as ^1H , ^{19}F , etc.

6.6.3.1 Heteronuclear COSY

The simplest I-S correlation experiment (considering $I = ^1\text{H}$ and $S = ^{13}\text{C}$) is depicted in Fig. 6.32. This pulse sequence is very similar to the homonuclear COSY, except

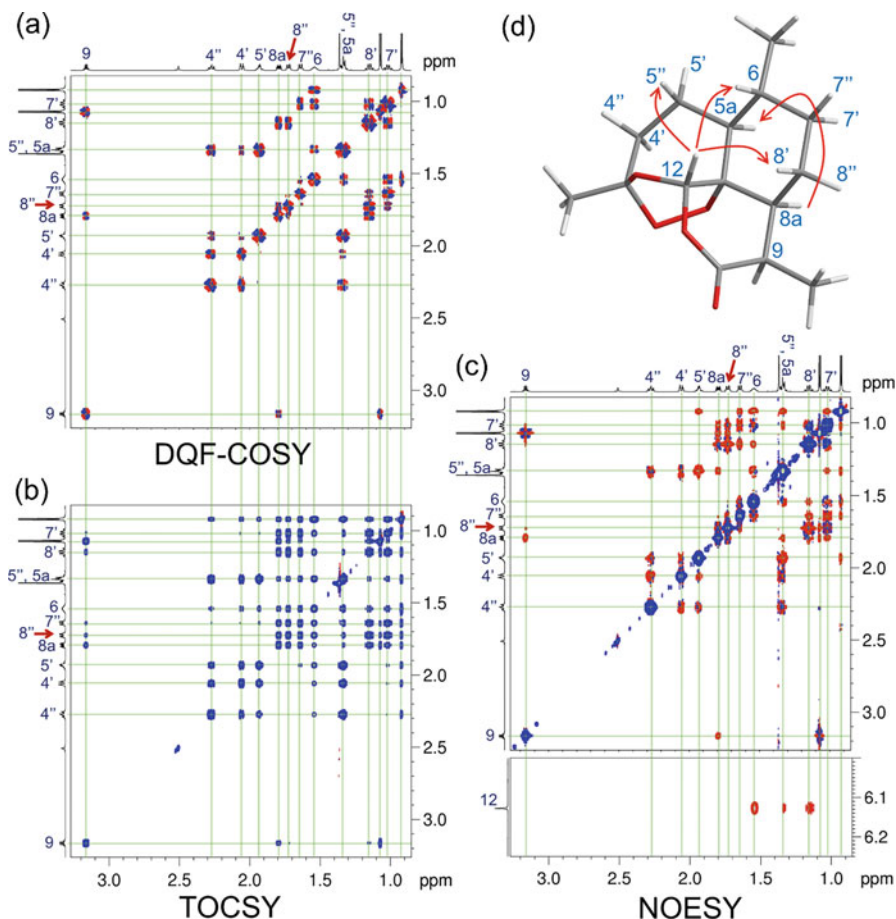


Fig. 6.31 Two-dimensional homonuclear correlation spectra DQF-COSY (a), TOCSY (b), and NOESY (c) recorded on artemisinin molecule dissolved in DMSO- D_6 solvent. The combined utilization of all these spectra resulted in the given structure for artemisinin molecule (d). The green-colored lines are useful to track the chemical shift correlations, whereas the red-colored arrows are the NOE correlations

the first 90° pulse is selective to only I spin. During the t_1 period, therefore, there are only I spin coherences. The pair of pulses on I and S , at the end of t_1 transfers coherence partially to the S spin. The magnetization is finally detected on the S spin. Thus, the two-dimensional spectrum will have only I - S correlation peaks, which retain the fine structure as in the COSY spectrum. Such a spectrum for two spins is schematically shown in Fig. 6.33. It has the antiphase property along both dimensions, and the separation between the components is equal to the coupling constant.

Fig. 6.32 Pulse sequence for ^1H - ^{13}C correlation experiment with carbon detection. H_z is the starting ^1H magnetization, and $2C_yH_z$ represents the ^{13}C magnetization component at the beginning of detection

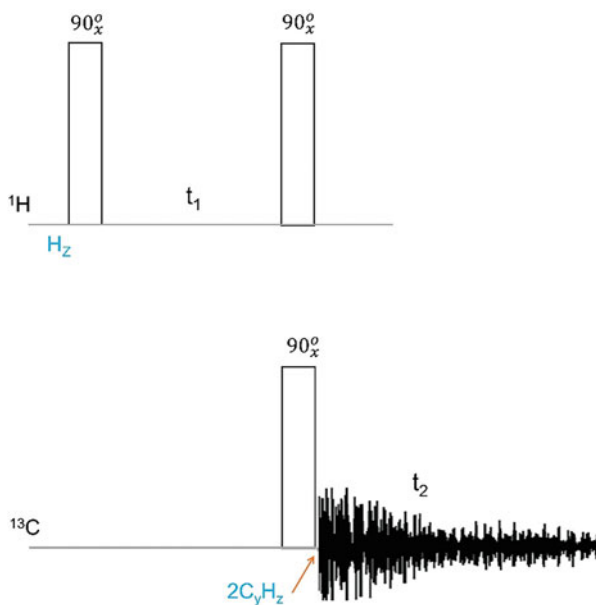
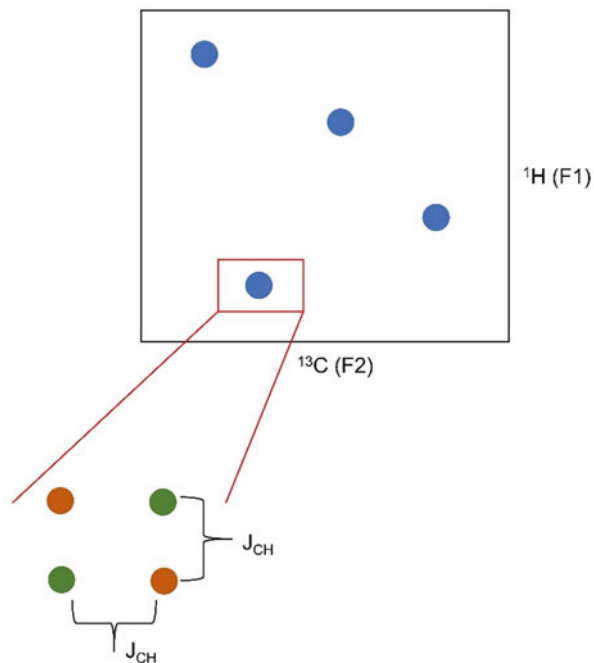


Fig. 6.33 Schematic spectrum from the pulse sequence in Fig. 6.31. Orange and green symbols indicate positive and negative signs, respectively



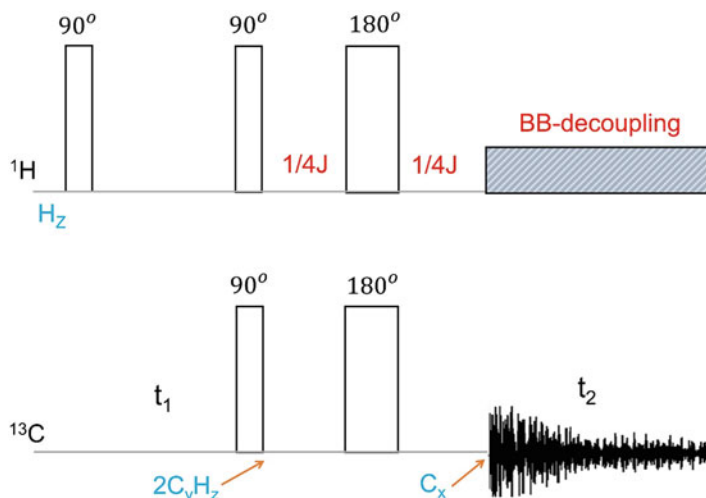


Fig. 6.34 Pulse sequence for ^1H - ^{13}C correlation with carbon detection and proton decoupling during acquisition. Magnetization components at few time points along the sequence are indicated in cyan. BB implies broadband and J is the one-bond ^1H - ^{13}C coupling constant

In most of these experiments, the correlation is established between nuclei, which are directly bonded. These one-bond coupling constants are usually very high, for example, $J^{1\text{H}}-^{13}\text{C} \sim 120\text{--}160$ Hz and $J^{1\text{H}}-^{15}\text{N} \sim 90\text{--}100$ Hz. While this enables a very efficient transfer of coherence, the large overall width of the cross-peak hampers the resolution in the spectra. Since the one-bond coupling constant does not add too much value for structural information of the molecules, it would be desirable to remove this coupling constant information from the spectrum. This is partially achieved by the pulse sequence shown in Fig. 6.34. In the pulse sequence, an additional spin echo block is added to refocus the S spin antiphase magnetization so that during detection of S magnetization, the I spins can be decoupled. This results in the collapse of the fine structure along the detection axis (F_2), which is shown in Fig. 6.34. The components here will have twice the intensity as compared to Fig. 6.32.

A further improvement can be achieved by eliminating the coupling information altogether. This can be achieved in more than one ways (Fig. 6.35).

(A) The HETCOR Pulse Sequence

The pulse sequence for the HETCOR experiment (considering $I = ^1\text{H}$ and $S = ^{13}\text{C}$) is shown in Fig. 6.36. It begins with the excitation of the I spin magnetization by a nonselective 90° pulse. Then this magnetization evolves during the t_1 period during which the I - S coupling is removed by the application of 180° pulse to the S spin in the middle of the t_1 period. Thus, during t_1 , the I spins are labelled by their characteristic frequencies. Following the t_1 period, a spin echo block [$\tau_1 -$

Fig. 6.35 Schematic ^1H - ^{13}C correlation spectrum from the pulse sequence given in Fig. 6.34. Orange and green symbols indicate positive and negative signs, respectively

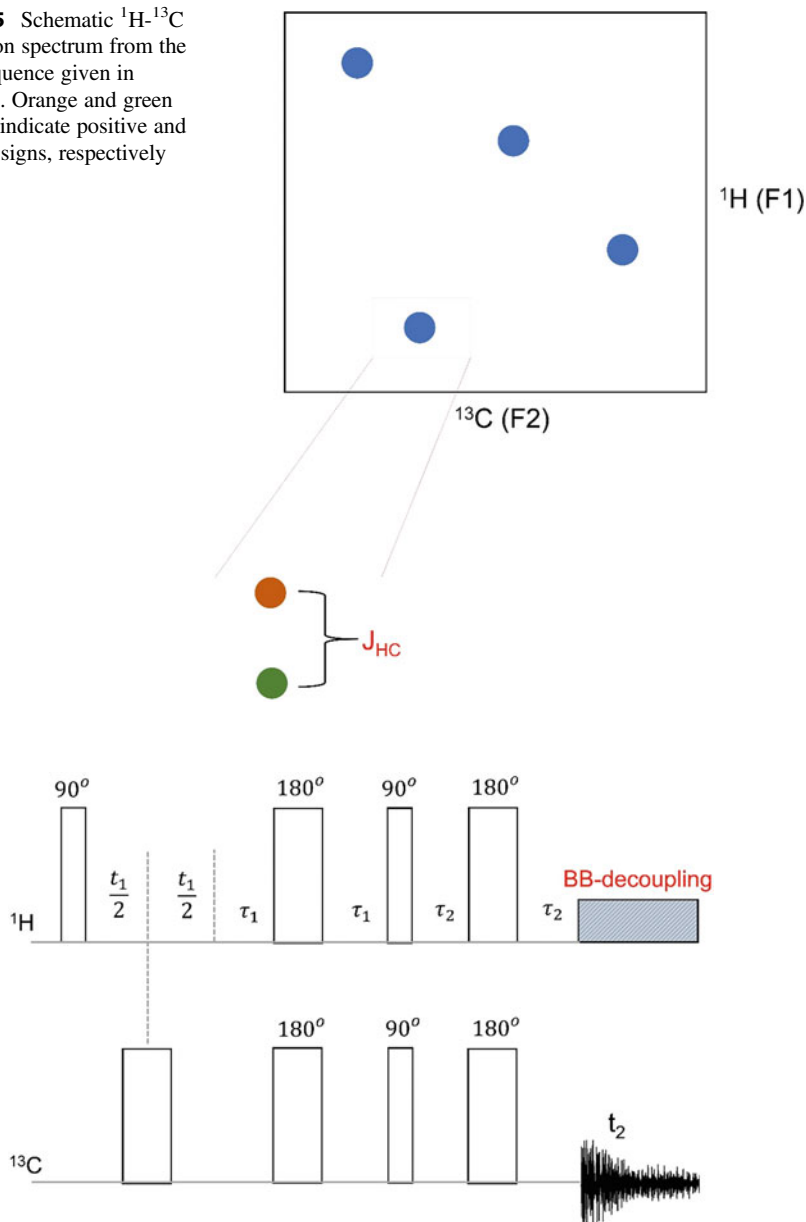
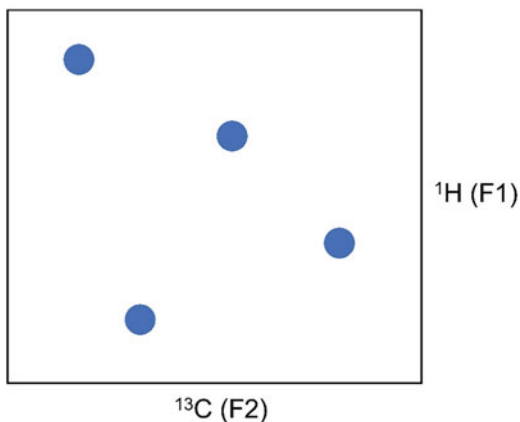


Fig. 6.36 Pulse sequence for the HETCOR experiment, which incorporates ^1H - ^{13}C decoupling along both $F1$ and $F2$ axes

$180^\circ (I, S) - \tau_1]$ is introduced during which I spin magnetization evolves under the I - S coupling and generates antiphase I spin magnetization. The pair of $90^\circ (I, S)$ pulses at the end of the spin echo causes coherence transfer to the S spin, resulting in

Fig. 6.37 Schematic HETCOR spectrum. The peaks do not have any fine structure



antiphase S spin magnetization. The delay τ_1 ($\tau_1 = 1/4J_{IS}$) can be adjusted to cause near-complete transfer to the S spin. Then the antiphase S magnetization evolves during the following spin echo period, $[\tau_2 - 180(I, S) - \tau_2]$, to produce in-phase S spin magnetization. This magnetization is detected during t_2 , while I spins are simultaneously decoupled. Thus, the resulting spectrum has only one peak for an I - S pair, as shown in Fig. 6.37. The signal-to-noise ratio (SNR) in this experiment is

$$\text{SNR} \propto \gamma_I (\gamma_S)^3 \quad (6.84)$$

(B) The HSQC Pulse Sequence

This experiment improves upon the HETCOR experiment. The pulse sequence for the HSQC (heteronuclear single-quantum correlation) is depicted in Fig. 6.38. The experiment starts with an INEPT (refer to Sect. 4.7 in Chap. 4) block which achieves the transfer of I spin magnetization to S spin ($I_z \rightarrow 2I_z S_y$). This S spin magnetization is antiphase in character with respect to the coupled I spin and evolves during the following t_1 period under chemical shift Hamiltonian. Evolution under the I - S coupling is eliminated because of the 180° pulse applied to the I spin in the middle of the t_1 period. Thus, during the t_1 period, the S spins are labeled by their characteristic frequencies. The subsequent pair of 90° pulses on I and S transfers the magnetization back to the I spin as antiphase magnetization ($2I_z S_y \rightarrow 2I_y S_z$). This antiphase I magnetization is then refocused during the next spin echo block, $[\tau_2 - 180(I, S) - \tau_2]$, to generate in-phase I magnetization (I_x). This in-phase magnetization then evolves during t_2 with characteristic I spin frequencies, while the I - S coupling is removed by broadband S spin decoupling. Thus, the resultant spectrum has a single peak for an I - S pair, as shown Fig. 6.39.

The differences between the experiments A (HETCOR) and B (HSQC) are the following.

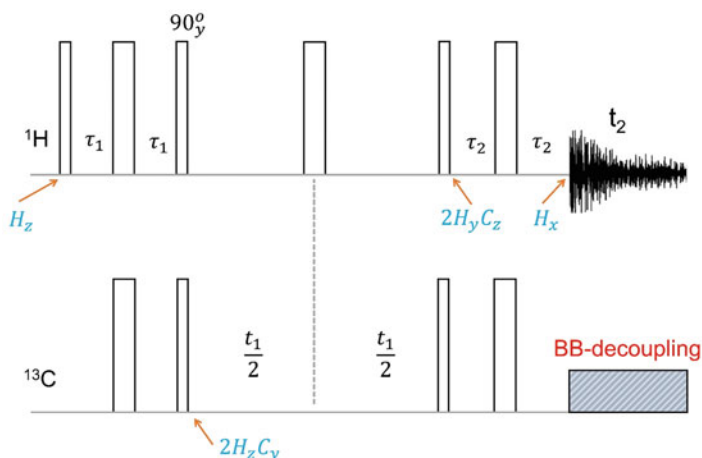
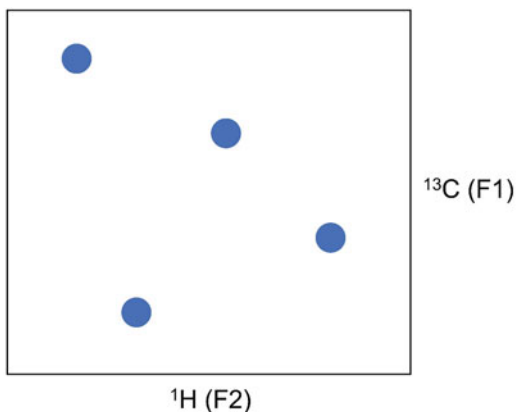


Fig. 6.38 Pulse sequence for the HSQC experiment. Narrow and wide rectangles indicate 90° and 180° pulses, respectively. Unless mentioned all the pulses are applied along the x-axis. Relevant magnetization components at certain time points are indicated in cyan

Fig. 6.39 Schematic appearance of the HSQC spectrum. The peaks do not have any fine structure



- (i) In A, S spin magnetization is detected, whereas in B, I spin magnetization is detected. This has an impact on sensitivity, since the latter is proportional to $\gamma^{3/2}$ of the detected nucleus. Therefore, if I spin is ^1H and S spin is ^{13}C , then the HSQC experiment has a sensitivity gain of $\left(\frac{\gamma_{\text{H}}}{\gamma_{\text{C}}}\right)^{3/2}$. This is a factor of 8, which is a substantial gain in terms of the signal-to-noise ratio, which in turn amounts a gain by factor of 64 in terms of the experimental time. Similarly, for $S = ^{15}\text{N}$ and $I = ^1\text{H}$, the gain will be a factor of ~ 1000 , in terms of experimental time.
- (ii) In A, the detected signal will have S frequencies, whereas in B, the detected signal will have I frequencies. The spectral range of S spin (^{13}C , ~ 140 ppm) is much larger compared to that of the I spin (^1H , ~ 10 ppm). Therefore, the

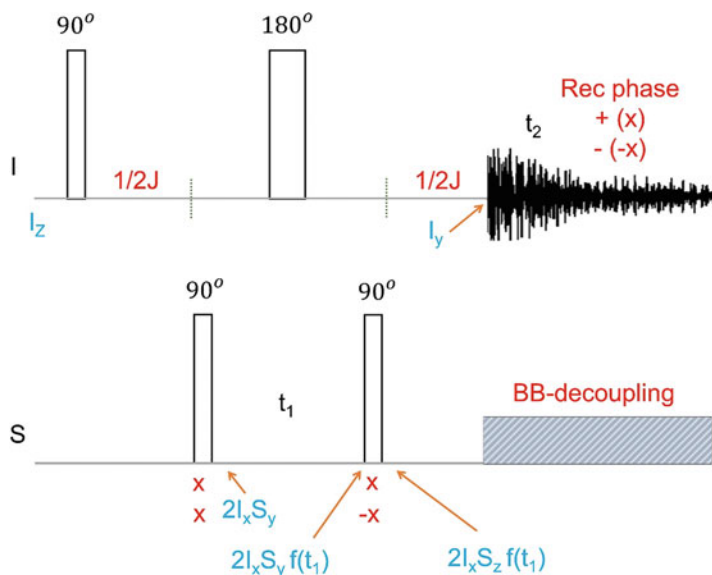


Fig. 6.40 Pulse sequence for the HMQC experiment. Relevant magnetization components at certain time points are indicated in cyan. The I spin pulses are applied along x -axis. The pulses on the S spin and the receiver are phase cycled as indicated

chemical shift dispersion along the detection axis will be higher in A as compared to that in B, even considering that the γ_H is four times γ_C .

(C) The HMQC Pulse Sequence

This experiment achieves coherence transfer from spin I to spin S via multiple quantum coherences; hence, this is termed as heteronuclear multiple-quantum coherence (HMQC) transfer experiment. The pulse sequence for HMQC is shown in Fig. 6.40.

In Fig. 6.40, the spin I is taken to represent the abundant species, and the spin S is taken to represent the rare heteronucleus (^{13}C (1.1% abundant)/ ^{15}N (0.37% abundant)). In the case of protons which are coupled ^{12}C or ^{14}N , the signals coming from these have to be eliminated. This is achieved by phase cycling the receiver (+ x , $-x$) in consecutive scans, while the phase of the first 90° pulse on I spin remains as + x .

The experiment can be analyzed using the product operator formalism, and the flow of the magnetization can be described for a I - S two-spin system. The first 90° pulse along the x -axis creates transverse magnetization of the I spin:

$$I_z \rightarrow -I_y \quad (6.85)$$

The chemical shift evolution of the I magnetization is refocused by the 180° pulse kept at the middle of the entire evolution period before the start of the detection. Hence, this evolution need not be calculated. When the τ period is set equal to $1/2J_{IS}$,

the I spin magnetization gets transferred entirely to multiple-quantum IS coherence (double-quantum + zero-quantum) after the application of 90° x-pulse on the S spin.

$$-I_y \rightarrow -2I_x S_y \quad (6.86)$$

As described earlier, this multiple quantum coherence does not evolve under the influence of J-coupling between I and S . Since the I spin chemical shift is refocused by the 180° pulse in the middle of the t_1 period, we need to calculate the chemical shift evolution of the S spin only. Thus,

$$-2I_x S_y \rightarrow -2I_x [S_y \cos(\omega_s t_1) - S_x \sin(\omega_s t_1)] \quad (6.87)$$

The last 90° x-pulse on the S spin converts a part of this magnetization into a single-quantum coherence.

$$-2I_x [S_y \cos(\omega_s t_1) - S_x \sin(\omega_s t_1)] \rightarrow -2I_x S_z \cos(\omega_s t_1) + 2I_x S_x \sin(\omega_s t_1) \quad (6.88)$$

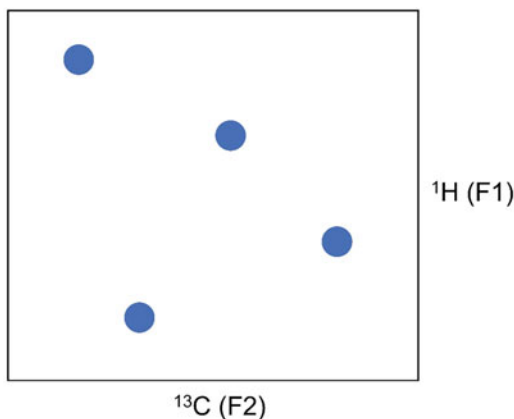
The first term in Eq. 6.88 on the right-hand side is the single-quantum I spin magnetization antiphase with respect to S , and the second term represents multiple quantum coherence which does not lead to observable signal. During the following τ period, the antiphase I magnetization gets refocused into in-phase magnetization.

$$-2I_x S_z \cos(\omega_s t_1) \rightarrow -I_y \cos(\omega_s t_1) \quad (6.89)$$

During the detection period t_2 , the I spin is decoupled from S spin and thus will only have chemical shift evolution. Thus, we will only have one cross-peak between I and S , as shown in Fig. 6.41. From explicit product operator calculations, the intensity of the cross-peaks in the final spectrum turns out to be proportional to $[\sin(\pi J_{IS}\tau)]^2$.

In the examples shown, we have considered one I spin and one S spin. However, in real systems, there will be situations where an S spin is J-coupled to more than one I spin species, which may be scalarly coupled among themselves. Assuming I and

Fig. 6.41 Schematic HMQC spectrum for I - S spin systems



K are two such spins of the same nuclear species, a similar calculation will lead to the following observable operator at the start of the detection period.

$$\rho'(t_1) = -I_y \cos(\omega_S t_1) \cos(\pi J_{IK} t_1) + 2I_x K_z \cos(\omega_S t_1) \sin(\pi J_{IK} t_1) \quad (6.90)$$

This indicates the following:

- (i) There will be splitting along the indirect dimension ($F1$) due to J_{IK} .
- (ii) The sum of cosine-cosine and cosine-sine products in Eq. 6.90 results in the superposition of in-phase absorptive and antiphase dispersive line shapes along the $F1$ axis; this results in mixed phases.

After considering the evolution of I spin magnetization terms in Eq. 6.90 during the following t_2 period, the observable part of the density operator will be

$$\rho''(t_2) = f'(t_1) \{ I_y \cos(\omega_I t_2) \cos(\pi J_{IK} t_2) - I_x \sin(\omega_I t_2) \cos(\pi J_{IK} t_2) \} \\ + f''(t_1) \{ I_y \cos(\omega_I t_2) \sin(\pi J_{IK} t_2) - I_x \sin(\omega_I t_2) \sin(\pi J_{IK} t_2) \} \quad (6.91)$$

where

$$f'(t_1) = \cos(\omega_S t_1) \cos(\pi J_{IK} t_1) \text{ and } f''(t_1) = \cos(\omega_S t_1) \sin(\pi J_{IK} t_1)$$

If we assume the detection of y-magnetization, the resultant signal will be

$$\text{Signal} = \cos(\omega_I t_2) [\cos(\pi J_{IK} t_2) f'(t_1) + \sin(\pi J_{IK} t_2) f''(t_1)] \\ = \{ [\cos(\omega_I + \pi J_{IK}) t_2 + \cos(\omega_I - \pi J_{IK}) t_2] f'(t_1) + [\sin(\omega_I + J_{IK}) t_2 - \sin(\omega_I - \pi J_{IK}) t_2] f''(t_1) \} \quad (6.92)$$

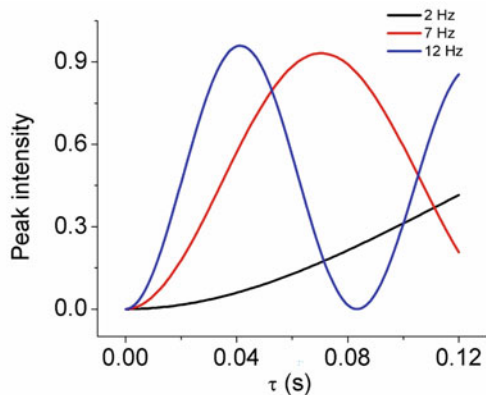
From this it follows that there will be splitting along the direct dimension ($F2$) due to J_{IK} . Further, there will be superposition of in-phase absorptive and antiphase dispersive line shapes along the detection axis ($F2$), which results in mixed phases.

The dispersive component of the signal can be purged by inserting a 90° y-pulse on I spin prior to the detection period. The antiphase I spin operator is converted into antiphase k spin operator ($2I_x K_z \rightarrow 2I_z K_x$). This results in a cross-peak between K and S spins. If the k spin is not coupled to S spin, this can lead to a confusion with regard to the correlations, though it will have antiphase components as against in-phase components in the I - S cross-peak. These complications do not occur in the HSQC spectra.

6.6.3.2 Heteronuclear Multiple Bond Correlation (HMBC)

The heteronuclear correlation experiments, HSQC, HETCOR and HMQC, rely on the transfer of coherences based on one-bond coupling constants. Often it is necessary to establish correlations via multiple bond coupling constants for unambiguous resonance assignments and structure elucidations. If one has to optimize the coherence transfer to reflect these correlations, the delay τ has to be chosen to be $\frac{1}{2J_{IS}^{\text{long}}}$,

Fig. 6.42 Peak intensities in HMQC experiment as a function of the long-range coupling constant while assuming the T_2 relaxation value equal to 1 s



where I and S are spins separated by multiple bonds. These coupling constants are much smaller compared to one-bond couplings, and there is also a large variation in these couplings (1–15 Hz). Simultaneous optimization with respect to all these couplings is not possible. As discussed earlier for HMQC, the intensity of the cross-peaks in the final spectrum turns out to be proportional to $\left[\sin \left(\pi J_{IS}^{\text{long}} \tau \right) \right]^2$. Figure 6.42 shows the variation in the intensities with τ for three different values of long-range couplings (2 Hz, 7 Hz, and, 12 Hz).

From this, it can be seen that the smaller the coupling, the larger is the required delay. In such a situation, relaxation also plays an important role in determining the intensity of the cross-peak. Figure 6.43 shows a pulse sequence designed to circumvent some of these problems. This experiment is referred to as heteronuclear multiple bond correlation (HMBC). It differs from the HMQC pulse sequence in only one sense; i.e., the last refocusing τ period (Fig. 6.40) is eliminated, and accordingly, the decoupling of S spin has also been removed, while this saves on the relaxation loss and the intensity will be proportional to $\left[\sin \left(\pi J_{IS}^{\text{long}} \tau \right) \right]$ (Fig. 6.44), which is better than $\left[\sin \left(\pi J_{IS}^{\text{long}} \tau \right) \right]^2$ dependence. This results in an antiphase splitting of the cross-peak along the detection dimension.

6.6.4 Combination of Mixing Sequences

Depending upon the desired information in the two-dimensional spectrum, it is possible to design pulse sequences, which have a mix of different types of coherence transfer steps discussed in the previous sections. For example, HSQC can be combined with TOCSY or COSY or NOESY transfer, HMQC can be combined with TOCSY or COSY or NOESY, etc. Some typical pulse sequences to achieve these features are shown in Fig. 6.45. The corresponding spectra are shown in Fig. 6.46.

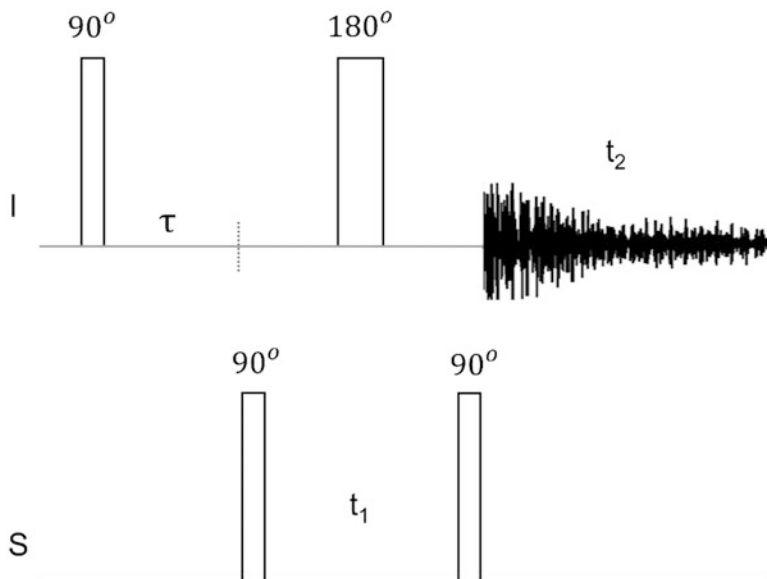
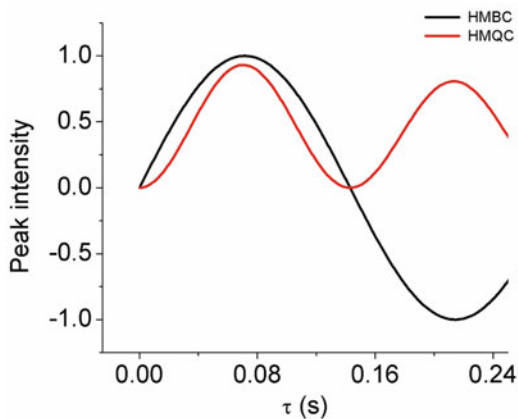


Fig. 6.43 Pulse sequence for the HMBC experiment

Fig. 6.44 A comparison of intensities in HMQC and HMBC spectra for a small J -value (7 Hz) while assuming the T_2 relaxation value equal to 1 s



6.7 Three-Dimensional NMR

The ideas discussed in the context of two-dimensional NMR can be extended to include another dimension resulting in a three-dimensional spectrum. A schematic of such an experiment is indicated in Fig. 6.47.

This consists of a *preparation period*, two *evolution periods* (t_1 and t_2), two *mixing periods* (M1 and M2), and a *direct detection period* (t_3). The resulting time

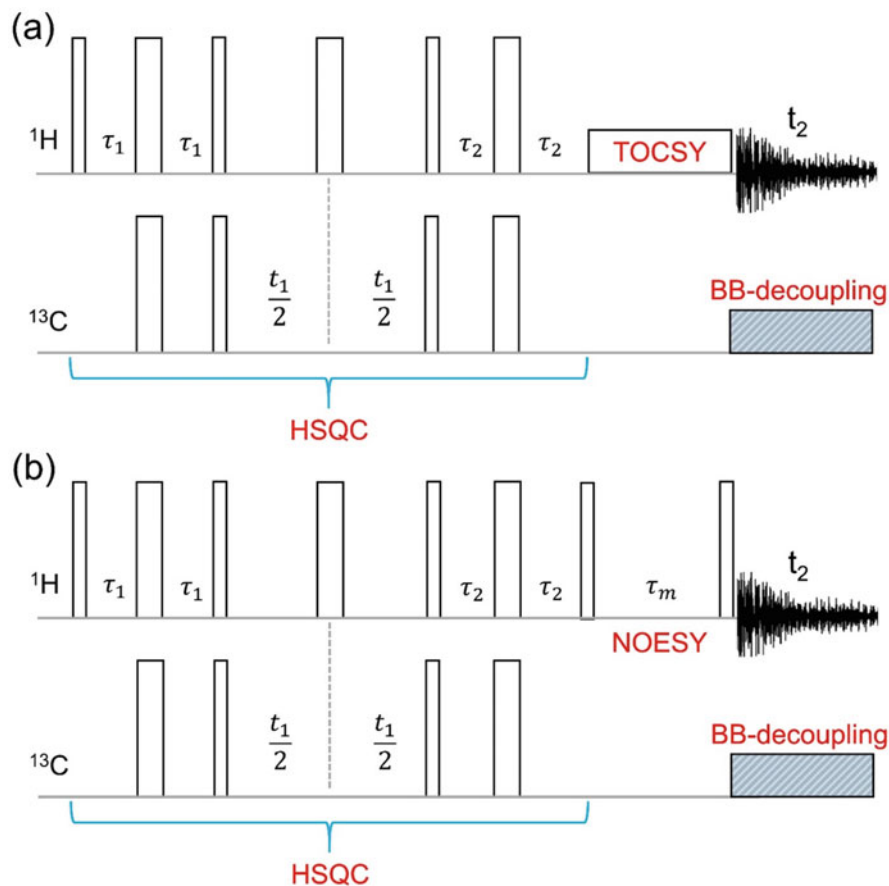


Fig. 6.45 Pulse sequences combining (a) HSQC with TOCSY and (b) HSQC with NOESY

domain data, $S(t_1, t_2, t_3)$, after three-dimensional Fourier transformation produces a three-dimensional frequency domain spectrum, $S(F_1, F_2, F_3)$.

$$S(t_1, t_2, t_3) \xrightarrow{3D-FT} S(F_1, F_2, F_3) \quad (6.93)$$

A variety of three-dimensional spectra can be generated by choosing appropriate mixing sequences, M1 and M2. For example, if M1 is chosen to result in a HSQC type of the transfer of coherence with its independent evolution period t_1 , and M2 is chosen to result in a TOCSY type of transfer with the evolution period t_2 , then in the end, we generate a three-dimensional HSQC-TOCSY spectrum, schematically shown in Fig. 6.48.

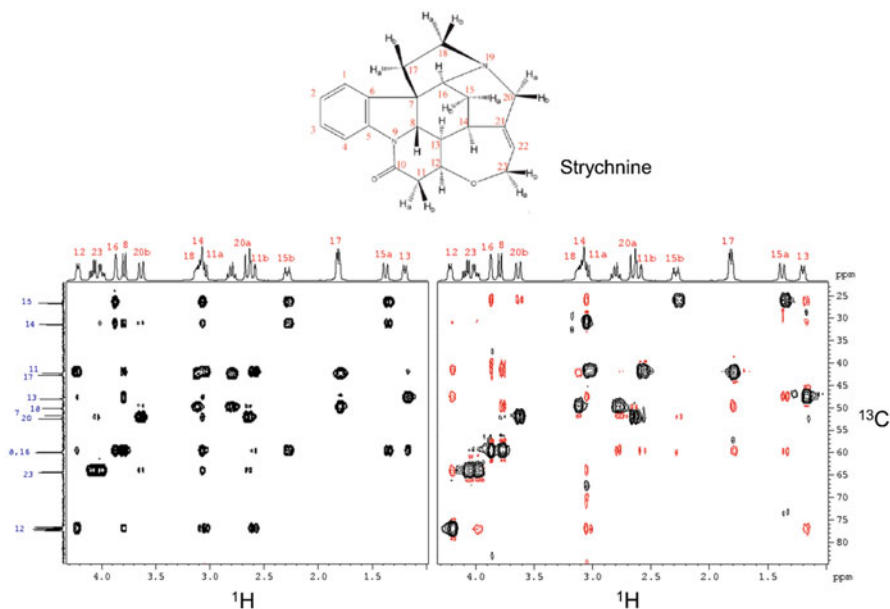


Fig. 6.46 Spectra of (a) HSQC-TOCSY and (b) HSQC-NOESY recorded on strychnine. It is adapted from the Bruker website

Fig. 6.47 A schematic of a three-dimensional experiment



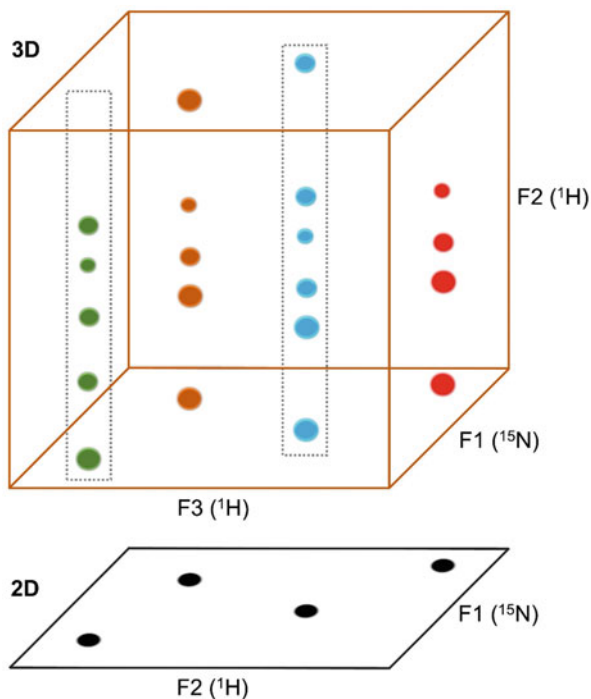
Similar combinations can be made with COSY, TOCSY, NOESY, HSQC, HMQC, HMBC, etc., to generate a variety of three-dimensional spectra.

A large variety of three-dimensional spectra have been designed for biomolecular applications, especially proteins. These differ in magnetization transfer pathways along the protein chain. While these are covered in several elegant monographs, some of these are indicated in Fig. 6.49, wherein the pathways of magnetization transfer through the chain are indicated.

These rely on the transfer of magnetization via evolution under the influence of one- and two-bond couplings along the polypeptide chain. These coupling constants are independent of the amino acid sequence in the chain, and their typical values are shown in Fig. 6.50.

In the following, we describe briefly a few experiments to demonstrate the analysis of these pulse sequences, in general. All these experiments require proteins uniformly enriched in ^{13}C and ^{15}N isotopes. These are routinely achieved by standard techniques in recombinant protein production. These experiments also require spectrometers equipped with three independent channels, ^1H , ^{13}C , and ^{15}N .

Fig. 6.48 Schematic of three-dimensional HSQC-TOCSY spectrum. The TOCSY relay is seen along the F2 axis in the three-dimensional spectrum



6.7.1 The CT-HNCA Experiment

Figure 6.51 shows the pulse sequence for the constant time (CT)-HNCA experiment.

The flow of magnetization through the pulse sequence is schematically shown in Eq. 6.94:

$$H_i^N \rightarrow N_i(t_1) \rightarrow C^\alpha(i, i-1)(t_2) \rightarrow N_i \rightarrow H_i^N(t_3) \quad (6.94)$$

It starts with the ^1H magnetization, H_z , and the evolution of this magnetization through the pulse sequence can be calculated using the product operator formalism. At time point “a,” after the first INEPT transfer from amide proton (H_i^N) to N_i along the backbone, the density operator is given by

$$\rho_a = -2H_{iz}^N N_{iy} \quad (6.95)$$

H_{iz}^N refers to z-magnetization of the amide proton (H_i^N) of the i^{th} residue along the polypeptide chain, and N_{iy} refers to the y-component of the backbone ^{15}N spin of the i^{th} residue. Thus, this operator represents antiphase ^{15}N magnetization with respect to the amide proton (H_i^N).

Following this, the ^{15}N magnetization evolves for a constant time period T under different Hamiltonians:

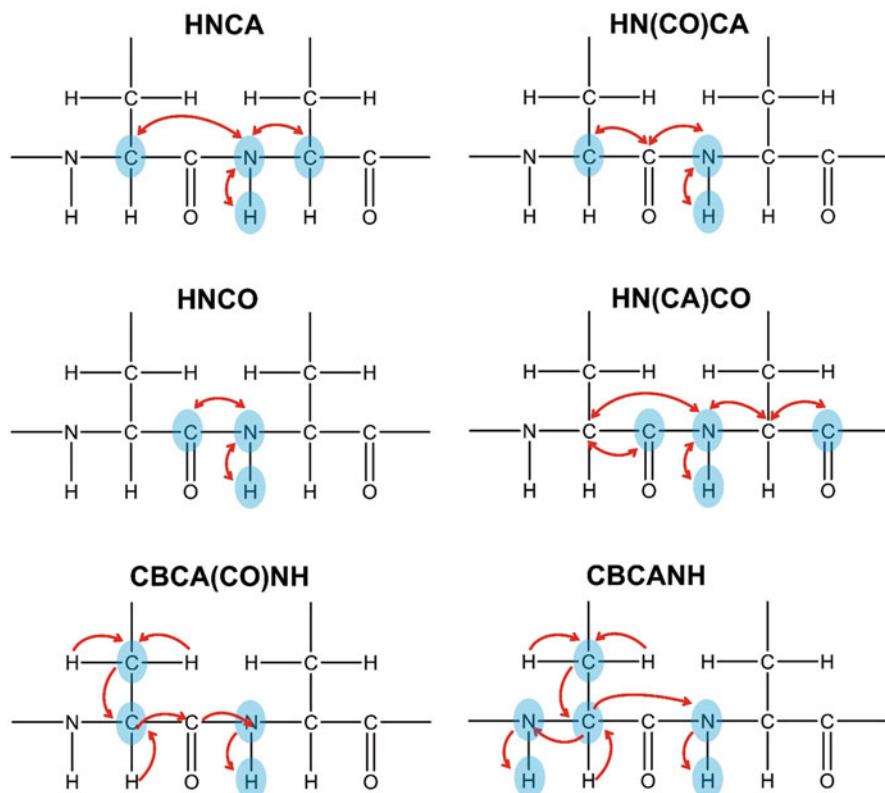
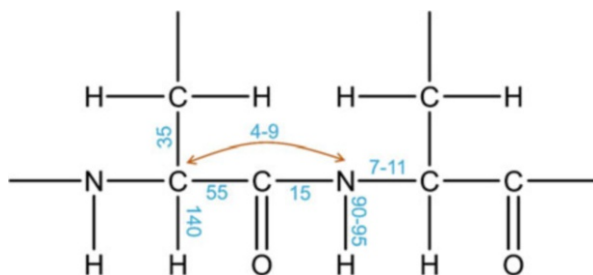


Fig. 6.49 Schematic of magnetization transfer pathways in HNCA, HN(CO)CA, HNC(O), HN(CA)CO, CBCA(CO)NH, and CBCANH experiments. Red arrows identify magnetization transfers during the pulse sequence, and the atoms enclosed in cyan circles are the nuclei participating in the transfer process

Fig. 6.50 One- and two-bond coupling constants relevant for magnetization transfers shown in Fig. 6.48



(i) Under the influence of ^{15}N chemical shifts for a period t_1 .

$$-2H_{iz}^N N_{iy} \rightarrow -2H_{iz}^N (N_{iy} \cos(\omega_{Ni} t_1) - N_{ix} \sin(\omega_{Ni} t_1)) \quad (6.96)$$

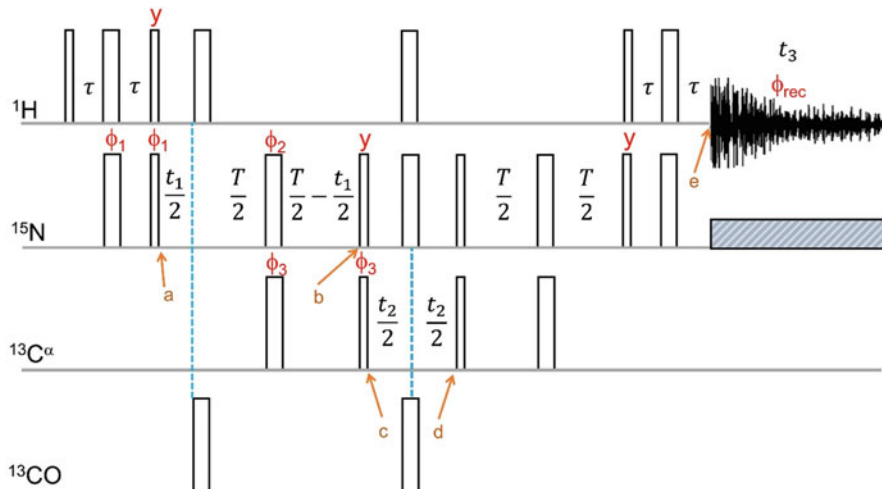


Fig. 6.51 Pulse sequence for the constant time (CT)-HNCA experiment. Narrow and wide rectangular bars represent 90° and 180° pulses, respectively. Pulses are applied along the x-axis unless indicated otherwise. The phase cycles ϕ_1 – ϕ_3 are as follows: $\phi_1 = x$ and $-x$; $\phi_2 = 4(x), 4(y), 4(-x)$, and $4(-y)$; and $\phi_3 = 2(x)$ and $2(-x)$. $\phi_{\text{rec}} = x, -x, -x, x, -x, x, x$, and $-x$. The period $\tau = 1/4J_{\text{NH}}$. T represents the constant time period, which is typically 22–25 ms. Broadband decoupling of ^{15}N is achieved using standard composite decoupling. Alphabets a–e identify time points discussed in the text

- (ii) Evolution under the influence of ^{15}N - ^1H coupling is effectively refocused and ^{15}N magnetization remains anti-phase with respect to ^1H .
- (iii) Under the influence of one-bond ($N_i - C_i^\alpha$) and two-bond ($N_i - C_{(i-1)}^\alpha$) couplings for the period T .
- (iv) Evolution under ^{15}N - ^{13}CO coupling is removed by the application of 180° band-selective pulse to the ^{13}CO spins and also to ^{15}N .
During the period $\frac{t_1}{2} - \pi(CO) - \frac{t_1}{2}$, decoupling happens due to the 180° pulse on the carbonyl spins.

During the next period, $[(\frac{T}{2} - \frac{t_1}{2}) - \pi(^{15}\text{N}) - (\frac{T}{2} - \frac{t_1}{2})]$, decoupling happens due to the 180° pulse on ^{15}N .

Thus, at time point “b,” the density operator is given by

$$\rho_b = \left\{ 4H_{iz}^N N_{ix} C_{iz}^\alpha \Gamma_1(T) + 4H_{iz}^N N_{ix} C_{(i-1)z}^\alpha \Gamma_2(T) \right\} \cos(\omega_{N_i} t_1) \quad (6.97)$$

where

$$\Gamma_1(T) = \sin(\pi^1 J_{C^N T}) \cos(\pi^2 J_{C^N T}) \quad (6.98)$$

$$\Gamma_2(T) = \cos(\pi^1 J_{C^{\alpha}N} T) \sin(\pi^2 J_{C^{\alpha}N} T) \quad (6.99)$$

$\Gamma_1(T)$ and $\Gamma_2(T)$ represent transfer efficiencies, which are seen to be dependent on the constant time period T and the magnitudes of the coupling constants. In this calculation relaxation has been ignored. However, relaxation will be occurring which causes an exponential decay ($\exp(-R_N T)$, where R_N is the transverse relaxation rate of ^{15}N magnetization). Therefore, the constant time period T has to be properly optimized for the efficient transfer of magnetization without losing too much signal.

The first term in Eq. 6.97 represents ^{15}N magnetization of the i^{th} residue, antiphase with respect to H^N and C^{α} of the i^{th} residue. The second term represents ^{15}N magnetization of the i^{th} residue antiphase with respect to H^N of the i^{th} residue and C^{α} of the $(i-1)^{\text{th}}$ residue. Thus, a sequential correlation between i and $(i-1)$ residues is created. Following the application of a pair of 90° pulses to ^{15}N and C^{α} spins at the end of the T period results in the density operator at time point “c”:

$$\rho_c = \left\{ 4H_{iz}^N N_{iz} C_{iy}^{\alpha} \Gamma_1(T) + 4H_{iz}^N N_{iz} C_{(i-1)y}^{\alpha} \Gamma_2(T) \right\} \cos(\omega_{N_i} t_1) \quad (6.100)$$

Now the magnetization is on C^{α} of “i” (first term in 6.100) and $(i-1)$ (second term in 6.100) residues. This magnetization evolves for the t_2 period under the influence of C^{α} chemical shifts. All the coupling evolutions (except $C^{\alpha} - C^{\beta}$ coupling) are eliminated by simultaneous 180° pulses on CO, ^{15}N , and ^1H channels. At the end of the t_2 evolution (i.e., at time point “d”), the relevant density operator is given by

$$\rho_d = \left\{ 4H_{iz}^N N_{iz} C_{iy}^{\alpha} \cos(\omega_{C_i^{\alpha}} t_2) \Gamma_1(T) + 4H_{iz}^N N_{iz} C_{(i-1)y}^{\alpha} \cos(\omega_{C_{i-1}^{\alpha}} t_2) \Gamma_2(T) \right\} \cos(\omega_{N_i} t_1) \cdot \cos(\pi J_{C^{\alpha}C^{\beta}} t_2) \quad (6.101)$$

This magnetization is then transferred back to the coupled ^{15}N spins by the simultaneous application of 90° pulses on C^{α} and ^{15}N . The ^{15}N magnetization which is antiphase with C^{α} and also ^1H then evolves for the constant time period T to refocus the antiphase character with respect to ^{15}N . At the end of the T period, we have ^{15}N magnetization which is antiphase with respect to coupled H^N spins. A pair of 90° pulse on ^{15}N and ^1H 's at this point transfers the magnetization to amide protons. This proton magnetization is antiphase with respect to the ^{15}N , and during the next INEPT block gets refocused to produce in-phase amide proton magnetization. The relevant density operator at this point “e” is given by

$$\rho_e = H_{ix}^N \left\{ \cos(\omega_{C_i^{\alpha}} t_2) \Gamma_1(T) + \cos(\omega_{C_{i-1}^{\alpha}} t_2) \Gamma_2(T) \right\} \cos(\omega_{N_i} t_1) \cdot \cos(\pi J_{C^{\alpha}C^{\beta}} t_2) \quad (6.102)$$

This proton magnetization is then detected during the time t_3 , while ^{15}N is decoupled in a broadband fashion. Thus, the resulting three-dimensional spectrum can be represented by

$$S(t_1, t_2, t_3) \xrightarrow{3D-FT} S[F1(^{15}\text{N}), F2(C^\alpha), F3(H^N)] \quad (6.103)$$

This is schematically shown in Fig. 6.52a. The $F2$ – $F3$ cross-section plane at particular $^{15}\text{N}_i$ along $F1$ through this three-dimensional spectrum is shown in Fig. 6.52b. It is clearly seen that this experiment allows establishing correlations between two neighboring amino acid residues, which allows sequential walk along the polypeptide chain as indicated in Fig. 6.53. Each strip shows correlations between the amide protons of a particular residue, say i , to the ^{15}N of the same residue i (self-peak) and to the ^{15}N of the previous residue $i-1$ (sequential peak). Typically, the self-peak has slightly higher intensity than the sequential peak.

In practical terms one has to scan through the ^{15}N planes along the $F1$ axis to find H^N – C^α correlation peaks at the appropriate chemical shifts to establish such connectivities. While this works elegantly when the chemical shift dispersions are very good, difficulties arise when there are degeneracies in the chemical shifts. This happens particularly for C^α chemical shifts in disordered and flexible regions of proteins, and sequential connectivities become ambiguous. Several other three-dimensional experiments have been designed to circumvent such problems, and these have been described in great details in many other books (see, e.g., Cavanagh et al., protein NMR spectroscopy). We describe one particular development which has not been covered in any book. Even here, we restrict to the very basic technique (Sanjay et al. 2001); several additions, improvements, and enhancements have been published in the literature.

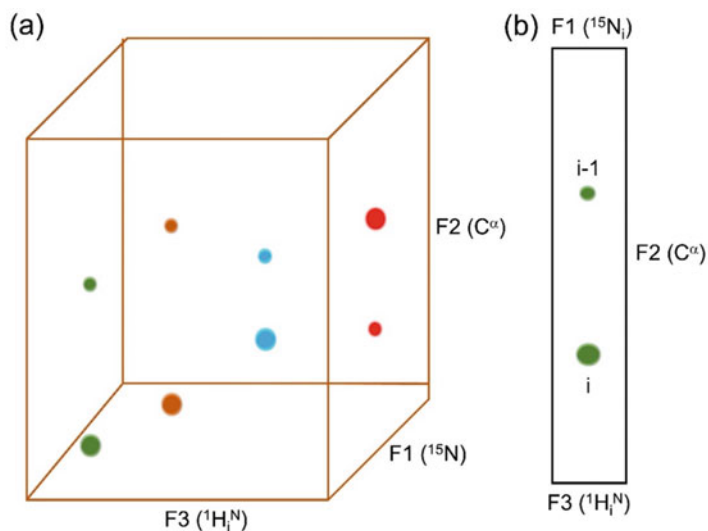


Fig. 6.52 (a) Schematic spectrum of three-dimensional CT-HNCA. (b) The $F2$ – $F3$ cross-section at a particular ^{15}N chemical shift along $F1$. Different colors are used to distinguish between the residues, and larger and smaller circles indicate self- and sequential correlations

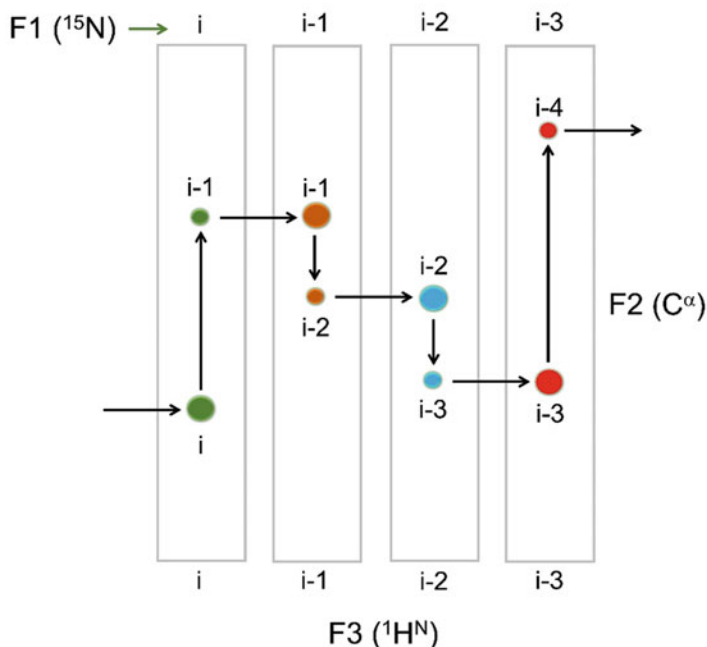


Fig. 6.53 Sequential walk through the polypeptide chain from residues i to $i-4$. Selected $F2$ – $F3$ strips at $F1$ chemical shifts indicated on the top are aligned to show the sequential connectivities through the polypeptide sequence

6.7.2 The HNN Experiment

This experiment is derived by simple modification of the HNCA, and the pulse sequence is shown in Fig. 6.54. It follows the magnetization transfer pathway shown in Fig. 6.55.

The basic differences with respect to the HNCA are: (i) Both the $F1$ and $F2$ axes have ^{15}N chemical shifts, whereas in HNCA $F1$ has ^{15}N and $F2$ has C^α chemical shifts, and (ii) an additional coherence transfer step is included to transfer the magnetization to the neighboring residues ($i \rightarrow i-1$, $i \rightarrow i+1$). The periods $2T_N$ and $2\tau_{CN}$ in Fig. 6.54 are constant time periods during which magnetization transfers take place. In the first $2T_N$ period, the transfer happens from ^{15}N of residue “ i ” to C^α spins of residues “ i ” and “ $i-1$ ”. During the $2\tau_{CN}$ constant time period, magnetization transfer occurs from C^α of “ i ” residue to ^{15}N of i and $i+1$ residues; likewise, the transfer also occurs from C^α of “ $i-1$ ” the residue to ^{15}N of i and “ $i-1$ ” residues. Thus, a sequential correlation gets established between three consecutive residues, $i-1$, i , and $i+1$. The constant time periods, $2T_N$ and $2\tau_{CN}$, are adjusted to be around 22–30 ms. The z-field gradients used in the pulse sequence destroy the unwanted transverse components of the magnetization at different stages. Just before the

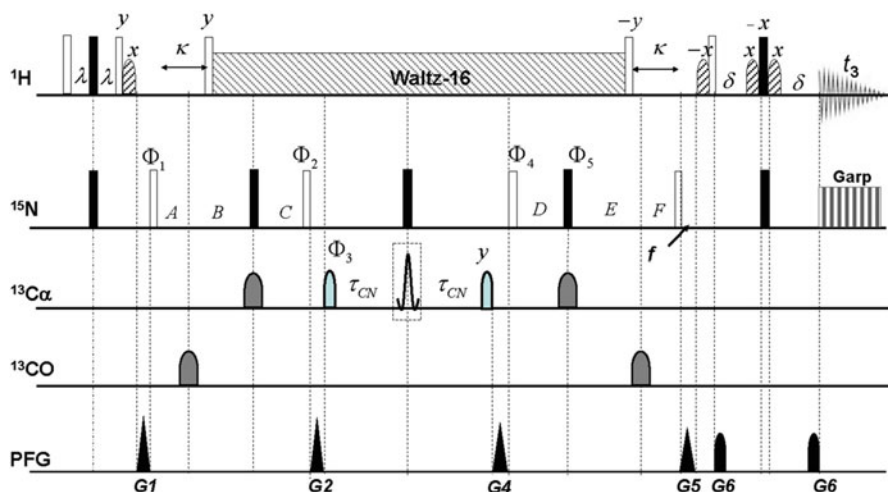


Fig. 6.54 Pulse sequence for the HNN experiment. Narrow (hollow) and wide (filled black) rectangular bars represent nonselective 90° and 180° pulse, respectively. Narrow lobe (light blue) and wide lobe (gray) on carbon channel indicate selective 90° and 180° pulse, respectively. Unless indicated otherwise, the pulses are applied with phase x . Proton decoupling using the Waltz-16 decoupling sequence with field strength of 6.25 kHz is applied during most of the t_1 and t_2 evolution periods, and ^{15}N decoupling using the Garp-1 sequence with field strength 0.9 kHz is applied during acquisition. The ^{13}C carrier frequency for pulses, respectively, on $^{13}\text{C}^\alpha$ and ^{13}CO channels are set at 54.0 ppm and 172.5 ppm. The strengths of the $^{13}\text{C}^\alpha$ pulses (standard Gaussian cascade Q3 (180°) and Q5 (90°) pulses) are adjusted so that they cause minimal excitation of carbonyl carbons. The 180° ^{13}CO -shaped pulse (width 200 μs) had a standard Gaussian cascade Q3 pulse profile with minimal excitation of $^{13}\text{C}^\alpha$. The delays are set to $\lambda = 2.7$ ms, $\kappa = 5.4$ ms, $\delta = 2.7$ ms. The delay τ_{CN} used for the evolution of one-bond and two-bond $^{13}\text{C}^\alpha - ^{15}\text{N}$ coupling is around 12–16 ms and must be optimized. The values for the individual periods containing t_1 are $A = t_1/2$, $B = T_N$, and $C = T_N - t_1/2$. The values for the individual period containing t_2 are $D = T_N - t_1/2$, $E = T_N$, and $F = t_1/2$. The delay $2T_N$ is set to 24–28 ms. Phase cycling for the experiment is $\Phi_1 = 2(x)$, $2(-x)$; $\Phi_2 = \Phi_3 = x$, $-x$; $\Phi_4 = x$; and $\Phi_5 = 4(x)$, $4(-x)$ and receiver = $2(x)$, $4(-x)$, and $2(x)$. Frequency discrimination in t_1 and t_2 is achieved using states-TPPI phase cycling of Φ_1 and Φ_4 , respectively, along with the receiver phase. The gradient (sine-bell shaped; 1 ms) levels are optimized between 30% and 80% of the maximum strength of 53 G/cm in the z -direction. These destroy the unwanted transverse magnetization components

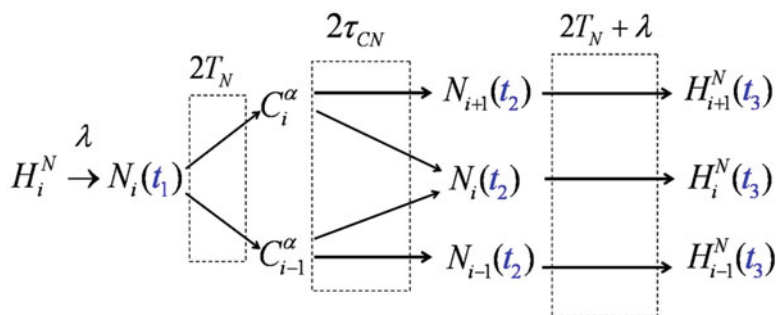


Fig. 6.55 A schematic of magnetization transfer pathway through the HNN pulse sequence

detection, the Watergate pulse block is used to achieve an efficient water suppression.

The experiment can be analyzed in detail using the product operator formalism. Considering a chain of four residues, $i-2$ to $i+1$ along the polypeptide chain, the intensities of the diagonal ($I_i^d; F1 = F2 = N_i, F3 = H_i^N$) and cross-peaks ($(I_{i-1}^c; F1 = N_i, F2 = N_{i-1}, F3 = H_{i-1}^N)$ and $(I_{i+1}^c; F1 = N_i, F2 = N_{i+1}, F3 = H_{i+1}^N)$) in the $F2-F3$ plane of the HNN spectrum turn out to be

$$I^d = -(E_1^2 E_3 E_9 K_{i1}^d + E_2^2 E_5 E_{10} K_{i2}^d) \quad (6.104)$$

$$I_{i-1}^c = E_1 E_4 E_7 E_9 K_{i-1}^c$$

$$I_{i+1}^c = E_2 E_6 E_8 E_{10} K_{i+1}^c \quad (6.105)$$

where

$$E_1 = \cos p_i T_N \sin q_{i-1} T_N$$

$$E_2 = \sin p_i T_N \cos q_{i-1} T_N$$

$$E_3 = \cos p_{i-1} \tau_{CN} \cos q_{i-1} \tau_{CN}$$

$$E_4 = \sin p_{i-1} \tau_{CN} \sin q_{i-1} \tau_{CN}$$

$$E_5 = \cos p_i \tau_{CN} \cos q_i \tau_{CN}$$

$$E_6 = \sin p_i \tau_{CN} \sin q_i \tau_{CN}$$

$$E_7 = \sin p_{i-1} T_N \cos q_{i-2} T_N$$

$$E_8 = \cos p_{i+1} T_N \sin q_i T_N$$

$$E_9 = \cos n_{i-1} \tau_{CN}$$

$$E_{10} = \cos n_i \tau_{CN} \quad (6.106)$$

and

$$p_i = 2\pi^1 J(C_i^\alpha - N_i); q_i = 2\pi^2 J(C_i^\alpha - N_{i+1}); n_i = 2\pi^1 J(C_i^\alpha - C_i^\beta) \quad (6.107)$$

$$K_{i1}^d = \exp(-4T_N R_{2i}^N - 2\tau_{CN} R_{2,i-1}^\alpha)$$

$$K_{i2}^d = \exp(-4T_N R_{2i}^N - 2\tau_{CN} R_{2i}^\alpha)$$

$$K_{i-1}^c = \exp(-2T_N (R_{2i}^N + R_{2,i-1}^N) - 2\tau_{CN} R_{2,i-1}^\alpha)$$

$$K_{i+1}^c = \exp(-2T_N(R_{2i}^N + R_{2,i+1}^N) - 2\tau_{cN}R_{2i}^{\alpha}) \quad (6.108)$$

1J and 2J represent one-bond and two-bond N-C $^{\alpha}$ coupling constants and R_2^N and R_2^{α} 's are the various ${}^{15}\text{N}$ and C $^{\alpha}$ transverse relaxation rates, respectively.

This data after three-dimensional Fourier transformation yields the three-dimensional NMR spectrum.

$$S(t_1, t_2, t_3) \xrightarrow{3D-FT} S[F1({}^{15}\text{N}), F2({}^{15}\text{N}), F3(H^N)] \quad (6.109)$$

Equation 6.104 (I^d) gives rise to the diagonal peak ($F1 = F2 = N_i$, $F3 = H_i^N$) in the three-dimensional spectrum. The first term in Eq. 6.105 yields the cross-peak (I_{i-1}^c ; $F1 = N_i$, $F2 = N_{i-1}$, $F3 = H_{i-1}^N$). The second term in Eq. 6.105 yields another cross-peak (I_{i+1}^c ; $F1 = N_i$, $F2 = N_{i+1}$, $F3 = H_{i+1}^N$). A schematic representation of the three-dimensional spectrum is shown in Fig. 6.56a, and in Fig. 6.56b, c are shown, respectively, the $F1 - F3$ plane at $F2 = N_i$ and $F2 - F3$ plane at $F1 = N_i$.

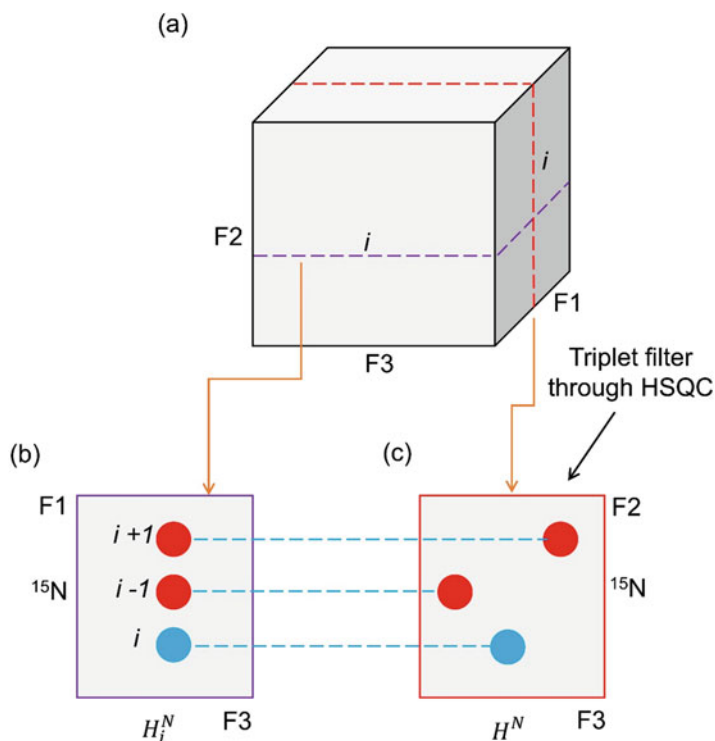


Fig. 6.56 (a) Schematic representation of the three-dimensional spectrum of HNN. (b) Schematic representation of $F1 - F3$ plane at a particular $F2 = N_i$. (c) Schematic representation of $F2 - F3$ plane at $F1 = N_i$. Cyan peaks are self-peaks ($F2 = F1 = N_i$), and the red peaks are sequential peaks

Clearly, the $F2 - F3$ plane at a particular $F1 = N_i$ is a triplet filter through the HSQC spectrum displaying exclusively the peaks of three consecutive residues ($i-1$, i , $i+1$) along the polypeptide chain. The orthogonal $F1 - F3$ plane at a particular $F2 = N_i$ shows correlations from the amide proton of residue “ i ” to the ^{15}N of residues $i-1$, i , and $i+1$. This feature eliminates the need to scan through the ^{15}N planes as in the HNCA experiment to establish sequential correlations.

Figure 6.57 shows the coherence transfer efficiencies and consequent intensities of the diagonal and cross-peaks with and without including relaxation. These curves indicate the optimum value to be chosen for the $2\tau_{CN}$ period. As mentioned earlier, a value of 22–30 ms turns out to be the optimum choice, which gives reasonable intensities for both the diagonal and the cross-peaks.

The HNN experiment has an additional interesting feature in the patterns of peaks. The diagonal and cross-peaks will have different combinations of positive and negative signs depending upon the nature of the residues in the triplet sequence represented by the chosen plane. This feature arises because of the fact that during the $2\tau_{CN}$ period, the magnetization on C^α evolves under the influence of $C^\alpha - C^\beta$ coupling; the coefficients E9 and E10 which reflect this coupling evolution contribute to the change in sign patterns of the diagonal and cross-peaks. Since the glycine

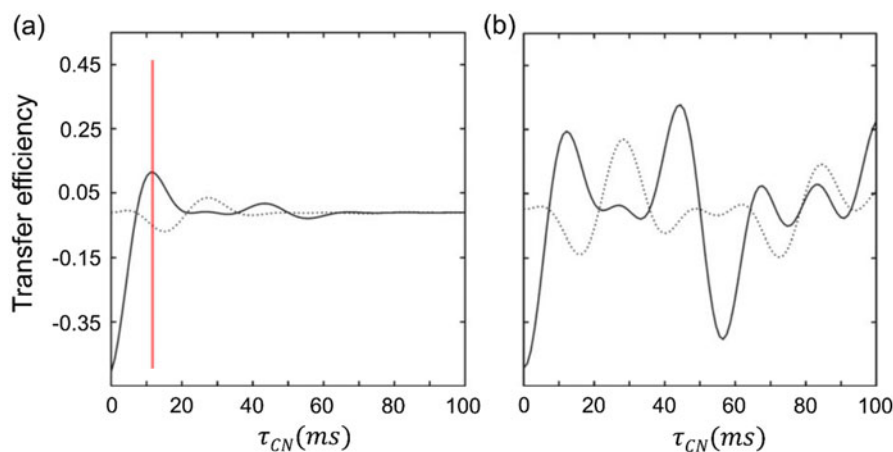


Fig. 6.57 Plots of the HNN coherence transfer efficiencies. The transfer functions for the diagonal peak I^d and the cross-peaks I_{i-1}^c, I_{i+1}^c . Here, (a) is for the transfer efficiencies calculated with relaxation terms, while (b) is for calculations without the relaxation terms. The transfer efficiency is plotted as a function of τ_{CN} . The plots were calculated by using, $J_{C^\alpha C^\beta}$, $J_{C^\alpha CO}$, and J_{NCO} values of 35, 55, and 15 Hz, respectively. The $^1J_{C^\alpha N}$, and $^2J_{C^\alpha N}$ values have been chosen to be 10.5 and 8.5 Hz, respectively. The value of T_N used in the transfer functions for HNN was 14.0 ms. Thick and dotted lines represent diagonal and sequential peaks, respectively. The vertical red line indicates the optimum choice for the τ_{CN} value. For this choice, the diagonal and cross-peaks have opposite signs. (Reproduced from Journal of Magnetic Resonance. 181, 21 (2006), with the permission of Elsevier Publishing)

residues do not have a C^β carbon, they appear distinctly and generate different peak patterns depending upon the position of the glycine in the triplet sequence. Four different cases of triplet amino acid sequences can be considered: (i) XGZ, (ii) GYZ, (iii) G'GZ, and (iv) ZXY, where X, Y, and Z can be any amino acid residue other than glycine and proline and G is glycine. The cases (i)–(iii) are special cases containing glycine in the triplet sequence, and case (iv) is a general case. For the three special cases (i) to (iii), the relevant density operators before the start of detection are given by the following:

- (i) -XGZ-: In this case the $C^\alpha - C^\beta$ couplings are absent and hence $E_{10} = 1$. Thus, the transfer efficiencies are as follows:

$$I^d = -(E_1^2 E_3 E_9 K_{i1}^d + E_2^2 E_5 K_{i2}^d) \quad (6.110)$$

$$I_{i-1}^c = E_1 E_4 E_7 E_9 K_{i-1}^c$$

$$I_{i+1}^c = E_2 E_6 E_8 K_{i+1}^c \quad (6.111)$$

- (ii) -GYZ-: In this case $C^\alpha - C^\beta$ coupling of the $(i-1)$ th residue vanishes and hence $E_9=1$. The transfer efficiencies can be written as follows:

$$I^d = -(E_1^2 E_3 K_{i1}^d + E_2^2 E_5 E_{10} K_{i2}^d) \quad (6.112)$$

$$I_{i-1}^c = E_1 E_4 E_7 K_{i-1}^c$$

$$I_{i+1}^c = E_2 E_6 E_8 E_{10} K_{i+1}^c \quad (6.113)$$

- (iii) -G'GZ-: Here both E_{10} and E_9 terms become unity, and the equations can be written as:

$$I^d = -(E_1^2 E_3 K_{i1}^d + E_2^2 E_5 K_{i2}^d) \quad (6.114)$$

$$I_{i-1}^c = E_1 E_4 E_7 K_{i-1}^c$$

$$I_{i+1}^c = E_2 E_6 E_8 K_{i+1}^c \quad (6.115)$$

The calculated peak patterns in $F1-F3$ planes for various combinations of triplets of sequences involving a glycine residue at different positions in the triplet are shown in Fig. 6.58. If there is a proline residue at either $(i-1)$ or $(i+1)$ position in the triplet, the corresponding peak will not appear in the spectrum.

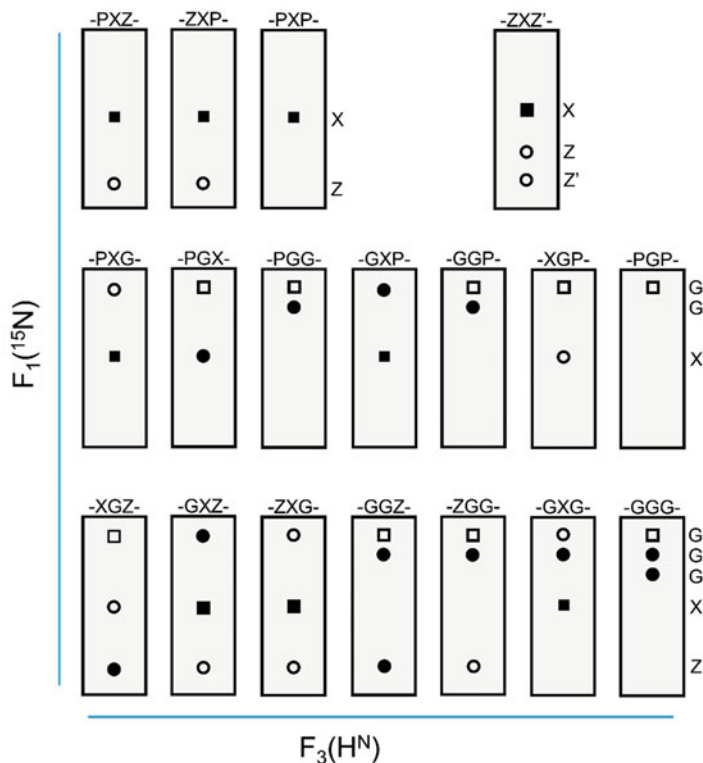


Fig. 6.58 Schematic patterns in the F_1 - F_3 planes at the F_2 chemical shift of the central residue in the triplets mentioned on the top of each panel, in the HNCA spectra for various special triplet sequences. X, Z, and Z' are any residue other than glycine (G) and proline (P). Squares are the diagonal peaks and circles are the sequential peaks. Filled and open symbols represent positive and negative signals, respectively. In all cases, the peaks are aligned at the F_3 (H^{N}) chemical shift of the central residue

6.7.3 The Constant Time HN(CO)CA Experiment

The HNCA experiment described earlier establishes the correlation between residue “ i ” and $(i-1)$ along the polypeptide chain. A particular cross-section plane along the ^{15}N axis shows peaks between amide protons of residue “ i ” and C^α carbons of residues i and $i-1$. However, a priori, it is not possible to identify the i and $i-1$ peak individually, unambiguously. The HN(CO)CA experiment has been designed to circumvent this problem by adopting a different magnetization transfer pathway, which allows the flow of magnetization through the pulse sequence in one direction along the polypeptide chain. This is as indicated in Eq. 6.116.

$$\begin{aligned}
 H_i^N &\rightarrow N_i(t_1) \rightarrow \text{CO}(i-1) \rightarrow C^\alpha(i-1)(t_2) \rightarrow \text{CO}(i-1) \rightarrow N_i \\
 &\rightarrow H_i^N(t_3)
 \end{aligned}
 \tag{6.116}$$

Figure 6.59 shows the pulse sequence of the CT-HN(CO)CA experiment.

The experiment can be analyzed by the product operator formalism as for other experiments. The experiment starts with an initial INEPT transfer from H_i^N to N_i of residue i . At time point a , in the pulse sequence, the relevant density operator is

$$\rho_a = -2H_{iz}^N N_{iy}
 \tag{6.117}$$

This antiphase magnetization of N_i is refocused to in-phase magnetization, which then evolves under coupling to $\text{CO}(i-1)$ exclusively for the period $\delta_1 + \delta_2 + \delta_3 = 2\delta_1$. This is normally adjusted between $\frac{1}{2J_{\text{NCO}}}$ and $\frac{1}{3J_{\text{NCO}}}$ and most often it is set to $\frac{1}{3J_{\text{NCO}}}$. Note, C^α is decoupled by the application 180° pulses on C^α channel and the ^{15}N channel. N_i -magnetization also evolves under N_i -chemical shifts leading to frequency labeling in the time period t_1 . The relevant density operator at point b in the pulse sequence is given by

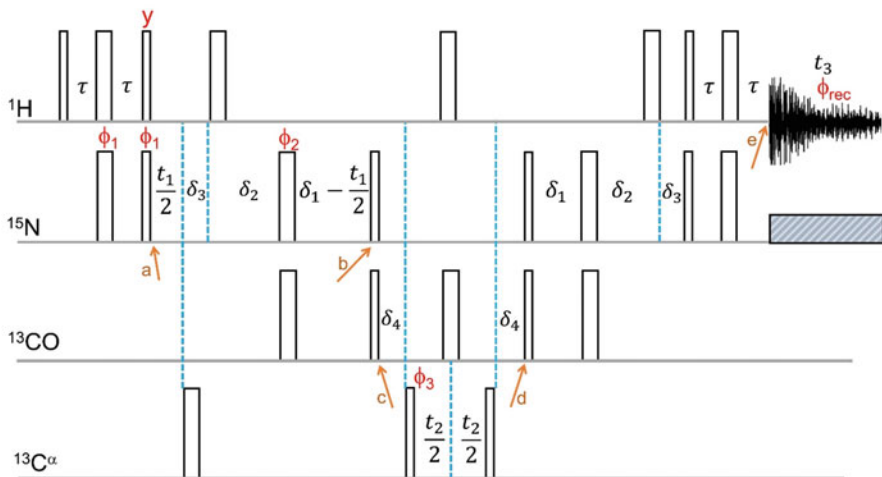


Fig. 6.59 Pulse sequence for the CT-HN(CO)CA experiment. Wide and narrow rectangles indicate 180° and 90° pulses, respectively. Typically, the delays are $2\delta_1 \approx 22 \text{ ms} \left[\approx \frac{1}{3J_{\text{NCO}}} \right]$, $2\delta_3 \approx \frac{1}{2J_{\text{NH}}}$, $\delta_2 = (\delta_1 - \delta_3)$, and δ_4 in the range $\frac{1}{3J_{\text{C}^\alpha\text{CO}}}$ to $\frac{1}{2J_{\text{C}^\alpha\text{CO}}}$. Unless mentioned, the pulse phases are along the x -axis. The phase cycles mentioned are $\phi_1 = x, -x$; $\phi_2 = 4(x), 4(y), 4(-x), 4(-y)$; $\phi_3 = 2(x), 2(-x)$, and $\phi_{\text{rec}} = x, -x, -x, x, -x, x, x, -x$. Quadrature detection in the t_1 and t_2 dimensions is achieved by incrementing independently the phases ϕ_1 and ϕ_3 , respectively, along with the receiver phase, as in a states-TPPI manner

$$\rho_b = 2 N_{iy} \text{CO}_{(i-1)z} \cos(\omega_{N_i} t_1) \sin(2\pi J_{\text{NCO}} \delta_1) \sin(2\pi J_{\text{NH}} \delta_3) \quad (6.118)$$

The simultaneous application of 90° pulses on CO and ^{15}N channels at this point causes transfer into antiphase CO magnetization, and the relevant density operator at time point c is given by

$$\rho_c = -2 N_{iz} \text{CO}_{(i-1)y} \cos(\omega_{N_i} t_1) \sin(2\pi J_{\text{NCO}} \delta_1) \sin(2\pi J_{\text{NH}} \delta_3) \quad (6.119)$$

This magnetization then evolves under C^α coupling for the period δ_4 , and it is transferred to $C^\alpha(i-1)$, which is then frequency labeled during the period t_2 . At the end it is back transferred to $\text{CO}(i-1)$, which continues to evolve under the $C^\alpha - \text{CO}$ coupling, for the next δ_4 period, and at time point d , the relevant density operator is

$$\rho_d = -2 N_{iz} \text{CO}_{(i-1)y} \cos(\omega_{N_i} t_1) \cos(\omega_{C_{i-1}^\alpha} t_2) \cos(\pi J_{C^\alpha C^\beta} t_2) \sin^2(\pi J_{C^\alpha \text{CO}} \delta_4) \sin(2\pi J_{\text{NCO}} \delta_1) \sin(2\pi J_{\text{NH}} \delta_3) \quad (6.120)$$

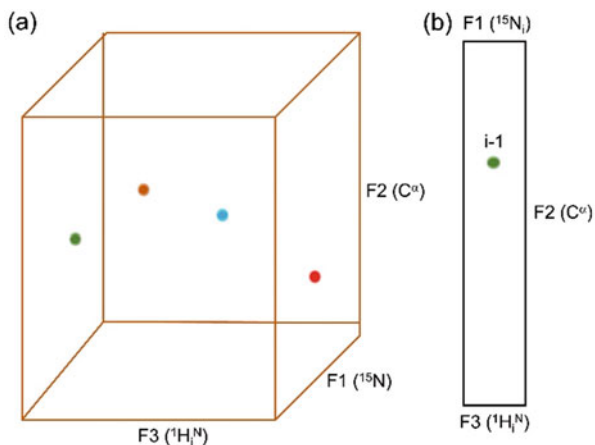
Magnetization is now on $\text{CO}_{(i-1)}$. During the subsequent part of the pulse sequence, the magnetization retraces the path evolving under the various couplings, and at time point e , the relevant density operator leading to observable magnetization is given by

$$\rho_e = H_{ix}^N \cos(\omega_{N_i} t_1) \cos(\omega_{C_{i-1}^\alpha} t_2) \cos(\pi J_{C^\alpha C^\beta} t_2) \sin^2(\pi J_{C^\alpha \text{CO}} \delta_4) \sin^2(2\pi J_{\text{NCO}} \delta_1) \sin^2(2\pi J_{\text{NH}} \delta_3) \quad (6.121)$$

The amide proton magnetization is then detected during “ t_3 ” under ^{15}N decoupling.

After three-dimensional Fourier transformation, this leads to a spectrum schematically shown in Fig. 6.60.

Fig. 6.60 (a) Schematic spectrum of three-dimensional CT-HN(CO)CA. (b) The F2-F3 cross-section at a particular ^{15}N chemical shift along F1. Here only the sequential connections i to $(i-1)$ are seen. Different colors are used to distinguish between the residues



6.7.4 The HN(C)N Experiment

This is a counter part of HNN in the same manner as HN(CO)CA is a counter part of the HNCA experiment, providing the directionality to the sequential assignment process of the backbone atoms along the polypeptide chain. The pulse sequence for this experiment is shown in Fig. 6.61, and the magnetization transfer pathway is shown in Fig. 6.62.

Note that the flow of the magnetization is similar to that in HN(CO)CA till the point reaches $C^\alpha(i-1)$. The C^α 's are not frequency labeled, and the magnetization is transferred directly to the ^{15}N of residues i and $(i-1)$. This involves an additional

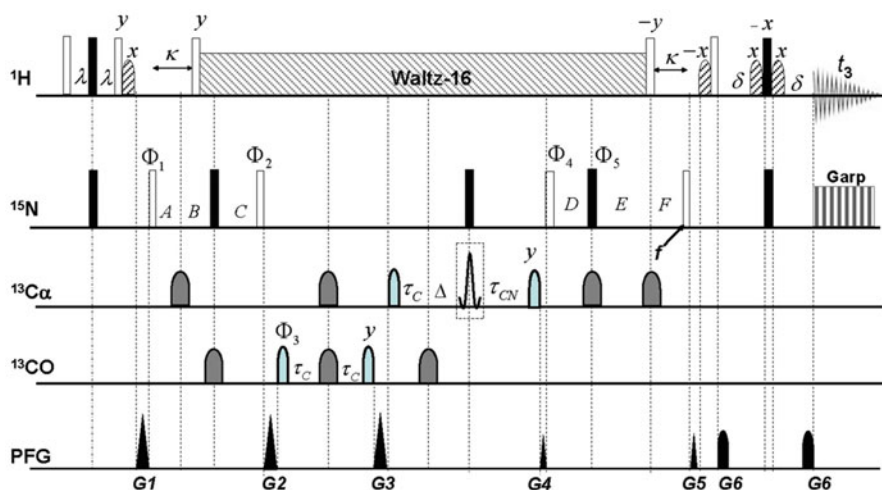


Fig. 6.61 Pulse sequence for the HN(C)N experiment. Narrow (hollow) and wide (filled black) rectangular bars represent nonselective 90° and 180° pulse, respectively. Narrow lobe (light blue) and wide lobe (gray) on carbon channel indicate selective 90° and 180° pulse, respectively. Unless indicated otherwise, the pulses are applied with phase x . Proton decoupling using the Waltz-16 decoupling sequence with field strength of 6.25 kHz is applied during most of the t_1 and t_2 evolution periods, and ^{15}N decoupling using the Garp-1 sequence with field strength 0.9 kHz is applied during acquisition. The ^{13}C carrier frequency for pulses, respectively, on $^{13}\text{C}^\alpha$ and ^{13}CO channels are set at 54.0 ppm and 172.5 ppm. The strength of the $^{13}\text{C}^\alpha$ pulses (standard Gaussian cascade Q3 (180°) and Q5 (90°) pulses) is adjusted so that they cause minimal excitation of carbonyl carbons. The 180° ^{13}CO -shaped pulse (width 200 μs) had a standard Gaussian cascade Q3 pulse profile with minimal excitation of $^{13}\text{C}^\alpha$. The delays are set to $\lambda = 2.7$ ms, $\kappa = 5.4$ ms, $\delta = 2.7$ ms. The delay τ_{CN} used for the evolution of one-bond and two-bond $^{13}\text{C}^\alpha - ^{15}\text{N}$ coupling is around 12–16 ms and must be optimized. The delay τ_{C} in the pulse sequence used for $^{13}\text{C}^\alpha - ^{13}\text{C}$ (refers to carbonyl, CO, carbon) coupling evolution is 4.5 ms. The values for the individual periods containing t_1 are $A = t_1/2$, $B = T_N$, and $C = T_N - t_1/2$. The values for the individual period containing t_2 are $D = T_N - t_1/2$, $E = T_N$, and $F = t_1/2$. The delay $2T_N$ is set to 24–28 ms, and $\Delta = \tau_{\text{CN}} - \tau_{\text{C}}$. Phase cycling for the experiment is $\Phi_1 = 2(x)$, $2(-x)$; $\Phi_2 = \Phi_3 = x$, $-x$; and $\Phi_4 = x$; $\Phi_5 = 4(x)$, $4(-x)$ and receiver = $2(x)$, $4(-x)$, $2(x)$. The frequency discrimination in t_1 and t_2 has been achieved using states-TPPI phase cycling of Φ_1 and Φ_4 , respectively, along with the receiver phase. The gradient (sine bell shaped; 1 ms) levels are optimized between 30% and 80% of the maximum strength of 53 G/cm in the z -direction. These destroy the unwanted transverse magnetization components

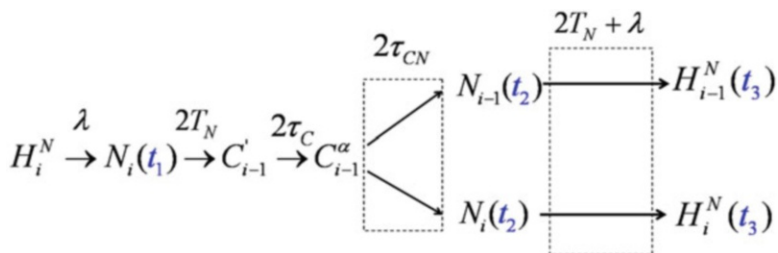


Fig. 6.62 Schematic of magnetization transfer pathway through the HN(C)N pulse sequence. Here C' refers to carbonyl (CO) carbon

transfer period, $2\tau_{CN}$. The ^{15}N are frequency labeled in the evolution time t_2 , and finally the magnetization is transferred to amide protons of residues i and $(i-1)$, which are then detected during the detection period t_3 .

The experiment can be analyzed using the product operator as has been done in the previous cases. The final relevant density operator at the start of the detection (t_3) is given by

$$\sigma_f = \left\{ 2H_{iz}N_{iy} \cos(\omega_{N_i}t_2)\Gamma_2\Gamma_4 - 2H_{(i-1)z}N_{(i-1)y} \cos(\omega_{N_{(i-1)}}t_2)\Gamma_3\Gamma_5 \right\} \sin(2\pi J_{C^\alpha CO}\tau_C)\Gamma_6\Gamma_1 \cos(\omega_{N_i}t_1) \quad (6.122)$$

where

$$\begin{aligned} \Gamma_1 &= \sin(2\pi J_{C^\alpha CO}\tau_C) \sin(2\pi J_{NCO}T_N) \\ \Gamma_2 &= \sin(2\pi^2 J_{C^\alpha N}\tau_{CN}) \cos(2\pi^1 J_{C^\alpha N}\tau_{CN}) \\ \Gamma_3 &= \sin(2\pi^1 J_{C^\alpha N}\tau_{CN}) \sin(2\pi^2 J_{C^\alpha N}\tau_{CN}) \\ \Gamma_4 &= \cos(2\pi^1 J_{C^\alpha N}T_N) \sin(2\pi^2 J_{C^\alpha N}T_N) \\ \Gamma_5 &= \sin(2\pi^1 J_{C^\alpha N}T_N) \cos(2\pi^2 J_{C^\alpha N}T_N) \\ \Gamma_6 &= \cos(2\pi J_{C^\alpha C^\beta}\tau_{CN}) \end{aligned} \quad (6.123)$$

τ_C , τ_{CN} , and $2T_N = A + B + C = D + E + F$ are the delays as indicated in the pulse sequence. The resultant data after the three-dimensional Fourier transformation yields the three-dimensional HN(C)N spectrum.

$$S(t_1, t_2, t_3) \xrightarrow{3D-FT} S[F1(^{15}\text{N}), F2(^{15}\text{N}), F3(H^N)] \quad (6.124)$$

The first term in Eq. (6.122) gives rise to the diagonal peak ($F1 = F2 = ^{15}\text{N}_i$, $F3 = H^{\text{N}_i}$) in the three-dimensional spectrum. The second term yields the cross-peak ($F1 = ^{15}\text{N}_i$, $F2 = ^{15}\text{N}_{(i-1)}$, and $F3 = H^{\text{N}_{i-1}}$). A schematic representation of the

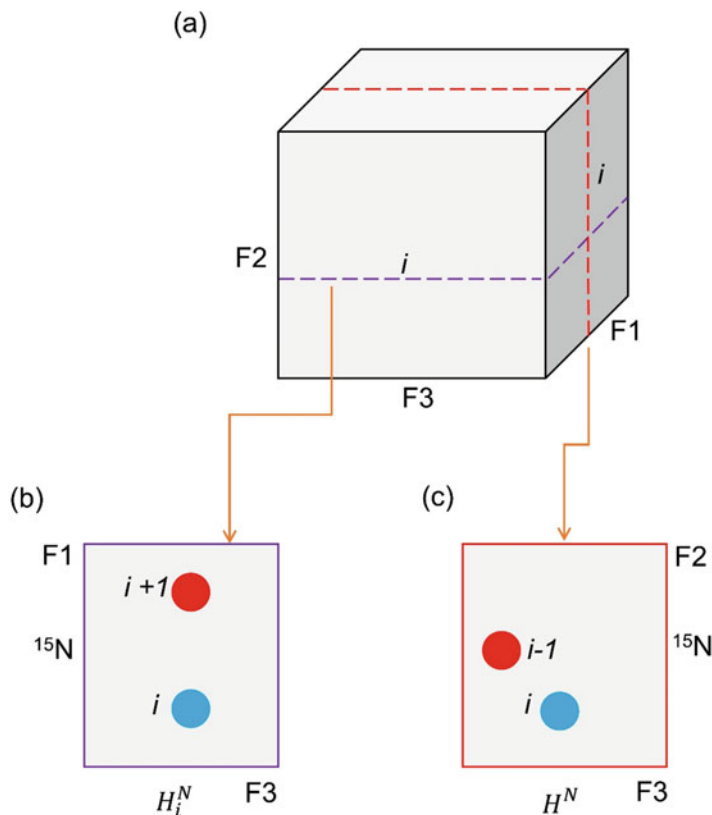


Fig. 6.63 (a) Schematic representation of the three-dimensional spectrum of HN(C)N. (b) Schematic representation of $F1 - F3$ plane at a particular $F2 = N_i$. (c) Schematic representation of $F2 - F3$ plane at $F1 = N_i$

three-dimensional spectrum is shown in Fig. 6.63a, and in Figs. 6.63b and 6.63c, the $F1-F3$ plane at $F2 = {}^{15}\text{N}_i$ and the $F2-F3$ plane at $F1 = {}^{15}\text{N}_i$ are shown, respectively.

Clearly, both the $F1-F3$ and $F2-F3$ cross-section planes provide directionality in sequential connections from the residue “ i .” The peaks also carry sign patterns as in the case of HNN experiment. The transfer efficiencies will be dictated by various coefficients (Γ 's) in the respective terms. The different delays (τ_C , τ_{CN} , T_N) have to be optimized as before in the case of HNN. τ_C is generally set to ~ 4.5 ms, and τ_{CN} and T_N are typically set to $\sim 12-15$ ms.

Here again, the glycine residues make a special contribution because of the lack of C^β carbon and consequent absence of evolution under $C^\alpha - C^\beta$ coupling. This results in special patterns for glycine residues as well as for those which are adjacent to glycines. Considering the various possibilities of triplets of residues involving glycines, the expected peak patterns can be calculated as in the case of HNN. These are shown schematically in Fig. 6.64.

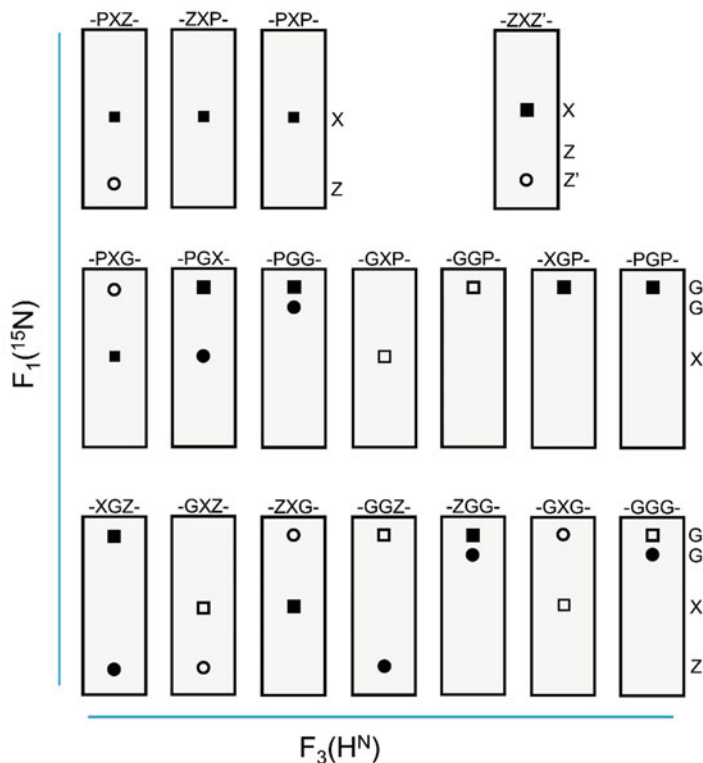


Fig. 6.64 Schematic patterns in the F_1 – F_3 planes at the F_2 chemical shift of the central residue in the triplets mentioned on the top of each panel, in the HN(C)N spectra for various special triplet sequences. X, Z, and Z' are any residue other than glycine (G) and proline (P). Squares are the diagonal peaks and circles are the sequential peaks. Filled and open symbols represent positive and negative signals, respectively. In all cases the peaks are aligned at the F_3 (H^N) chemical shift of the central residue

The special features in the peak patterns in the HN(C)N and HNN spectra generate the so-called checkpoints which help greatly for sequential resonance assignments in proteins. Sections of experimental HN(C)N and HNN spectra demonstrating the sequential walk through a stretch of polypeptide chain are shown in Fig. 6.65a, b, respectively.

In the HNN and HN(C)N experiments, glycine residues served to provide checkpoints for sequential resonance assignments. Simple modifications of these experiments have been described where alanines and serines/threonines also produce distinctive peak patterns, similar to glycines. These experiments have provided the foundation for many more developments, which have enabled rapid and unambiguous assignments in different kinds of protein systems, including folded, unfolded, intrinsically disordered, and partially folded proteins. A complete description of

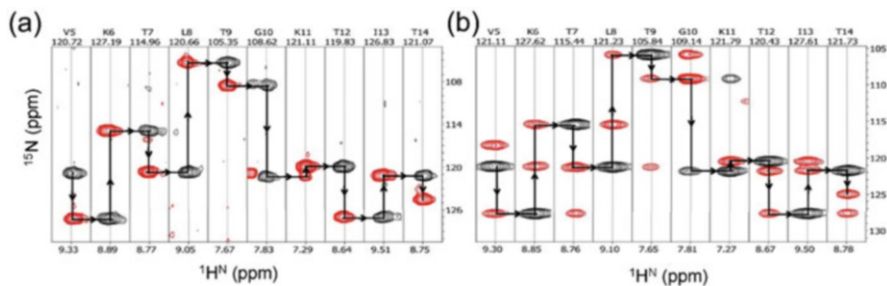


Fig. 6.65 (a) An illustrative stretch of sequential walk through the HN(C)N (a) and HNN (b) spectra of ubiquitin protein (1.6 mM, 76 aa). A sequential peak in one plane joins the diagonal peak in the adjacent plane on the right. Note that the panels of G10 and K11 constitute the checkpoints in this sequential walk. The numbers at the top and bottom in each panel A and B identify the F_2 (^{15}N) and F_3 ($^1\text{H}^{\text{N}}$) chemical shifts, which help in the identification of the diagonal peaks. Black and red contours represent the positive and negative peaks, respectively

these is beyond the scope of this book. The intention here has been only to give a flavor of the possibilities.

6.8 Summary

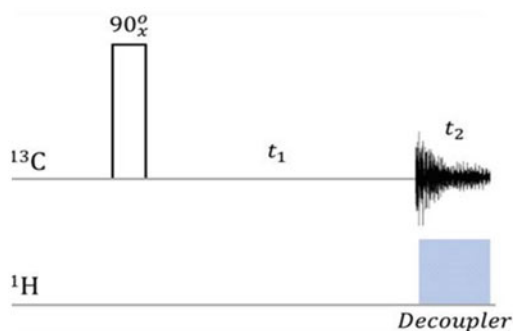
- The principles of multidimensional NMR are described.
- Different types of two-dimensional NMR are presented. The discussion is limited to some commonly used experiments.
- Illustrative elaborate product operator calculations are shown for some standard experiments. Some three-dimensional experiments are also described in some detail as illustrations.

6.9 Further Reading

- Principles of NMR in one and two dimensions, R. R. Ernst, G. Bodenhausen, A. Wokaun, Oxford, 1987
- High Resolution NMR Techniques in Organic Chemistry, T. D. W. Claridge, 3rd ed., Elsevier, 2016
- NMR Spectroscopy: Basic Principles, Concepts and Applications in Chemistry, H. Günther, 3rd ed., Wiley, 2013
- Understanding NMR Spectroscopy, J. Keeler, Wiley, 2005
- Protein NMR Spectroscopy, J. Cavanagh, N. Skelton, W. Fairbrother, M. Rance, A. Palmer III, 2nd ed., Elsevier, 2006

6.10 Exercises

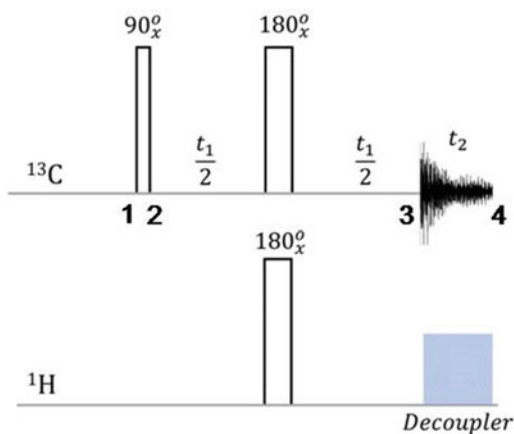
- 6.1 In a two-dimensional NMR experiment, which of the following statement is correct?
- Data is explicitly collected during two independent time variables t_1 and t_2 .
 - Data is explicitly collected only during t_2 .
 - Data is explicitly collected only during t_1 .
 - The spectrum is generated by frequency selective excitations along the two frequency axes (F_1 and F_2).
- 6.2 Fourier transformation of a complex NMR signal $S(t_1, t_2)$ leads to
- absorptive line shapes along both frequency axes
 - dispersive line shapes along both frequency axes
 - absorptive line shape along F_1 and dispersive line shape along F_2
 - mixed line shape along both frequency axes
- 6.3 If SW is the spectral width along the F_1 dimension of the two-dimensional spectrum and carrier is placed at the center of the spectrum, then in the TPPI method of quadrature detection, the dwell time along t_1 dimension is equal to
- 1 SW
 - 1/2 SW
 - 1/4 SW
 - 2 SW
- 6.4 Given the pulse sequence,



the F_2 axis of the two-dimensional spectrum for the molecule $\text{CH}_3\text{-CH}_2\text{-CH}_2\text{-Cl}$ will show

- 3 singlets
- 2 triplets and 1 quartet
- 1 quartet and 1 triplet
- 1 quartet and quintet

6.5 In a heteronuclear (C-H) spin echo experiment shown in the figure, the F_1 axis displays



- (a) carbon multiplets (J_{CH}) orthogonal to F_2 axis
 (b) no multiplets
 (c) multiplets tilted by 45° with respect to F_2 axis
 (d) fine structure along with chemical shift of individual carbon nuclei
- 6.6 In a homonuclear two-dimensional J-resolved spectrum,
- (a) F_1 axis has chemical shifts and F_2 axis has coupling constants
 (b) F_1 axis has coupling constants and F_2 axis has chemical shifts and coupling constants
 (c) F_1 axis has coupling constants and F_2 axis has chemical shifts
 (d) F_1 axis has chemical shifts and coupling constants and F_2 axis has chemical shifts
- 6.7 In a two-dimensional homonuclear J-resolved experiment, the peaks have
- (a) absorptive line shape along F_1 and dispersive line shape along F_2
 (b) absorptive line shape along both F_1 and F_2
 (c) dispersive line shape along both F_1 and F_2
 (d) mixed line shapes along both F_1 and F_2
- 6.8 In a two-dimensional homonuclear COSY experiment, which of the following is correct?
- (a) Cross-peak arises due to magnetization transfer mediated by dipolar interaction.
 (b) Cross-peak arises due to magnetization transfer mediated by J-coupling interaction.
 (c) Diagonal peak arises due to magnetization transfer mediated by dipolar interaction.
 (d) Diagonal peak arises due to magnetization transfer mediated by J-coupling interaction.

6.9 Diagonal peaks in a COSY spectrum

- (a) have no fine structure
- (b) have fine structure with dispersive line shape along both frequency axes
- (c) have fine structure with absorptive line shape along F_1 axis and dispersive line shape along F_2 axis
- (d) have fine structure with dispersive line shape along F_1 axis and absorptive line shape along F_2 axis

6.10 The diagonal peak for a two-spin system ($I = 1/2$) in a two-dimensional COSY spectrum will have the fine structure

- (a) $\begin{bmatrix} + & - \\ - & + \end{bmatrix}$
- (b) $\begin{bmatrix} + & + \\ + & + \end{bmatrix}$
- (c) $\begin{bmatrix} + & - \\ + & - \end{bmatrix}$
- (d) $\begin{bmatrix} + & + \\ - & - \end{bmatrix}$

6.11 The cross-peak for a two-spin system ($I = 1/2$) in a two-dimensional COSY spectrum will have the fine structure

- (a) $\begin{bmatrix} + & - \\ - & + \end{bmatrix}$
- (b) $\begin{bmatrix} + & + \\ + & + \end{bmatrix}$
- (c) $\begin{bmatrix} - & - \\ - & - \end{bmatrix}$
- (d) $\begin{bmatrix} + & + \\ - & - \end{bmatrix}$

6.12 In the cross-peak in a two-dimensional COSY spectrum, the line shapes along the F_1 and F_2 dimension will be (*abs*: absorptive line shape; *dis*: dispersive line shape)

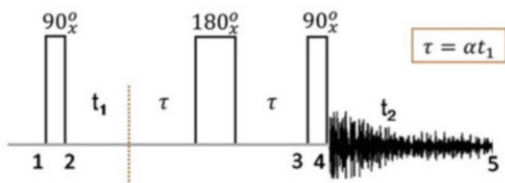
- (a) $\begin{bmatrix} abs & dis \\ dis & abs \end{bmatrix}$
- (b) $\begin{bmatrix} abs & abs \\ dis & dis \end{bmatrix}$
- (c) $\begin{bmatrix} dis & abs \\ dis & abs \end{bmatrix}$
- (d) $\begin{bmatrix} abs & abs \\ abs & abs \end{bmatrix}$

- 6.13 In a two-dimensional COSY spectrum, for a linear AMX spin system, with $J_{AM} > J_{MX}$, the M spin fine structure in the AM cross-peak is
- [+ - + -]
 - [+ + - -]
 - [+- - +]
 - [+ + + +]
- 6.14 In a two-dimensional COSY spectrum of a three-spin AMX system, the fine structure in a cross peak
- is determined by the relative magnitude of the chemical shifts
 - is determined by the relative magnitudes of the active and passive coupling constants
 - does not depend upon the signs of the coupling constants
 - is entirely determined by the passive couplings
- 6.15 In a DQF-COSY spectrum of a two-spin system ($I = 1/2$),
- both the diagonal and cross peak have the same fine structure and line shapes
 - the diagonal peak has antiphase structure and dispersive line shape, while the cross peak has antiphase structure and absorptive line shape
 - both the diagonal and cross peak have in-phase structure and absorptive line shape
 - the diagonal has in-phase structure and dispersive line shape and cross peak have antiphase structure and absorptive line shape
- 6.16 Phase cycling in the DQF-COSY experiment
- helps to improve the signal-to-noise ratio
 - helps in selection of coherence transfer pathway
 - helps to remove artefacts of pulse imperfections
 - helps to improve the resolution in the spectrum
- 6.17 In a two-dimensional NOESY experiment, the cross peak arises
- between J-coupled protons
 - between protons coupled by dipolar interaction
 - between chemically equivalent protons
 - between magnetically equivalent protons
- 6.18 The intensity of a cross-peak between two protons separated by distance “r,” in a two-dimensional NOESY spectrum, is proportional to
- r
 - 1/r
 - $1/r^3$
 - $1/r^6$
- 6.19 The CT-COSY experiment achieves
- homonuclear broadband decoupling along the F_1 dimension
 - homonuclear broadband decoupling along the F_2 dimension
 - selective decoupling along the F_1 dimension
 - selective decoupling along the F_2 dimension

6.20 In CT-COSY experiment,

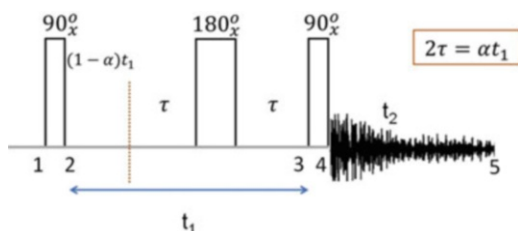
- J-coupling evolution does not occur during the t_1 period
- J-coupling evolution occurs for the same time Δ for all the t_1 increments
- chemical shift evolves through the constant time Δ
- J-coupling evolution occurs for the periods $\Delta - t_1$, and the chemical shift evolution occurs for the period t_1

6.21 In the following pulse sequence,



- chemical shifts appear scaled up in the indirect dimension
- J-values appear scaled up in the indirect dimension
- J-values appear scaled down in the indirect dimension
- both J-values and chemical shift are scaled up in the indirect dimension

6.22 In the given pulse sequence,



- chemical shifts are scaled up in the indirect dimension
- chemical shifts appear scaled down in the indirect dimension
- J-values appear scaled up in the indirect dimension
- J-values appear scaled down in the indirect dimension

6.23 In the TOCSY experiment, which of the following statements are true?

- There is in-phase transfer of coherence.
 - There is relay of magnetization.
 - Transfer efficiency is worse than that in INEPT transfer.
 - Spin lock leads to isotropic Hamiltonian.
- All the statements are true.
 - A, B, C are true.
 - A, B, D are true.
 - B, C, D are true.

6.24 In heteronuclear COSY experiment with the pulse sequence

$$90_x(^1\text{H}) - t_1 - 90_x(^1\text{H}, ^{13}\text{C}) - t_2 - (\text{acquisition}),$$

which of the following is true?

- (a) The C-H cross-peak has no fine structure.
- (b) The C-H cross-peak has fine structure along F_2 alone.
- (c) The C-H cross-peak has fine structure along F_1 alone.
- (d) The C-H cross-peak has fine structure along both F_1 and F_2 .

6.25 In a HSQC spectrum, which of the following statements are true?

- A. There is no fine structure in the cross peaks
 - B. Signal-to-noise is much superior compared to direct X detection experiment
 - C. Signal-to-noise ratio is inferior to direct X detection experiment
 - D. Cross-peaks have fine structure along the F_1 axis
- (a) A and B
 - (b) B and C
 - (c) C and D
 - (d) only A

6.26 In the HMQC spectrum, identify the correct statement.

- (a) The HX cross-peaks have no fine structure,
- (b) The HX cross-peaks have mixed phases resulting from H-H coupling evolutions,
- (c) The resolution is superior compared to HSQC spectrum,
- (d) The experiment takes less time than HSQC,

6.27 In a two-dimensional HSQC-TOCSY spectrum,

- (a) TOCSY causes relay along the F_2 axis.
- (b) TOCSY causes relay along the F_1 axis.
- (c) TOCSY leads to amplitude alteration HX cross peaks.
- (d) TOCSY leads to a phase alteration of HX cross peaks.

6.28 For a three-dimensional NMR experiment, recorded with 256, 512, and 1024 data points along the t_1 , t_2 , and t_3 axes, respectively, with acquisition time of 0.2 s and relaxation delay of 1 s, the total acquisition time with four scans for each FID will be approximately

- (a) 1.5 days
- (b) 3.5 days
- (c) 7.3 days
- (d) 11 days

6.29 In a three-dimensional experiment,

- (a) the evolution time t_1 and t_2 are incremented simultaneously
- (b) the evolution time t_1 and t_2 are incremented independently
- (c) t_1 is incremented synchronously with t_3
- (d) t_2 is incremented synchronously with t_3

Reference

Sanjay C. Panchal, Neel S. Bhavesh, and Ramakrishna V. Hosur (2001) Improved 3D triple resonance experiments, HNN and HN(C)N, for HN and ^{15}N sequential correlations in (^{13}C , ^{15}N) labeled proteins: Application to unfolded proteins. *J Biomol NMR* 20:135–147